

AB INITIO QUANTUM MECHANICAL STUDIES IN  
ELECTRONIC AND STRUCTURAL PROPERTIES OF  
CARBON NANOTUBES AND SILICON NANOWIRES

Thesis by

Yuki Matsuda

In Partial Fulfillment of the Requirements

for the Degree of

Doctor of Philosophy

California Institute of Technology

Pasadena, California

2008

(Defended 17 July, 2008)

To my parents

© 2008

Yuki Matsuda

All Rights Reserved

## **Acknowledgements**

First and foremost, I thank my advisor, Professor William A. Goddard III, for the great research opportunities he has provided me with, for his extensive suggestions and discussions, for teaching me, and for the encouragement and trust he has always maintained.

I specially thank Dr. Jamil Tahir-Kheli for his numerous suggestions, physics insights and discussions about my work. I am truly grateful to Professor Santiago D. Solares at University of Maryland, Professor Seung Soon Jang at Georgia Institute of Technology, and Professor Wei-Qiao Deng at Nanyang Technological University in Singapore, who provided me invaluable guidance in my projects while they were still members of the Materials and Process Simulation Center (MSC).

I thank all the members of the MSC, especially Shirley Wu for supporting my research, and Darryl Willick and Welison Floriano for their technical assistance with the MSC computational environment.

I thank all the Caltech staffs who have worked hard to support me in my studies, research work and campus life (special thanks to Jim Endrizzi at International Student Programs for ensuring that my stay in the U.S. was very comfortable).

Last but not least, I thank my parents, Toshihiro and Towako Matsuda, for all their hard work in raising me and my wonderful friends for being helpful and supportive throughout my time at Caltech.

## Abstract

This dissertation focuses on ab-initio quantum mechanical calculations of nanoelectronics in three research topics: contact resistance properties of carbon nanotubes and graphenes (Chapters 1 through 3), electrical properties of carbon nanotubes (Chapter 4) and silicon nanowires (Chapter 5). Through all the chapters, the aim of the research is to provide useful guidelines for experimentalists.

Chapter 1 presents the contact resistance of metal electrode–carbon nanotube and metal electrode–graphene interfaces for various deposited metals, based on first-principles quantum mechanical density functional and matrix Green’s function methods. Chapters 2 and 3 describe inventive ways to enhance contact resistance properties as well as mechanical stabilities using “molecular anchors” (Chapter 2) or using “end-contacted” (or end-on) electrodes (Chapter 3). Chapters 1 through 3 also provide useful guidelines for nanotube assembly process which is one of the main obstacles in nanoelectronics. Chapter 4 shows accurate and detailed band structure properties of single-walled carbon nanotubes using B3LYP hybrid functional, which are critical parameters in determining the electronic properties such as small band gaps ( $\sim 0.1$  eV) and effective masses. Chapter 5 details both structural and electronic properties of silicon nanowires. These results lead to the findings controlling the diameter and surface coverage by adsorbates (e.g., hydrogen) of silicon nanowires can be effectively used to optimize their properties for various applications.

All the theoretical results are compared with other theoretical studies and experimental data. Notably, electronic studies using B3LYP show excellent agreement with experimental studies quantitatively, which previous quantum mechanical calculations had failed.

These studies show how quantum mechanical predictions of complex phenomena can be effectively investigated computationally in nanomaterials and nanodevices. Given the difficulty, expense, and time required for experiments, theory may now be useful for high-throughput screening to identify the best conditions and materials before performing experiments.

## Table of Contents

Acknowledgements .....	iii
Abstract .....	iv
Table of Contents .....	vi
Chapter 1 Contact Resistance Properties between Nanotubes and Various Metals ...	1
Chapter 2 Improving Contact Resistance at the Nanotube-Cu Electrode Interface using Molecular Anchors .....	26
Chapter 3 Contact Resistance of “End-contacted” Metal–Graphene and Metal– Nanotube Interfaces .....	65
Chapter 4 Definitive Band Gaps for Single-Walled Carbon Nanotubes .....	98
Chapter 5 Surface and Electronic Properties of Hydrogen Terminated Si [001] Nanowires .....	127

## Chapter 1

# Contact Resistance Properties between Nanotubes and Various Metals\*

**Abstract.** We report on the interfacial structure, the current-voltage ( $I$ - $V$ ) characteristics, and contact resistance of metal electrode-carbon nanotube contacts for five metals, Ti, Pd, Pt, Cu and Au, based on first-principles quantum mechanical density functional and matrix Green's function methods. We find that Ti leads to the lowest contact resistance followed by Pd, Pt, Cu, and Au. The sequence,  $\text{Ti} \gg \text{Pd} > \text{Pt} > \text{Cu} > \text{Au}$ , correlates well with the predicted cohesive strength of the electrode-carbon interface. In addition Ti leads to linear  $I$ - $V$  characteristics up to  $\sim 1$  V, suggesting an Ohmic contact for both metallic and semiconductor nanotubes. However, the high reactivity of the Ti electrode at the contact to the nanotube distorts the nanotube structure.

---

\* Matsuda, Y.; Deng, W.-Q.; Goddard, W.A. III. "Contact Resistance Properties between Nanotubes and Various Metals from Quantum Mechanics". Published in *J. Phys. Chem. C*, *111*, 11113, **2007**.

## 1. Introduction

Carbon nanotubes are promising candidates for nanoelectronic devices due to their unique structural and electrical properties. Indeed, much experimental progress toward electronic devices based on carbon nanotubes has been reported.<sup>1–12</sup> In particular, near ballistic transport properties have been reported for both single-walled carbon nanotubes (SWNTs)<sup>1,2</sup> and multiwalled carbon nanotubes (MWNTs).<sup>10</sup> A potential problem with these devices is the high contact resistance, which significantly influences the conductance although it is hard to extract experimentally due to the variation in device geometries.

Several metals have been studied experimentally as candidates for ideal Ohmic contacts to carbon nanotubes,<sup>1–12</sup> but the experiments have given statistically inconsistent results due to difficulties in the fabrication of a large number of statistically representative carbon nanotube/metal contacts. Recent experimental results suggested that Pd and Ti contacts are superior to Au and Pt contacts,<sup>1–9</sup> but the results for Ti are erratic possibly due to the high chemical reactivity of Ti compared to other metals.<sup>9,12</sup> For example, annealing the Ti–carbon nanotube interface at temperatures above 973 K led to formation of titanium carbide at the interface.<sup>12</sup> Theoretical studies have been reported for the geometric structures of carbon nanotubes with “side-contacted” and “end-contacted” metal electrodes.<sup>13–18</sup> However, none of these studies reported the  $I$ – $V$  relationships (resistance) of metal–nanotube contacts although the Schottky barrier height between a metal surface (Pd, Pt, or Au) and a nanotube was reported.<sup>14</sup> We chose to simulate side-contacted nanotube models because current fabrication technology does not allow for the construction of end-contacted devices. We first considered the local structure,  $I$ – $V$

characteristics, and contact resistance from first-principles calculations on five metals (Ti, Pd, Pt, Cu, and Au) by depositing them on simple graphene surfaces to choose the best contact metals for nanotubes. We then used the best two candidate metals for investigating more realistic metal–nanotube models.

## 2. Computational Methodology

Our procedure was to start with a  $2 \times 2$  unit cell (8 carbons per layer) of the graphite surface (fixed at  $4.89 \times 4.89 \text{ \AA}^2$ ) and used quantum mechanics to optimize the periodic metal layers. We placed the atoms one by one, followed by relaxing the geometry each time to represent the deposited metal on the graphite surface. We used SEQUEST,<sup>19</sup> a fully self-consistent Gaussian-based linear combination of atomic orbitals (LCAO) density functional theory (DFT) method with double- $\zeta$  plus polarization (DZP) basis sets.<sup>20</sup> All calculations were based on the Perdew–Burke–Ernzerhof (PBE) generalized gradient approximation (GGA) with PBE pseudo-atomic potentials and spin polarization within two-dimensional periodic boundary conditions.<sup>21</sup> The  $k$ -point sampling of  $4 \times 4$  in the Brillouin Zone and the real space grid interval of  $32 \times 32$  in the  $x$ – $y$  plane, for a grid spacing of 0.25 / point, were carefully determined by energetic convergence.

## 3. Results and Discussion

In each case, we found approximately closed-packed layers of metal (three atoms per layer per cell) with ABC stacking (face-centered cubic (fcc)) for Pd, Pt, Cu and Au and

ABAB stacking (hexagonal close-packed (hcp)) for Ti, just as expected for the bulk structures. For Ti fcc packing was found to be less stable than hcp structure by 1.2 kcal / mol per unit cell. Figures 1a and 1b show the top views and side views of the models of Ti and Pd deposited on a  $4 \times 4$  graphene sheet. For each system the metal–metal distances within each layer is within 10% of the nearest neighbor distances of the bulk crystal structure. Importantly, the distance between graphene and the first deposited metal layer is quite small for Ti (strong bonding) and increases as  $\text{Pd} < \text{Pt} < \text{Cu} < \text{Au}$  (Table 1). The interaction energy of each metal–graphene model was calculated by changing the distance at the interface using the single-point energy calculation (Figure 1c). Figure 1c showed that the Ti layers bind strongly with graphene (48.3 kcal / mol per unit cell), while the cohesion for the other metals is much weaker, decreasing as  $\text{Pd} > \text{Pt} > \text{Cu} > \text{Au}$ , inversely correlated with the metal–graphene layer distance.

To compare directly the contact resistance at the interface between each metal and graphene sheet,  $I$ – $V$  models were constructed from the optimized geometries (Figures 1a and 1b) by reversing one of the models and placing it at the AB stacking positions of the original graphene sheet (Figures 2a and 2b). These models represent the two contacts (source and drain) of a nanotube. The distance between the two graphene sheets was fixed at 3.4 Å, which is specified by the experimental data.<sup>20</sup> Using these metal–graphene–metal configurations, we calculated the current as a function of voltage to compare the contact resistance of the five deposited metals. First we calculated the projected density of state (PDOS) from DFT quantum mechanics, and then we calculated the transmission coefficient using nonequilibrium Green’s function theory with DFT (which we have used successfully to compute transport properties of molecular electronic

devices).<sup>23, 24</sup> The transmission function was then used in the Landauer-Buttiker formula to calculate the  $I$ - $V$  characteristics. The total resistance of these systems was then obtained from the zero-bias transmission.

The PDOS of the  $p\pi$  orbitals of the graphene carbon atoms is shown in Figure 2c while the PDOS for the d-orbitals of the first-layer metal atoms (the layer closest to the graphene) is shown in Figure 2d. (The PDOS of other orbitals of carbon and the metals are not shown since their values did not contribute significantly.) For the Ti model, the d PDOS of Ti and the  $p\pi$  PDOS of carbon are large and uniform, indicating a good conduction channel. The Pd and Pt models showed the second and third highest combinations of metal d PDOS and graphene  $p\pi$  PDOS. For the Cu and Au models the  $p\pi$  PDOS shows many peaks or resonances, indicating electronic weak coupling of the metal with graphene. This behavior in the PDOS correlates directly with the metal carbon bond strength (Table 1): Ti  $\gg$  Pd > Pt > Cu > Au. The transmission function (Figure 2e) near the Fermi energy is mirroring the PDOS behaviors. In turn, the  $I$ - $V$  characteristics (Figure 2f) and total resistance per square nanometer (Figure 2g) correlate directly with the transmission coefficient and hence correlate with the cohesive coupling between metal d-orbitals and the graphite  $p\pi$  orbitals as discussed above. The bias voltage is defined as the difference between the source and the drain voltage.

We find that Ti has a linear  $I$ - $V$  curve indicating an Ohmic contact. We calculate contact resistances of 24.2 k $\Omega$  / nm<sup>2</sup> for Ti, 221 k $\Omega$  / nm<sup>2</sup> for Pd, 881 k $\Omega$  / nm<sup>2</sup> for Pt, 16.3 M $\Omega$  / nm<sup>2</sup> for Cu, and 32.6 M $\Omega$  / nm<sup>2</sup> for Au after averaging the bias voltage from -0.1 to +0.1 V. These values should be interpreted as a relative evaluation of these metals. Thus, on the basis of the graphene-metal model studies, we conclude that for metals deposited on

carbon nanotubes the contact resistance is the lowest for Ti, followed by Pd, Pt, Cu, and Au.

Next, we selected Ti and Pd, the best two candidates as contact materials, for calculations using more realistic metal–nanotube–metal assemblies. We placed the metallic SWNT (7,7), with diameter of 9.6 Å, between a pair of metal triple layers (Ti or Pd), keeping the periodic configurations of metal atoms on the graphene sheet and minimum distances at the electrode–nanotube interface obtained from the metal–graphene calculations. The geometries were minimized just as for the metal–graphite system using one-dimensional periodic boundary conditions (Figures 3a and 3b, where the top two layers were kept fixed). After optimization, we calculated the metal electrode–nanotube distance, cohesive energy, and strain energy in the SWNTs (compared to its original SWNT structure) (Table 2). For both systems, the distance between the nanotube and electrodes became 0.04–0.08 Å (1.9–2.8 %) smaller than that in the graphene case, indicating the larger attractive interaction due to the incursion of s hybrid character in the p $\pi$  orbital caused by the curvature of the nanotube. We found a similar ratio of the distance at the metal–nanotube interface as for metal–graphene (Ti/Pd = 0.75 in the graphene case and 0.75 for SWNT (7,7)), indicating that the graphite model represents the nanotube for geometric considerations.

The PDOS and the transmission functions of the Ti– or Pd–SWNT (7,7) are shown in Figures 3e and 3f, respectively. As expected from the metal–graphene studies, for Ti–SWNT (7,7), we find a strong coupling to the carbon p $\pi$  orbitals but much weaker for Pd–SWNT (7,7). The  $I$ – $V$  characteristics and contact resistance are shown in Figures 3g and 3h, respectively. The  $I$ – $V$  characteristics of Ti–SWNT (7,7) show linearity indicating

Ohmic contact. These calculations lead to contact resistances of  $6.9 \text{ k}\Omega / \text{nm}$  for Ti–SWNT (7,7) and  $63.7 \text{ k}\Omega / \text{nm}$  for Pd–SWNT (7,7) after averaging bias voltages from  $-0.1$  to  $0.1 \text{ V}$ . The contact resistance of Ti/Pd is 0.11 for graphene and 0.11 for metal nanotube.

Although the main point of this research was to determine the best metals for contacts to metallic nanotubes, we additionally considered the interface of the metal–semiconductor SWNT (13,0) with a diameter of  $10.0 \text{ \AA}$  (Figures 3c and 3d). This leads to similar geometries as for metallic nanotubes (the ratio of the distance at the interface is Ti/Pd = 0.77); however the Ti contacts significantly broaden the semiconductor nanotube states near the Fermi Energy, leading to a nearly metallic system as shown in Figure 3e. We expect that this would make Ti a poor candidate for the gate electrodes of carbon nanotube field-effect transistors. These calculations lead to contact resistances of  $30.7 \text{ k}\Omega / \text{nm}$  for Ti–SWNT (13,0) and  $1620 \text{ k}\Omega / \text{nm}$  for Pd–SWNT (13,0) after averaging bias voltages from  $-0.1$  to  $0.1 \text{ V}$ . The contact resistance of Ti/Pd is 0.02 for semiconductor nanotubes.

#### 4. Conclusion

In conclusion, our calculations suggest that the coupling of the metal d-orbitals of the electrode and the  $p\pi$  orbitals of the carbon atoms play a critical role in determining both the cohesive and the electronic interactions at the contacts. Considering only contact resistance, the suitability of metals as electrodes for metallic carbon nanotubes descends as  $\text{Ti} \gg \text{Pd} > \text{Pt} > \text{Cu} > \text{Au}$ . Ti forms an Ohmic contact through its strong chemical

bond to carbon atoms on both metallic and semiconductor nanotubes. However, the high reactivity of Ti might also lead to oxidation of the Ti<sup>11</sup> or else reaction with the nanotube to form titanium carbide (TiC).<sup>8</sup> We expect that our calculations provide a lower bound for contact resistances since we have assumed perfect contact geometries and no defects and have used DFT calculations with a PBE functional that underestimate the level of the conduction band.<sup>25</sup> The experimental trend that Ti and Pd are better than Pt and Au contacts<sup>1-9</sup> is in agreement with our calculations. The details of the comparisons are summarized in the Supporting Information (Table S1).

Contact metals have not been evaluated experimentally because it has been difficult to extract the contact resistance due to the variations in device geometries. Therefore, these results may provide useful guidelines for experimentalists to select the best contact materials for carbon nanotube device architectures. These studies show how first-principle predictions of complex phenomena such as contact resistance in metal–nanotube assemblies can now be effectively investigated computationally. Given the difficulty, expense, and time required for the experiments, theory may now be useful for high throughput screening to identify the best conditions and materials before performing experiments.

**Acknowledgements.**

This work was supported by Intel Components Research (Kevin O'Brien and Florian Gstrein) and by National Science Foundation (CCF-0524490 and CTS-0608889). The computer systems used in this research were provided by ARO-DURIP and ONR-DURIP. Additional support for the MSC was provided by ONR, ARO, DOE, NIH, Chevron, Boehringer-Ingelheim, Pfizer, Allozyne, Nissan, Dow-Corning, DuPont, and MARCO-FENA.

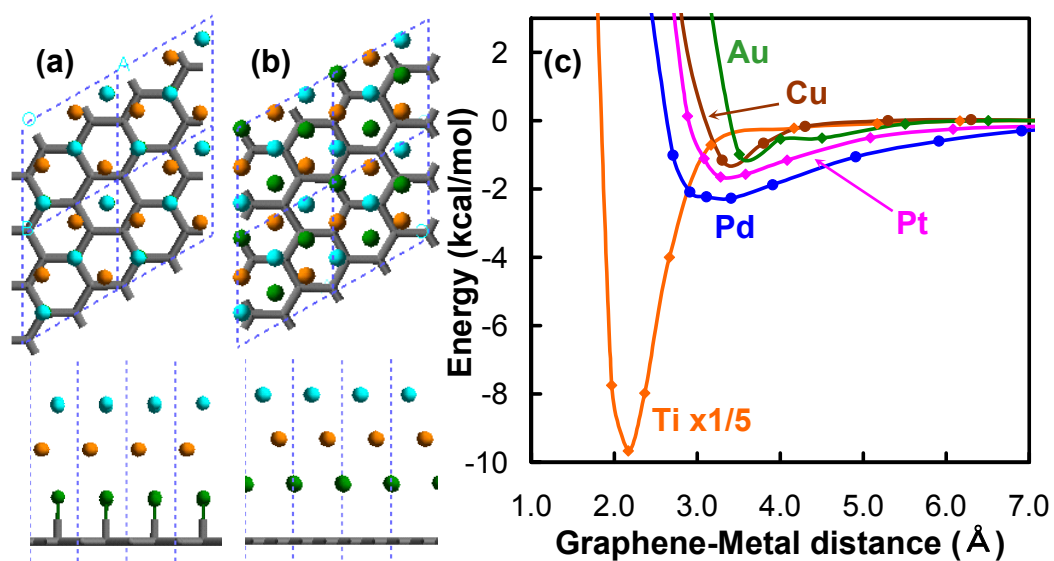


**Figure 1.** Optimized geometries of the top (top) and side (bottom) views of (a) Ti and (b) Pd deposited on a graphene  $4 \times 4$  sheet. (Unit cell for optimization is graphene  $2 \times 2$  sheet) (gray, graphite; green, metal first layer; orange, metal second layer; light blue, metal third layer). (c) Interaction energy of the metal–graphene model. Ti was scaled by 1:5 (orange, Ti; blue, Pd; pink, Pt; brown, Cu; green, Au).

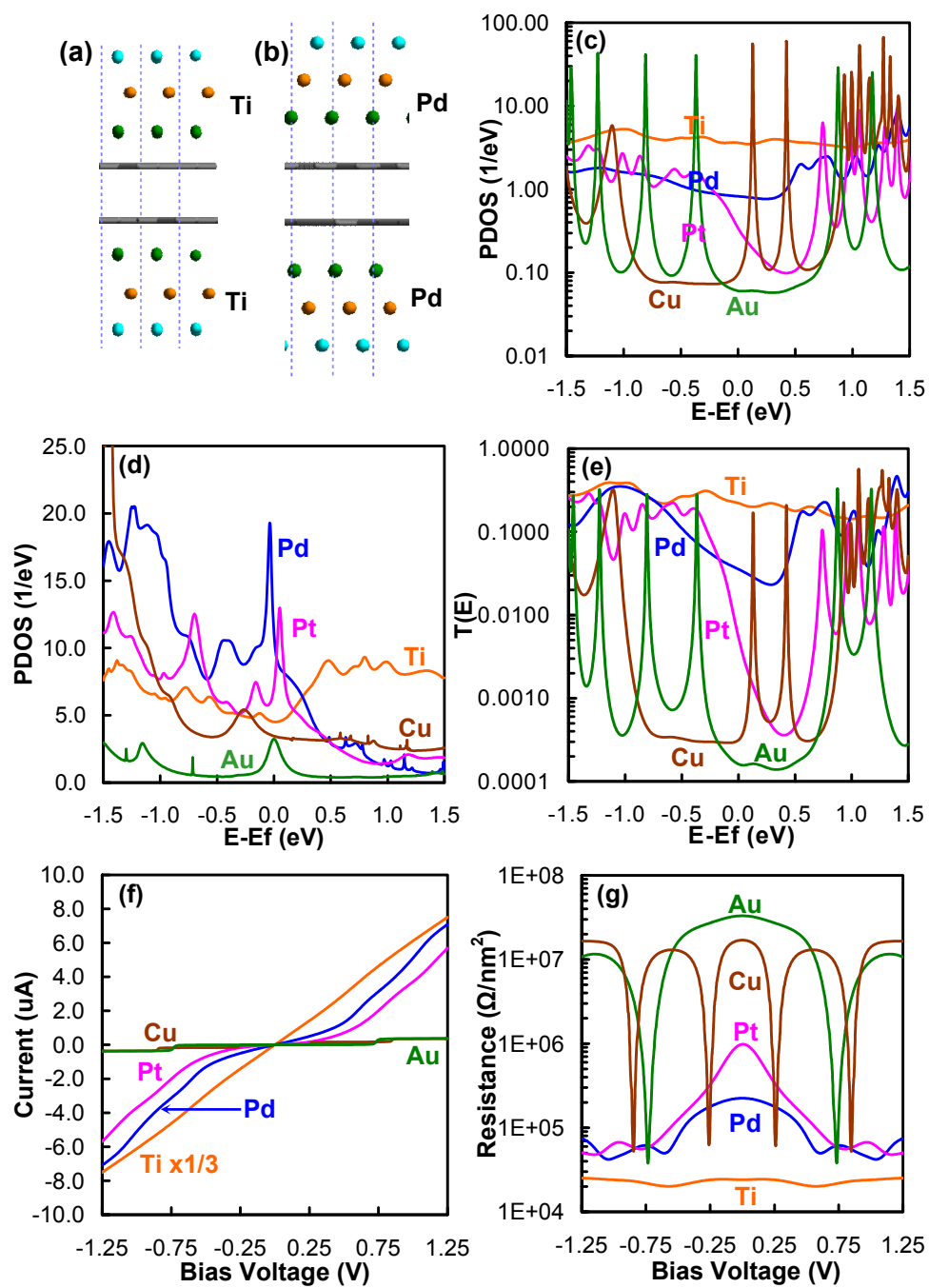


**Figure 2.**  $I$ - $V$  characteristics of the metal-graphene (two sheets of AB stacking) models.

Side views of  $I$ - $V$  calculation model of (a) Ti-graphene-Ti and (b) Pd-graphene-Pd.

The  $I$ - $V$  models were constructed from the optimized models of metal-graphene (Figures 1a and 1b). (c) Projected density of states (PDOS) near the Fermi energy ( $E_f$ ) of the  $p\pi$  orbital of carbon in graphite (orange, Ti; blue, Pd; pink, Pt; brown, Cu; green, Au). (d) PDOS of d-orbital of metal electrodes. (e) Transmission coefficient ( $T(E)$ ). (f)  $I$ - $V$  curve. Ti-graphite model was scaled by 1:3. (g) Contact resistance per square nanometer at metal-graphite interface.

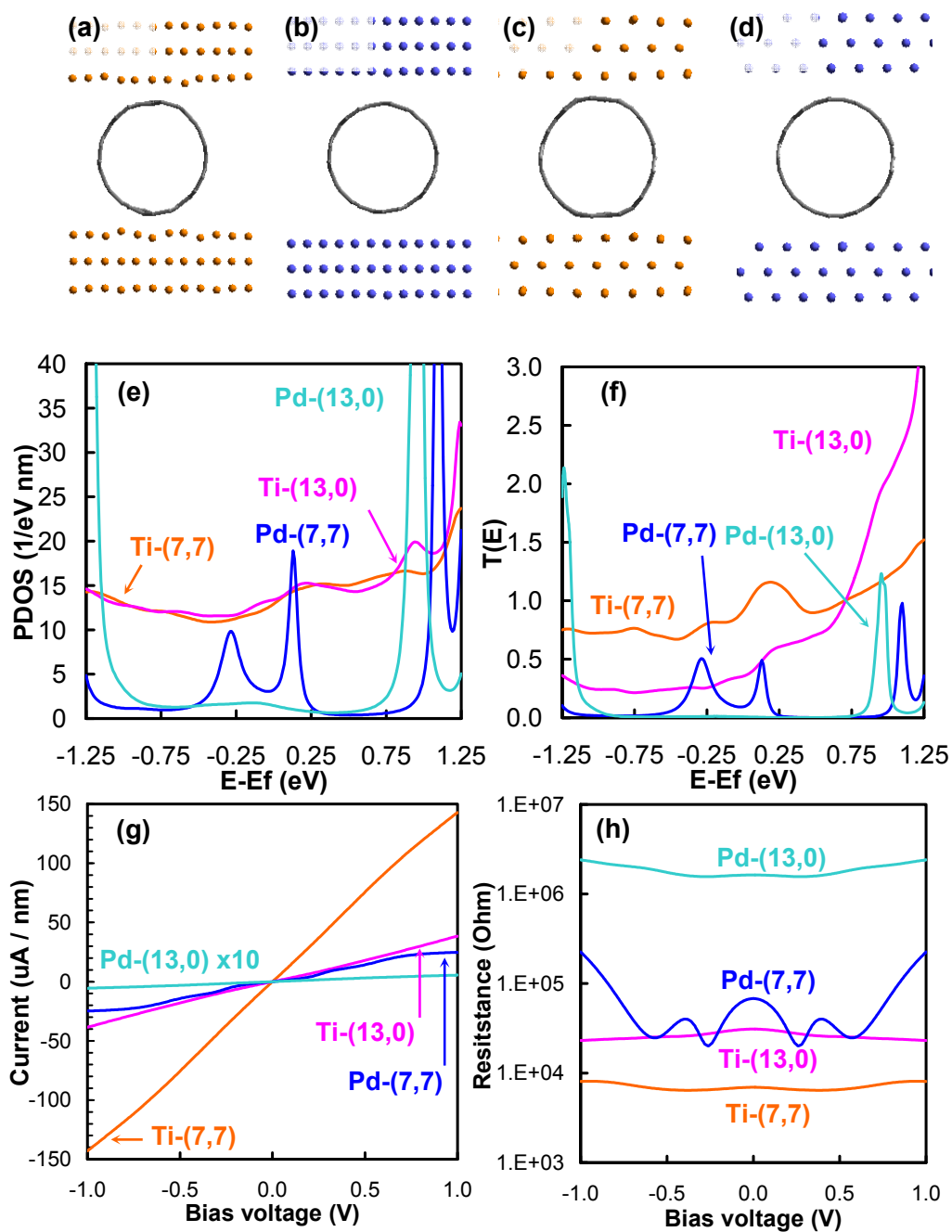


**Figure 3.**  $I$ - $V$  characteristics of Ti-SWNT (7,7), Pd-SWNT (7,7), Ti-SWNT (13,0), and Pd-SWNT (13,0).

Cross sections of the  $I$ - $V$  optimized models of (a) Ti-SWNT (7,7)-Ti, (b) Pd-SWNT (7,7)-Pd, (c) Ti-SWNT (13,0), and (d) Pd-SWNT (13,0). (e) PDOS (1/eV nm) near the Fermi energy. (f) Transmission coefficient ( $T(E)$ ). (g)  $I$ - $V$  curve. Pd-SWNT (13,0) was magnified by 10. (h) Contact resistance per nanometer. (orange, Ti -SWNT (7,7); blue, Pd-SWNT (7,7); pink, Ti-SWNT (13,0); light blue, Pd-SWNT (13,0)).

**Table 1.** Layer–Layer Distance of the Metal–Graphene Models after Optimization (Å) and Cohesive Energy (kcal/mol) of the Interface between Metal and Graphene<sup>a</sup>

	Ti	Pd	Pt	Cu	Au
graphene–first metal layer distance (Å)	2.17	2.91	3.38	3.30	3.50
first metal layer–second metal layer distance (Å)	2.44	2.22	2.30	2.02	2.54
second metal layer–third metal layer distance (Å)	2.27	2.22	2.29	2.02	2.52
bulk value (calculated) (Å)	2.33	2.27	2.29	2.14	2.40
bulk value (experimental) 300 K <sup>b</sup> (Å)	2.34	2.25	2.26	2.08	2.36
calculated metal–graphene cohesive energy (kcal/mol)	48.3	2.1	1.7	1.2	1.0

<sup>a</sup> All calculated distances are averaged values.

<sup>b</sup> Reference 22.

**Table 2.** Distance (Å) and Cohesive Energy (kcal/mol) between Metal and SWNT Models and Strain Energy of SWNT after Optimization.

	Ti-SWNT	Pd-SWNT	Ti-SWNT	Pd-SWNT
	(7, 7)	(7, 7)	(13, 0)	(13, 0)
SWNT–first metal layer distance (Å)	2.13	2.83	2.11	2.74
metal–SWNT cohesive energy (kcal/mol nm)	423.5	33.5	441.9	40.6
strain energy <sup>a</sup> of SWNT (kcal/mol nm)	72.8	1.8	96.5	0.9

<sup>a</sup> Obtained by comparing it to the initial structure.

## References

- (1) Javey, A.; Guo, J.; Wang, Q.; Lundstrom, M.; Dai H. *Nature* 2003, 424, 654.
- (2) Mann, D.; Javey, A.; Kong, J.; Wang, Q.; Dai, H. *Nano Lett.* 2003, 3, 1541.
- (3) Tans, S. J.; Verschueren, A. R. M.; Dekker C. *Nature* 1998, 393, 49.
- (4) Rosenblatt S.; Yaish, Y.; Park, J.; Gore, J.; Sazonova, V.; McEuen, P. L. *Nano Lett.*, 2002, 2, 869.
- (5) Seidel, R. V.; Graham, A. P.; Kretz, J.; Rajasekharan, B.; Duesberg, G. S.; Liebau, M.; Unger, E.; Kreupl, F.; Hoenlein, W. *Nano Lett.* 2005, 5, 147.
- (6) Cui, X.; Freitag, M.; Martel, R.; Brus, L.; Avouris, P. *Nano Lett.* 2003, 3, 783.
- (7) Austin, D. W.; Poretzky, A. A.; Geohegan, D. B.; Britt, P. F.; Guillorn, M. A.; Simpson, M. L. *Chem. Phys. Lett.* 2002, 361, 525.
- (8) Martel, R.; Derycke, V.; Lavoie, C.; Appenzeller, J.; Chan, K. K.; Tersoff, J.; Avouris, P. *Phys. Rev. Lett.* 2001, 87, 256805.
- (9) Marty, L.; Bouchiat, V.; Naud, C.; Chaumont, M.; Fournier, T.; Bonnot, A. M. *Nano Lett.* 2003, 3, 1115.
- (10) Frank, S.; Poncharal, P.; Wang, Z. L.; de Heer, W. A. *Science* 1998, 280, 1744.
- (11) Kanda, A.; Ootuka, Y.; Tsukagoshi, K.; Aoyagi, Y. *Appl. Phys. Lett.* 2001, 79, 1354.

- (12) Martel, R.; Schmidt, T.; Shea, H. R.; Hertel, T.; Avouris, P. *Appl. Phys. Lett.* 1998, 73, 2447.
- (13) Dag, S.; Gulseren, O.; Yildirim, T.; Ciraci, S. *Appl. Phys. Lett.* 2003, 83, 3180.
- (14) Shan, B.; Kyeongjae, C. *Phys. Rev. B* 2004, 70, 233405.
- (15) Tarakeshwar, P.; Kim, M. *J. Phys. Chem. B* 2005, 109, 7601.
- (16) Pomorski, P.; Roland, C.; Guo, H. *Phys. Rev. B* 2004, 70, 115408.
- (17) Durgun, E.; Dag, S.; Ciraci, S.; Gulseren, O. *J. Phys. Chem. B.* 2004, 108, 575.
- (18) Anantram, M. P.; Datta, S.; Xue, Y. *Phys. Rev. B* 2000, 61, 14219.
- (19) Schultz, P. A. *SEQQUEST code*; Sandia National Labs: Albuquerque, NM, 2005.  
<http://dft.sandia.gov/Quest/>.
- (20) Mattsson, A. E.; Schultz, P. A.; Desjarlais, M. P.; Mattsson, T. R.; Leung, K. *Modelling Simul. Mater. Sci. Eng.* 2005, 13, R1-R31.
- (21) Perdew, J. P.; Burke, K.; Ernzerhof, M. *Phys. Rev. Lett.* 1996, 77, 3865.
- (22) *CRC Handbook of Chemistry and Physics*, 87th ed.; CRC Press: Lide, D. R., Ed.; CRC Press: Boca Raton, FL, 2006.
- (23) Kim, Y. -H.; Jang, S. S.; Jang, Y. H.; Goddard, W. A. III. *Phys. Rev. Lett.* 2005, 94, 156801.
- (24) Kim, Y. -H.; Tahir-Kheli, J.; Schultz, P. A.; Goddard, W. A. III. *Phys. Rev. B* 2006, 73, 235419.

- (25) Muscat, J.; Wander, A.; Harrison, N. M. *Chem. Phys. Lett.* 2001, 342, 397.

## Supporting Information

### S1. Optimizing the Metal–Graphene Models

Optimized geometries of the top views and side views of (a) Ti, (b) Pd, (c) Pt, (d) Cu, and (e) Au deposited on a graphene  $4 \times 4$  sheet (Figure S1).

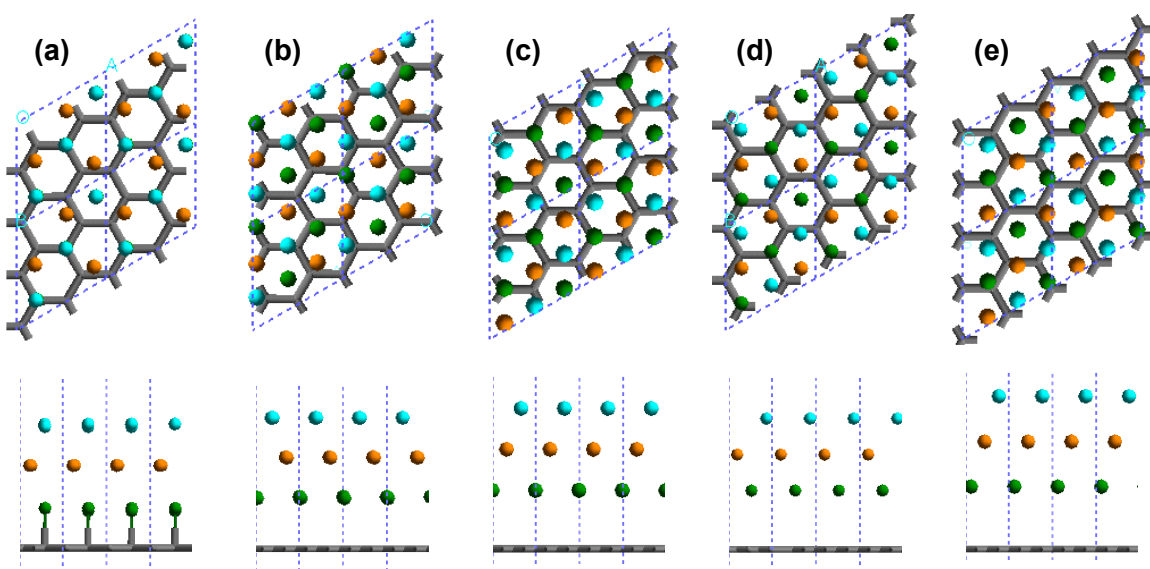


**Figure S1.** Optimized geometries of the top (top) views and side views (bottom) of (a) Ti, (b) Pd, (c) Pt, (d) Cu, and (e) Au deposited on a graphene  $4 \times 4$  sheet. (Unit cell for optimization is graphene  $2 \times 2$  sheet which is fixed at  $4.89 \times 4.89 \text{ \AA}$ ) (gray, graphite; green, metal first layer; orange, metal second layer; light blue, metal third layer).

To construct the models shown in Figure S1, we placed the atoms one by one, followed by relaxation of the geometry each time to represent the deposited metal on the graphite surface (Figure S2).

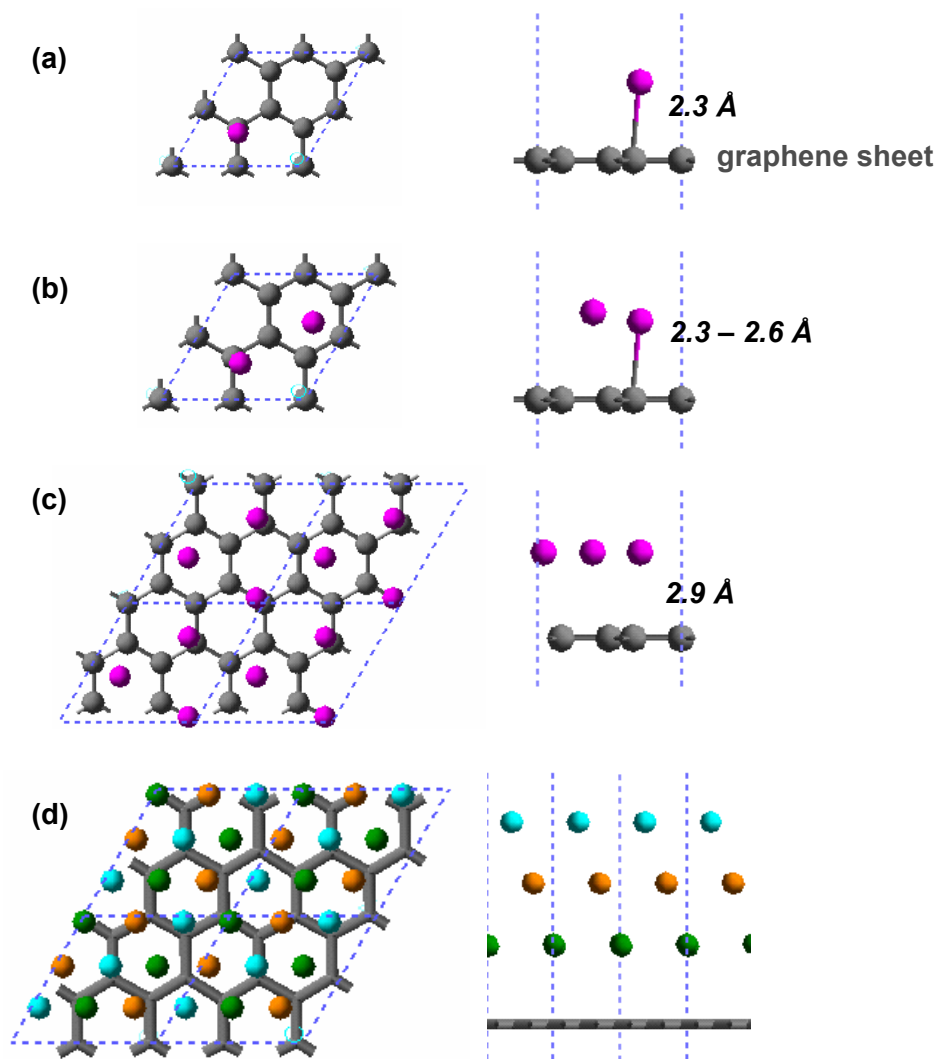


**Figure S2.** Optimization steps of the Pd-graphene model using a unit cell of graphene  $2 \times 2$  sheet which was fixed at  $4.89 \times 4.89 \text{ \AA}$ . The top views (left) and side views (right) are shown.

- (a) One Pd atom is added on the unit cell and relaxed.
- (b) Second Pd atom is added on the graphene unit cell and relaxed.
- (c) Third Pd atom is added on the graphene unit cell and relaxed, leading to an approximately closed-packed layer of metal. The top view shows the  $2 \times 2$  unit cell (graphene  $4 \times 4$  sheet).
- (d) The ABC stacking (face-centered cubic (fcc)) is found by adding the layers one by one (three atoms per layer per unit cell). The top and bottom views of the  $2 \times 2$  unit cell are shown. The metal–metal distances between each layer are within 10 % of the nearest neighbor distances of the bulk crystal structure (gray, graphite; green, metal first layer; orange, metal second layer; light blue, metal third layer).

## **S2. Comparison with Experimental Results**

It is difficult to compare the theoretical results and experimental data (Table S1) due to the following reasons:

1. The calculation models are constructed by assuming perfect geometries, but in experiment, the carbon nanotubes (CNTs) are bent and not fully contacted to the electrodes.
2. The referenced papers did not clearly define the device geometries and measurement conditions that were used.
3. The contact length or area was not stated in the referenced papers. Thus, the resistivity ( $\Omega$  nm) could not be calculated.

However, the experimental results seem to present the trend that Pd and Ti contacts are superior to Au and Pt contacts,<sup>1-9</sup> but the results for Ti are erratic possibly due to the high chemical reactivity of Ti compared to other metals.

**Table S1.** Comparison of Experimental Results. Resistance and Measurement Conditions in **Bold** are Mentioned in the Paper.

cont. <sup>a</sup>	geom. <sup>b</sup>	CNT <sup>c</sup>	resistance ( $\Omega$ ), temperature, $V_g^d$ and $V_{ds}^d$	cont. length (nm)	resistivity <sup>e</sup> ( $\Omega$ nm)	ref.
		m-SWNT	<b>8.6 k (4K), 32 k (270K)</b>		2.6 M (4K),	
Ti	Side	d = 1.7 nm L = 4 $\mu$ m	<b>10–100 k (fluctuate)</b> $V_g <  20V $ , $V_{ds} = 1$ mV	300 ?	3–30 M (270K)	2
		m-SWNT	<b>6.5 k (4K),</b> <b>10–20 k (270K)</b>		Q.C. <sup>f</sup> (4K),	
Pd	Side	d = 3 nm L = 0.3 $\mu$ m	$-10 < V_g < 0$ V, $V_{ds} = 1$ mV	$\sim 500^g$	5–10 M (270K)	2
		s-SWNT				
Pd	Side + End	d = 0.7–1.1 nm L = $\sim 20$ nm	47 k (?) $V_g = -5.4V$ , $V_{ds} = -0.4V$	$> 400^g$	19 M	5
		s-SWNT	<b>1.7 M (r.t. in air)</b>			
Pd	Side (top)	d = 1.3 nm L = 400 nm	$V_g = -10$ V, $V_{ds} \sim 0$ V	36	61 M	7
		m-SWNT	<b><math>\sim 1</math> M (r.t. in vacuum)</b>			
Pt	Side (top)	d = 1.4 nm L = 140 nm	<b>2 point cont (no <math>V_g</math>)</b> <b>(L = 140 nm, 550 k<math>\Omega</math>)</b>	140	77 M	3

Au	Side (top)	s-SWNT	100 M~1 G (r.t.? in air)	N/A <sup>h</sup>	6
		d = 1.4 nm	V <sub>g</sub> > 0, V <sub>ds</sub> = 0.5 V		
		L = 500 nm			
Au	Side (top)	s-SWNT	<b>Min. 1.1 M</b> , linear (r.t.)	N/A <sup>h</sup>	12
		d = 1.6 nm	V <sub>g</sub> < 0 V, V <sub>ds</sub> (saturated)		
		L = 300 nm			

<sup>a</sup> Contact (electrode) material.

<sup>b</sup> Side, “side-contacted”; End, “end-contacted”; top, CNT on top of the electrode.

<sup>c</sup> m-SWNT, metallic SWNT; s-SWNT, semiconductor SWNT.

<sup>d</sup> V<sub>g</sub>, gate voltage; V<sub>ds</sub>, source-drain voltage.

<sup>e</sup> Contact areas are estimated from the figures in the paper.

<sup>f</sup> Quantum conductance. For a SWNT, quantum conductance is  $4G_0$  ( $2G_0 \equiv 2e^2/h = 77.4 \text{ uA/V} = (12.9 \text{ k}\Omega)^{-1}$ , and there are two bands at the Fermi level).<sup>1,2</sup>

<sup>g</sup> Contact lengths are estimated from the figures on the paper.

<sup>h</sup> There are no figures which show device geometries.

## Chapter 2

# Improving Contact Resistance at the Nanotube–Cu Electrode Interface Using Molecular Anchors\*

### Abstract.

It is anticipated that future nanoelectronic devices will utilize carbon nanotubes (CNT) and / or single graphene sheets (SGS) as the low-level on-chip interconnects or functional elements. Here we address the contact resistance of Cu for higher level on-chip interconnects with CNT or SGS elements. We use first-principles quantum mechanical (QM) density functional and matrix Green's function methods to show that perfect Cu–SGS contact has a contact resistance of 16.3 M $\Omega$  for a one square nanometer contact. Then we analyzed possible improvements in contact resistance through incorporation of simple functional groups such as aryl (–C<sub>6</sub>H<sub>4</sub>–), acetylene (–CC–), carboxyl (–COO–), and amide (–CONH–), on CNT. We find that all four anchors enhance the interfacial mechanical stabilities and electrical conductivities. The best scenario is –COOH functionalized CNT which reduces the contact resistance to the Cu by a factor of 275 and increases the mechanical stability by 26 times.

---

\*Matsuda, Y.; Deng, W.-Q.; Goddard, W.A. III. “Improving Contact Resistance at the Nanotube–Cu Electrode Interface Using Molecular Anchors”. Published in *J. Phys. Chem. C.*, *112*, 11042, **2008**.

## 1. Introduction

The unique structures and excellent properties of carbon nanotubes (CNT) and single graphene sheets (SGS) provide promising applications to nanoelectronic devices.<sup>1-5</sup> For example, they are promising candidate materials for the low-level on-chip interconnect metals of future integrated circuits, because they address issues such as delays in signal propagation and density and scaling of process integration, which are currently limited by Cu and Al metal wires. However, applications of CNT and SGS to future nanoelectronics present a plethora of potential problems in developing assembly techniques suitable to pattern CNTs at desired positions on a wafer with high accuracy and reproducibility and to connect them to the higher level on-chip interconnects, while maintaining their distinguished electrical properties. In this paper, our primary concerns are improving the mechanical stabilities and contact resistance at the interfaces between CNT or SGS and other metals when constructing multiple level on-chip interconnects.

Copper is currently the leading on-chip interconnect for integrated circuits using fabrication processes established in the 1990s that have been well-studied and improved since then.<sup>6-9</sup> Advantages of Cu are that have led to its extensive use in electronics is that it has the second highest electrical conductivity of pure metals and is abundant and inexpensive. Thus, it would be most desirable to connect Cu electrodes directly to the CNT or SGS. However, our previous studies showed that Cu–CNT interfaces lead to extremely high contact resistance ( $16.3 \text{ M}\Omega/\text{nm}^2$ ), 672 times worse than Ti ( $24.2 \text{ k}\Omega/\text{nm}^2$ ) or 74 times worse than Pd–CNT interface ( $221.3 \text{ k}\Omega/\text{nm}^2$ ).<sup>10</sup> In addition it is mechanically weak.<sup>10</sup> In this paper, we show that this problem with Cu can be solved by incorporating functional linkers, which we describe as “anchors”, between Cu electrodes

and the CNT or SGS that can bond covalently to the Cu, dramatically decreasing the contact resistance, while increasing the mechanical stability.

For functionalized CNT applications, experimental studies have reported solubility enhancement of multiwalled and single-walled CNTs by dissociation of functionalized CNT bundles in various solvents such as water<sup>11,12</sup> and alcohol<sup>13</sup>. Functionalized CNTs have also been used as biological sensors by utilizing their high reactivity to amines or amides and because of their small dimensions.<sup>12</sup> In addition, some attempts have been made to utilize functionalized CNTs for self-assembly processes on substrates.<sup>14–16</sup> There have been several theoretical studies about the fundamental properties of functionalized CNTs,<sup>17–19</sup> yet there has been no study of the comparison of the mechanical and electrical properties of the appropriate anchors except for our initial report about functional anchors between Pt contacts and CNTs.<sup>20</sup>

Lastly, we illustrate some of the synthetic strategies that might be useful for incorporating the Cu–anchor–CNT elements into nanoelectronics.

## **2. Methods**

### **2.1. Modeling Details.**

The Cu–anchor–graphene configuration is shown in Figure 1a. It was also chosen to be our simplified model of the Cu–anchor–CNT concept (Figure 1b) and allows us to focus on the local interfacial structures and contact resistance ( $R_C$ ) properties in this paper. The total resistance of a CNT ( $R_T$ ) is often expressed as  $R_T = R_C + R_{NT} + \text{scattering}$ , where  $R_{NT}$  represents the resistance of the CNT.<sup>21</sup> For our simple models,  $R_T = R_C + R_G$ , where

$R_G$  is the contact resistance of two layers of graphene with a fixed distance of 3.4 Å and  $R_C$  is the contact resistance which we used for each of the different anchors, which are the main properties studied in this paper. The scattering term can be ignored since the distance is much smaller than the mean free path of an electron. Additionally, our previous work showed that metal–graphene models accurately represent metal–CNT models for all geometric considerations except for the distance between the CNT and electrodes which is slightly smaller (1.9–2.8 %) than the graphene case, indicating that the larger attractive interaction is due to the incursion of the s hybrid character in the  $p\pi$  orbital caused by the curvature of the CNT. Considering all of these issues, we believe that our models are appropriate for our purpose of study.

The model geometries were carefully optimized using the following steps: (1) Cu–anchor models were optimized to find the most stable binding sites and molecule species of the anchor molecules on the Cu(111) surface. For acetylene, carboxyl, and amide anchors, the  $\text{CH}_3$  group was attached at the end of the anchor molecules to replace the carbon on the graphene in step 3. (2) Graphene–anchor models, including the effects of the resonance positions, were optimized. (3) Cu(111)–anchor–graphene models for the current–voltage ( $I$ – $V$ ) calculations were fully optimized.

We chose a  $4 \times 4$  unit cell (32 carbons per layer) of a graphene sheet (fixed at  $0.98 \times 0.85 \text{ nm}^2$ ) to have large enough spacing to avoid interactions between anchor molecules. The quantum mechanical (QM) optimized Cu(111) layers with ABC stacking (fcc) deposited on top of a graphene sheet, which were calculated in our previous study, were used to represent Cu metal layers so that the periodic spacing of Cu metal matched with the graphite surface.<sup>10</sup> The Cu–Cu distances of the deposited Cu layers are within 5 % of the

nearest neighbor distance of the bulk crystal structure. For all optimizations, three layers of Cu were used with the second and third layers being held fixed.

## 2.2. Choice of Anchors.

We chose the simple functional groups, such as aryl ( $-\text{C}_6\text{H}_4-$ ), acetylene ( $-\text{CC}-$ ), amide ( $-\text{CONH}-$ ) and carboxyl ( $-\text{COO}-$ ), as anchor candidates to bind between Cu surfaces and CNTs. All anchor candidates have been reported to functionalize CNT side walls in experiments.<sup>22-25</sup> A variety of aryl functionalized CNTs can be synthesized using aryldiazonium salts, and the estimated surface coverage is 1 out of approximately 20 carbons<sup>23</sup> or even up to 9 carbons<sup>24</sup>, which can lead to an increase in solubility in organic solvents. The alkylated CNTs are synthesized using lithium and alkyl halides in liquid ammonia, which are also soluble in common organic solvents as well.<sup>24</sup> The carboxyl groups can be introduced on the CNTs by sonicating in 3:1 sulfuric/nitric acid solvents for 3 h at 273 K, and further treatment by ethylenediamine and the coupling agent produces the amido functionalized CNTs.<sup>25</sup> Although our primary goal is to find a good interface between Cu and CNTs or SGSs, we believe this study also provides useful results for fundamental surface physics.

### 2.3. Computational Details.

We used SEQUEST<sup>26</sup>, a fully self-consistent Gaussian-based linear combination of atomic orbitals (LCAO) density functional theory (DFT) method with double- $\zeta$  plus polarization (DZP) basis sets.<sup>27</sup> All calculations were based on the Perdew–Burke–Ernzerhof (PBE) generalized gradient approximation (GGA) with PBE pseudo atomic potentials and spin polarization within 2D periodic boundary conditions.<sup>28</sup> The  $k$ -point sampling of  $4 \times 4$  in the Brillouin zone and the real space grid interval of  $53 \times 60$  in the  $x$ - $y$  plane, for a grid spacing of  $0.30 \text{ bohr}^{-1}$  per point, were carefully determined by energetic convergence.

To obtain  $I$ - $V$  characteristics of each model, the density of state (DOS) was obtained from DFT quantum mechanics, while the transmission coefficient was obtained using matrix Green's function theory with DFT (which we have used successfully to compute transport properties of molecular electronic devices).<sup>29</sup> The transmission function was then used in the Landauer–Buttiker formula to calculate the  $I$ - $V$  characteristics. The zero-bias transmission  $T(E, V = 0)$  approximation is applied to the computation of the current  $I$  at a finite bias voltage ( $V$ ). The finite- $V$  transmission  $T(E, V)$  should be close to  $T(E)$  at a low bias voltage of  $-0.1$  to  $0.1 \text{ V}$ , which would be the region of the device operation studied in this paper. The large- $V$  region ( $V > 0.5 \text{ V}$ )  $I$ - $V$  curves should be taken as qualitative.

### 3. Results

#### 3.1. Optimization of Cu–Anchor Models.

For the modeling of the Cu–benzene anchor, we optimized the geometries of benzene ( $C_6H_6$ ) on top of Cu atom (atop), face-centered cubic (fcc), hexagonal close-packed (hcp) and bridge site to find the most stable binding site on the Cu(111) surface (Figure 2). When bonding the benzene to the Cu(111) surface, one hydrogen atom is removed from benzene, forming a phenyl. We calculated snap bond energies and difference in the energies (relative energies) in which the lowest energy is defined as 0 kcal/mol (Table 1). The most stable binding site on the Cu(111) for  $C_6H_5-$  is found to be at the bridge site with a bond energy of 46.9 kcal/mol, which is slightly more favorable than the hcp site by 0.4 kcal/mol, the fcc site by 1.6 kcal/mol, and the atop site by 1.7 kcal/mol. The perpendicular separation between the Cu(111) surface and anchor is 1.81 Å at the bridge site, which is the smallest of all the anchors.

In a similar manner to the benzene modeling, the acetylene anchor with optimized geometries for propyne ( $(CH)_3CCH$ ) on atop, fcc, hcp, and bridge sites were used to find the most stable binding site on Cu(111) by removing one hydrogen atom bonded to the acetylene (Figure 3). The methyl, bounded at the end of the acetyl to replace the carbon on the graphene, is used to clarify the bond directions. We again calculated snap bond energies and  $\delta$  energies in which the highest energy is defined as 0 kcal/mol (Table 2). The most stable binding site on the Cu(111) for propyne is found to be at the fcc site with a bond energy of 103.5 kcal/mol, which is slightly more favorable than the hcp site by 0.7 kcal/mol and is much more stable than the atop site by 14.7 kcal/mol, indicating that the threefold sites provide a preferable overlap of the orbitals between Cu on the Cu(111)

surface and carbon on propyne. The perpendicular separation between the Cu(111) surface and anchor is 1.37 Å at the fcc site, which is the smallest distance for all the anchors.

For the amide anchor,  $(\text{CH}_3)\text{CONH}_2$ , on top of the Cu(111) surface with or without hydrogen atoms was optimized to choose the most stable molecule which bonds to the Cu(111) surface (Figure 4), and the snap bond energies and  $\delta$  energies were calculated (Table 3). One hydrogen atom is placed on the Cu surface for the  $(\text{CH})_3\text{CONH}$  model, and two hydrogen atoms are placed on the Cu surface for the  $(\text{CH})_3\text{CON}$  to enable comparison of the total energies of all the models. We found that  $(\text{CH}_3)\text{CONH}$  bonds to the Cu(111) surface with the snap bond energy of 122.2 kcal/mol, which is more energetically favorable than  $(\text{CH}_3)\text{CONH}_2$  and  $(\text{CH}_3)\text{CONH}$ . In the  $(\text{CH}_3)\text{CONH}$  model, the O atom is on the top of the Cu atom, the N atom is in the bridge position between two Cu atoms, and the perpendicular separation between Cu(111) surface and anchor is 1.58 Å.

Lastly, the carboxyl anchor,  $(\text{CH}_3)\text{COOH}$ , on top of Cu(111) surface with or without a hydrogen atom was optimized to choose the most stable molecule which bonds to the Cu(111) surface (Figure 5). One hydrogen atom was added to the surface of Cu(111) for the  $(\text{CH})_3\text{COO}$  model to compensate for the missing hydrogen atom and to enable a comparison of the total energy with  $(\text{CH}_3)\text{COOH}$  by calculation of the snap bond energies and  $\delta$  energies (Table 4). We find that the  $(\text{CH}_3)\text{COOH}$  molecule does not bond to the Cu(111) surface due to the stability of the molecule itself, which also confirms that the calculations are being carried out reasonably. On the contrary,  $(\text{CH}_3)\text{COO}$  bonded to the Cu(111) surface with a snap bond energy of 70.3 kcal/mol, with one O atom on the

top of the Cu atom and the other O atom in the bridge position between two Cu atoms, with a perpendicular separation between the Cu(111) surface and anchor of 1.75 Å.

### 3.2. Optimizations of Graphene–Anchor Models.

Previous theoretical studies have reported that chemical bonding of a functionalizing molecule to the side wall of a CNT creates a half-filled band near the Fermi energy because of an unpaired spin of the  $p\pi$  orbital of a carbon–carbon bond.<sup>17–19</sup> Since  $I$ – $V$  characteristics at the interface are a critical issue in this paper and the unrealistic half-filled band near the Fermi energy can cause overestimation of the conductance, we carefully studied the resonance effects of anchors on a graphene sheet unit cell to determine the energetically favorable states.

To examine this issue, the difference in bond energies between resonance and nonresonance positions was calculated by bonding two acetylene molecules ( $C_2H_2$ ) on the graphene sheet and removing one hydrogen atom. The graphene unit cell consists of 32 carbon atoms with a fixed area of  $0.98 \times 0.85 \text{ nm}^2$ . When placing one acetylene anchor on the graphene unit cell (shown with a red solid circle (Figure 6a)), there are nine resonance positions (a, b, and c) and nine nonresonance positions (d, e, and f). Each alphabet notation represents the equivalent distance from the carbon atom which the first acetylene anchor is bonded to. For example, when the second acetylene anchor is bonded to the a3 site as shown in Figure 6b, the two acetylene anchors (5.1 Å separation) are in resonance positions. In contrast, the second acetylene anchor is bonded to the d5 site (4.2 Å separation), which shows the nonresonance states, and leaves a free radical on the

graphene sheet (Figure 6c). Acetylene positions which are within 2.8 Å of the first acetylene anchor (enclosed by the red line in Figure 6a) are not considered in order to avoid the large steric interactions between molecules.

To summarize the computational results, the adiabatic and snap bond energies measured by adding one acetylene and two acetylene molecules are shown in Chart 1 and Table 5. We calculated the adiabatic bond energies as a reference in order to exclude the significant effect of the strain energies in the graphene sheet. According to Table 5, the average adiabatic bond energy of the second addition of the acetylene molecule at resonance positions obtains larger energy than that of the first acetylene molecule by 13.0 kcal/mol, whereas that of nonresonance positions are lower by 4.4 kcal/mol. The results illustrate clearly that the addition of the second anchors in a resonance position stabilizes the total graphene–anchor models. According to this result, a hydrogen atom is added in the resonance position of the a3 site on the graphene unit cell for all anchor calculations to avoid creating an unrealistic half-filled band or a lowest unoccupied molecular orbital (LUMO) which affects the QM  $I-V$  calculations.

By taking into account the resonance effect described above, the graphene–anchor models are optimized by removing one hydrogen atom from each anchor and placing it on the resonance position (a3) of the graphene unit cell (Figure 7). For all anchors, atop sites are found to be favorable. The snap bond energy between the anchor and graphene and the graphene strain energy, which is due to the deformation of the graphene sheet by the bonding of both the anchor and H atom, are shown in Table 6. The largest snap bond energy is for acetylene with 82.6 kcal/mol, followed by benzene (58.9 kcal/mol), carboxyl (50.5 kcal/mol), and amid (42.0 kcal/mol).

### 3.3. Optimization of Cu(111)–Anchor–Graphene Models and Construction of $I$ – $V$ models.

Finally, we fully optimized the geometries of the Cu(111)–anchor–graphene models. The total snap bond energies of all four anchors are largest for acetylene anchor (168.9 kcal/mol), followed by carboxyl (123.9 kcal/mol), amide (117.8 kcal/mol), and benzene (106.1 kcal/mol) (Table 7). The perpendicular separations between the Cu(111) surface and graphene are significantly larger for benzene (7.03 Å) due to its configuration, whereas the rest of the separations have similar values. Looking at the results in more detail, the acetylene–Cu surface separation (1.33 Å) is smaller than the benzene–Cu surface separation (1.97 Å), the amide–Cu surface separation (1.88 Å), and the carboxyl–Cu surface separation (2.03 Å). The acetylene–graphene separation (1.48 Å) is also the shortest of all anchor separations ( $1.61 \pm 0.03$  Å).

To enable a direct comparison of the contact resistance at the interface between each anchor model and graphene,  $I$ – $V$  models were constructed from the optimized geometries by reversing one of the models and placing it at the AB stacking positions of the original graphene sheet as shown in Figure 8. The three Cu(111) layers represent the two electrodes (source and drain) of a CNT or SGS. The contact resistance of the pure Cu–graphene (no anchor) was calculated in our previous study (Figure 8e).<sup>10</sup> The distance between the two graphene sheets was fixed at 3.4 Å, which is specified by the experimental data.<sup>30</sup>

### 3.4. Contact Resistance of Cu(111)–anchor–graphene Models.

For all Cu(111)–anchor–graphene models, the DOS (Figure 9a) are higher than the Cu–graphene (no anchor) model, indicating improved conduction channels at the interface. The transmission coefficients near the Fermi energy (Figure 9b) and the strength of the amide, carboxyl, acetylene, no anchor, and benzene models are listed in descending order. Benzene shows a very small transmission coefficient which indicates that there is no appropriate orbital for current flow between the electrodes.

In turn, the  $I$ – $V$  characteristics (Figure 9c) and total resistance per unit area (Figure 9e) correlate directly with the transmission coefficient. We calculate contact resistances of 43 k $\Omega$  for carboxyl anchor, 58 k $\Omega$  for amide anchor, 128 k $\Omega$  for acetylene anchor, 10.3 M $\Omega$  for benzene anchor, and 11.7 M $\Omega$  per unit cell ( $0.98 \times 0.85 \text{ nm}^2$ ) for Cu without anchor after averaging for a bias voltage from  $-0.1$  to  $0.1$  V (Table 8), where the bias voltage is defined as the difference between the source and the drain voltage. These values should be interpreted as a relative evaluation of these models.

## 4. Discussion

### 4.1. Mechanical Stabilities and Electrical Enhancements by Choice of Anchors.

The interaction energies (Table 7) indicate that all anchors are good candidates for enhancing the mechanical stabilities of the Cu–CNT interface as compared to that of the Cu without anchor which has an interaction energy of 4.8 kcal/mol with a separation of 3.30 Å.<sup>10</sup> The acetylene anchor obtains the largest mechanical stability of all others because of the strong cohesive energy, which is also represented by the short separations to the Cu(111) surface and graphene. The snap bond energy of benzene anchor is smaller than that of acetylene anchor by 62.8 kcal/mol, and the separations between anchor–Cu(111) and anchor–graphene are larger by 1.48 times and 1.07 times, respectively, which is possibly due to the steric interactions between the benzene and the surfaces. The snap bond energies of amide and carboxyl anchors are relatively smaller than that of the acetylene anchor since the anchor ions are stabilized by resonance effects.

We also find that the second anchor bonds to the resonance position on the graphene unit cell to gain stability, which is also true for the CNT surface. More energetically favorable bonding at the a3 site and less favorable bonding at the c site within the resonance positions (Table 5) may be of further interest in the study of the effects of geometric symmetries or arene substitution patterns. However, since the primary focus of this paper is to construct reasonable models for the study of contact resistance, we will not pursue the discussion of this subject any further within the paper.

By applying the carboxyl anchor, the contact resistance can be reduced by a factor of approximately 270 when compared to that of pure Cu electrodes. From our previous

study, the contact resistance of the Pd–graphene (no anchor) is calculated as 159 k $\Omega$  per unit cell ( $0.98 \times 0.85 \text{ nm}^2$ ).<sup>10</sup> Hence, the carboxyl, amid, and acetylene anchors can improve the contact resistance better than the Pd electrodes.

Interestingly, the contact resistance for the benzene anchor is essentially the same as without the anchor. This is because the benzene leads to a total tunneling distance of 7.03 Å which is approximately 50 % larger than the other three cases. The experimentally reported anchors applied in self-aligning assemblies, such as sodium dodecyl sulphate (SDS)<sup>12</sup> and long-chained aryldiazonium salts<sup>13</sup> which possess long alkyl chains (C<sub>12</sub> and C<sub>11</sub>, respectively) leading the large separations, are likely to dramatically increase the contact resistance.

#### **4.2. Outline of Proposed Process Steps.**

The outline of processing steps that might be used to implement the assembly of CNT–anchor–Cu electrode systems is illustrated in Scheme 1. There have been studies which reported ways to implement the CNTs at a specific place on the wafer by functionalizing the CNTs<sup>14, 15</sup> or by functionalizing the surface of the substrate<sup>31</sup> or both<sup>16</sup>. Some of the functional molecules from the CNT surface can be successfully removed, and pristine CNTs are restored (Scheme 1a).<sup>15, 16</sup> After this process, the CNTs can be masked for the implementation of the electrodes to avoid unfavorable deformations of the CNTs (Scheme 1b), followed by treatment with anchor precursors (Scheme 1c). This step should be realized easily since there have already been experimental reports of the

functionalized CNTs with the anchors as we stated previously.<sup>21–24</sup> Finally, the Cu electrodes can be deposited on top of them and the masks can be removed (Scheme 1d).

## 5. Conclusion

The use of QM methods shows that appropriate anchors can dramatically reduce the contact resistance of Cu–CNT and Cu–SGS interfaces, while increasing mechanical stability. Of the four anchors we considered, the best Cu interface is carboxyl (275 times lower contact resistance and 30 times higher mechanical stability than the perfect Cu–SGS interface), followed by amide, acetylene, and benzene in descending order. We find that introducing the carboxyl anchor at the Cu–SGS interface improves the contact resistance by 3.7 times compared to the Pd–SGS interface without an anchor, making the Cu electrodes a good candidate for the CNT or SGS electronics.

Scheme 1 illustrates the processing steps that might be used to implement the self-assembly of CNT–anchor–Cu electrode systems. In this section, most of the steps for constructing self-assembling CNT–anchor–Cu electrode systems are shown.

We recommend that the anchors are to be selected to reduce the contact resistance as demonstrated here in the detailed calculations for four functional groups. They provide useful guidelines for selecting molecular anchors for carbon black and other graphite materials in addition to CNT and SGS. Our studies, which have shown first-principle predictions of complex phenomena in nanoscale materials and devices, may be used as a protocol for choosing the appropriate experimental materials and processes.

**Acknowledgements.**

We thank Dr. Jamil Tahir-Kheli for helpful discussions. This work was supported partially by Intel Components Research (Kevin O'Brien, Florian Gstrein, and James Blackwell) and by National Science Foundation (CCF-0524490 and CTS-0608889). The computer systems used in this research were provided by ARO-DURIP and ONR-DURIP. Additional support for the MSC was provided by ONR, ARO, DOE, NIH, Chevron, Boehringer-Ingelheim, Pfizer, Allozyne, Nissan, Dow-Corning, DuPont, and MARCO-FENA.

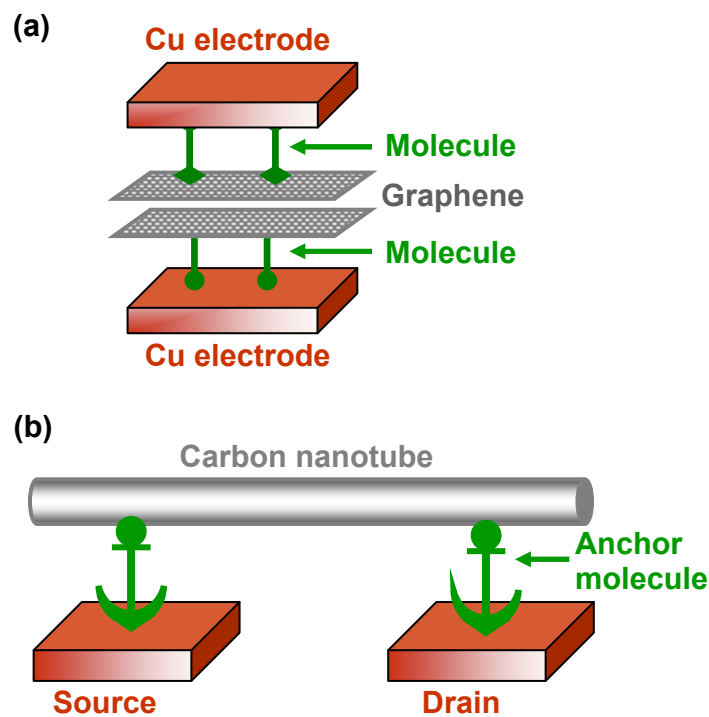


**Figure 1.** (a) Cu–anchor–graphene configuration for our simplified simulation model. (b) Proposed Cu–anchor–CNT concept to focus on the local interfacial structures and the contact resistance ( $R_C$ ) properties.

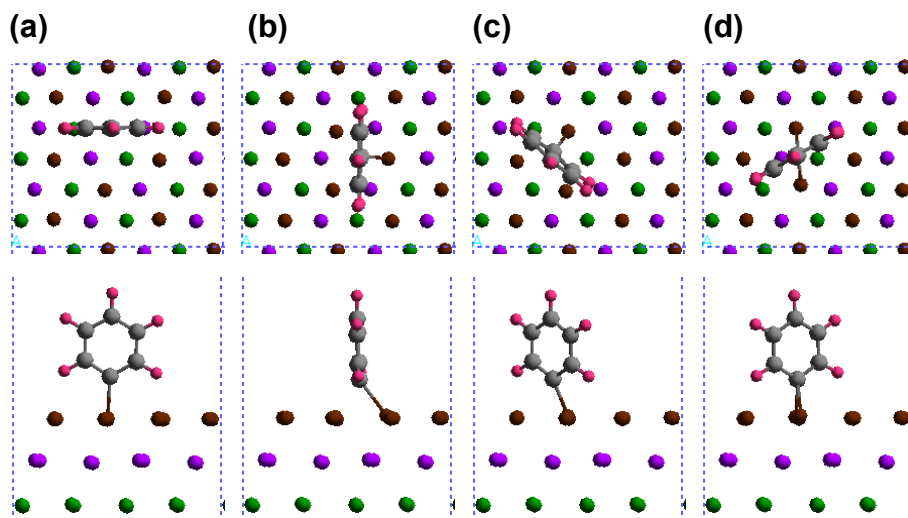


**Figure 2.** Optimized geometries of the top (top) and side (bottom) views of  $C_6H_5-$  Cu(111) surface: (a) atop, (b) fcc, (c) hcp, and (d) bridge sites on the Cu(111) unit cell of  $0.98 \times 0.85 \text{ nm}^2$ . The bridge site is found to be the most stable site (gray, carbon; pink, hydrogen; brown, Cu top layer; purple, Cu second layer; green, Cu third layer). The energies and geometric parameters are given in Table 1.

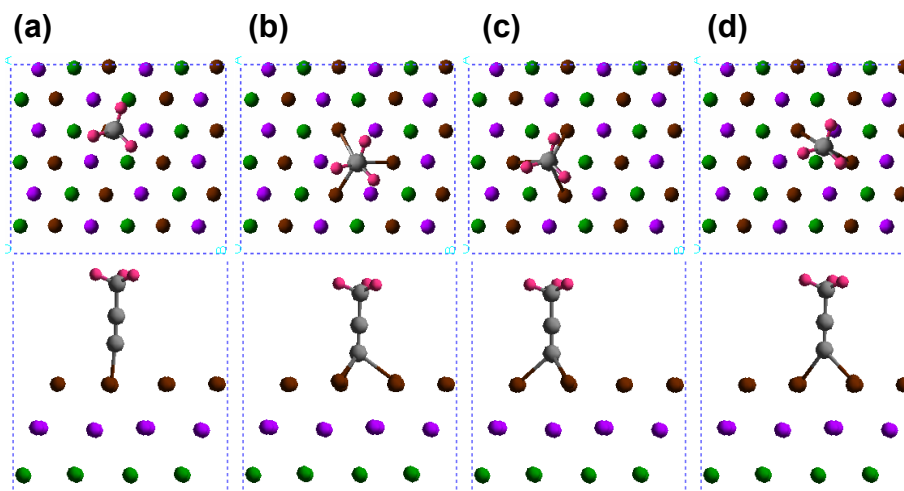


**Figure 3.** Optimized geometries of the top (top) and side (bottom) views of  $(\text{CH}_3)\text{CC}$ –Cu(111) surface: (a) atop, (b) fcc, (c) hcp, and (d) bridge sites on the Cu(111) unit cell. The fcc site is found to be the most stable site (gray, carbon; pink, hydrogen; brown, Cu top layer; purple, Cu second layer; green, Cu third layer). The energies and geometric parameters are given in Table 2.

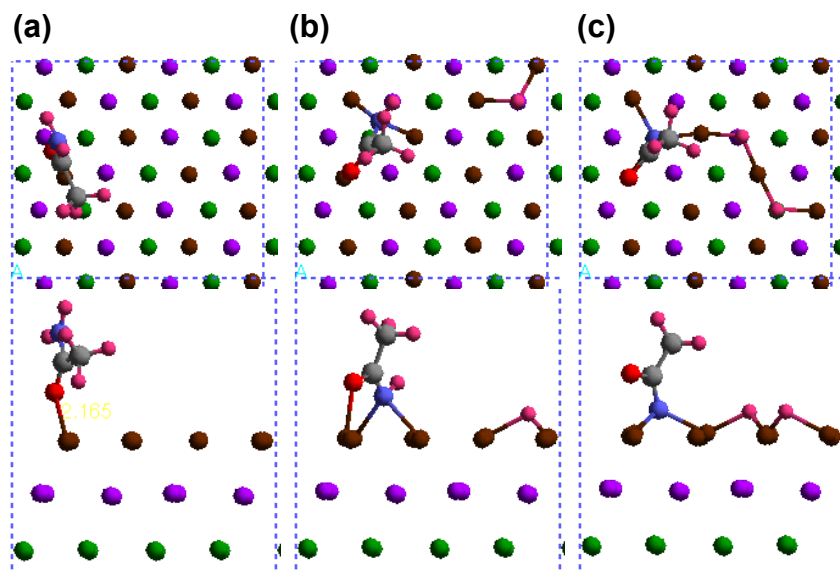


**Figure 4.** Optimized geometries of the top (top) and side (bottom) views of (a) (CH<sub>3</sub>)CONH<sub>2</sub>, (b) (CH<sub>3</sub>)CONH, and (c) (CH<sub>3</sub>)CON on the Cu(111) surface unit cell.

Chemisorbed hydrogen atoms are included for (b) and (c) for comparing the energetics of the unit cell (gray, carbon; pink, hydrogen; red, oxygen; blue, nitrogen; brown, Cu top layer; purple, Cu second layer; green, Cu third layer). The energies and geometric parameters are given in Table 3.

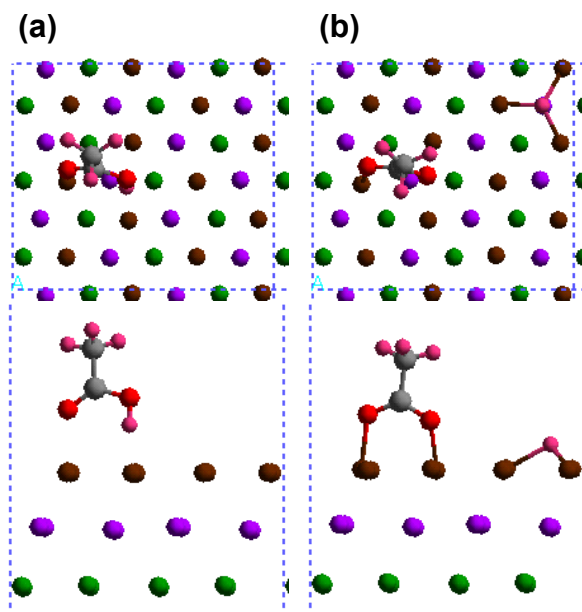


**Figure 5.** Optimized geometries of the top (top) and side (bottom) views of (a)  $(\text{CH}_3)\text{COOH}$  and (b)  $(\text{CH}_3)\text{COO}$  on the Cu(111) surface unit cell.

A chemisorbed hydrogen atom is added for (b) to compare the energetics (gray, carbon; pink, hydrogen; red, oxygen; brown, Cu top layer; purple, Cu second layer; green, Cu third layer). The energies and geometric parameters are given in Table 4.

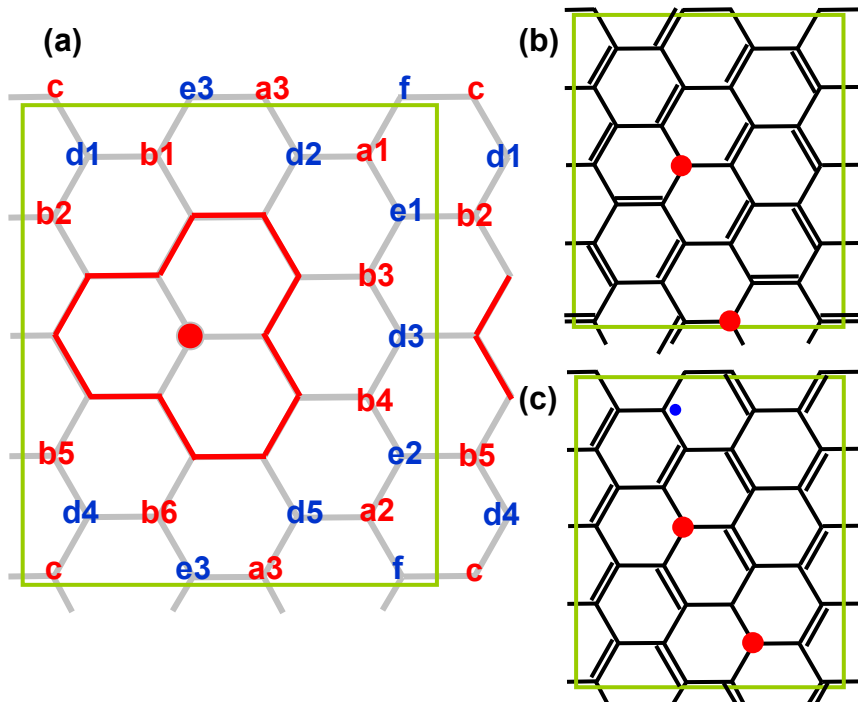


**Figure 6.** Top views of the graphene unit cell ( $0.98 \times 0.85 \text{ nm}^2$ , shown with a green line) used to evaluate the resonance effects by bonding the anchor molecules.

(a) Resonance (a, b, and c) and nonresonance (d, e, and f) positions when placing one acetylene anchor on the graphene unit cell (shown with a red solid circle). The red line shows a distance smaller than  $2.8 \text{ \AA}$ , which shows large steric interactions. (b) The second acetylene anchor is bonded to the a3 (resonance) site. (c) The second acetylene anchor is bonded to the d5 (nonresonance) site and a free radical is shown with a blue dot. The energies and geometric parameters are given in Table 5.

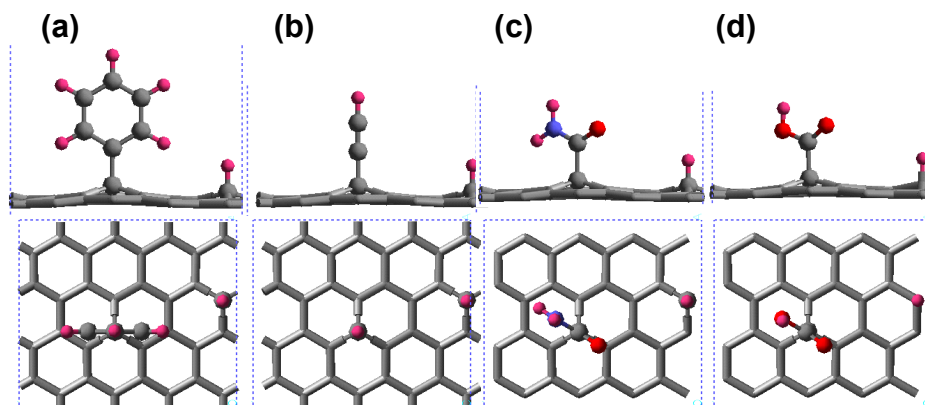


**Figure 7.** Optimized geometries of the side (top) and top (bottom) views of (a)  $C_6H_5$ , (b)  $HCC$ , (c)  $CONH_2$ , and (d)  $COOH$  on graphene unit cell ( $0.98 \times 0.85 \text{ nm}^2$ ).

Hydrogen atoms are added in the resonance positions (gray, carbon; pink, hydrogen; red, oxygen; blue, nitrogen; brown, Cu top layer; purple, Cu second layer; green, Cu third layer). The energies and geometric parameters are given in Table 6.

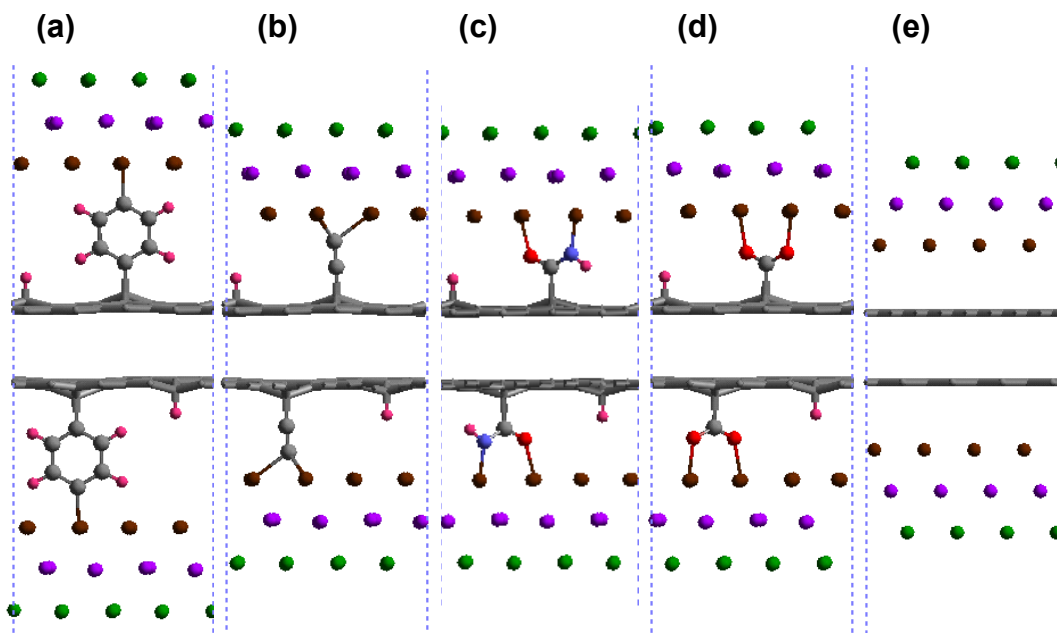


**Figure 8.** Side views of  $I$ - $V$  calculation models which were constructed from the optimized Cu(111)-anchor-graphene models by reversing one of the models and placing it at the AB stacking positions of the original graphene sheet.

(a) Cu(111)-C<sub>6</sub>H<sub>4</sub>-graphene-graphene-C<sub>6</sub>H<sub>4</sub>-Cu(111), (b) Cu(111)-CC-graphene-graphene-CC-Cu(111), (c) Cu(111)-CONH-graphene-graphene-CONH-Cu(111), (d) Cu(111)-COO-graphene-graphene-COO-Cu(111) and (e) Cu(111)-graphene-graphene-Cu(111) (gray, carbon; pink, hydrogen; red, oxygen; blue, nitrogen; brown, Cu top layer; purple, Cu second layer; green, Cu third layer).

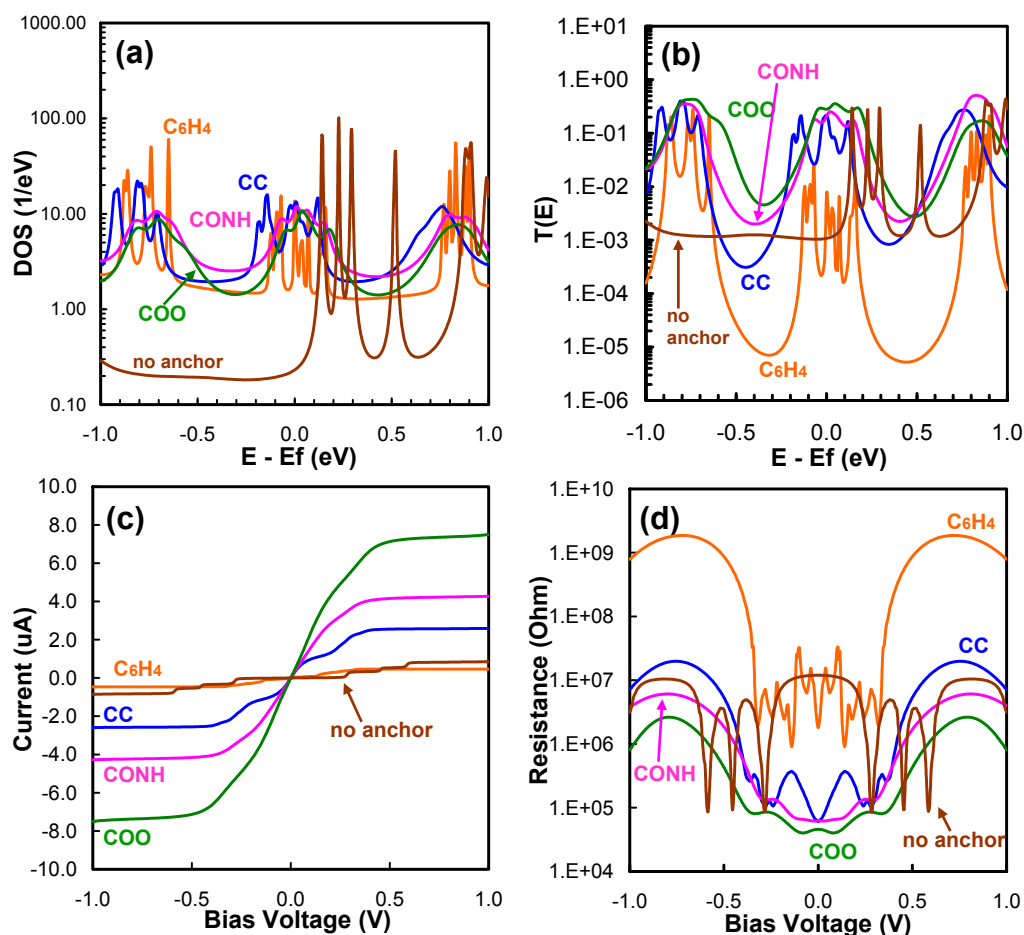
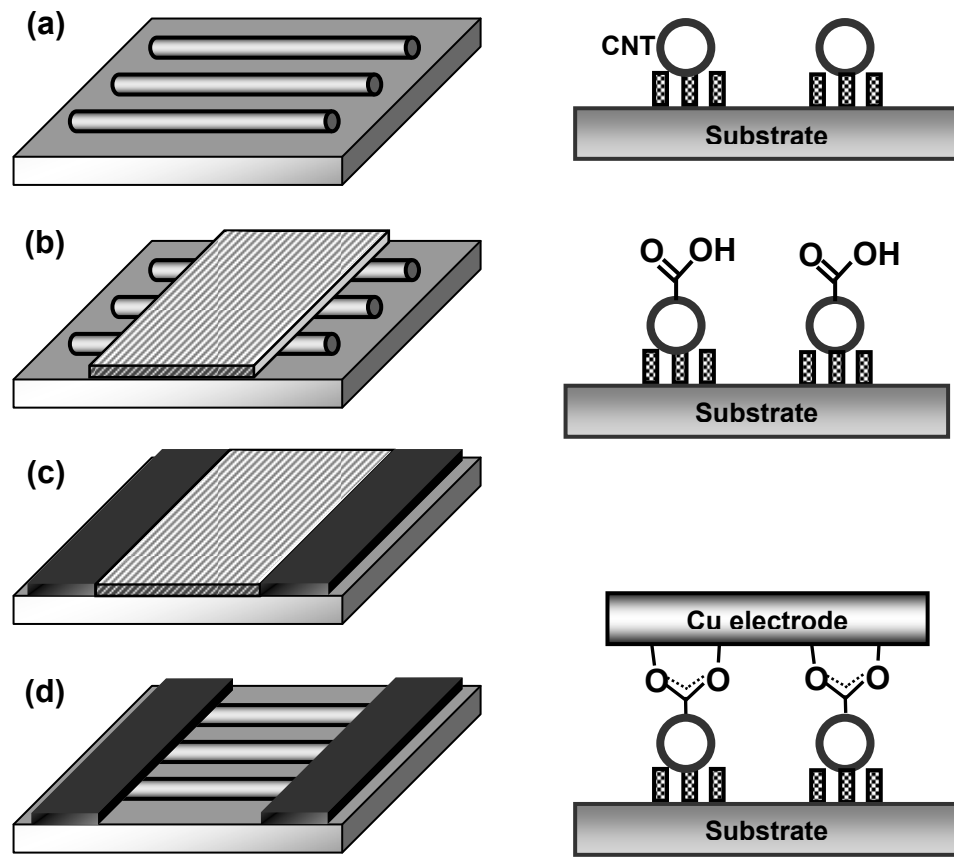


**Figure 9.**  $I$ - $V$  characteristics of Cu(111)-anchor-graphene-graphene-anchor-Cu(111) models (Figure 8) per unit cell ( $0.98 \times 0.85 \text{ nm}^2$ ).

(a) Density of states (1/eV/unit cell) near the Fermi energy. (b) Transmission coefficient ( $T(E)$ ). (c)  $I$ - $V$  curve. (d) Contact resistance (orange,  $-\text{C}_6\text{H}_4-$ ; blue,  $-\text{CC}-$ ; pink,  $-\text{CONH}-$ ; green,  $-\text{COO}-$ ; brown, no anchor).



**Scheme 1.** Proposed Steps for Forming Cu–Anchor–CNT Interconnect

- (a) Implementation of the CNTs at a specific place on the wafer.
- (b) CNTs can be masked for the implementation of the electrodes.
- (c) Treatment with anchor precursors, followed by the deposition of Cu electrodes.
- (d) Removal of masks.

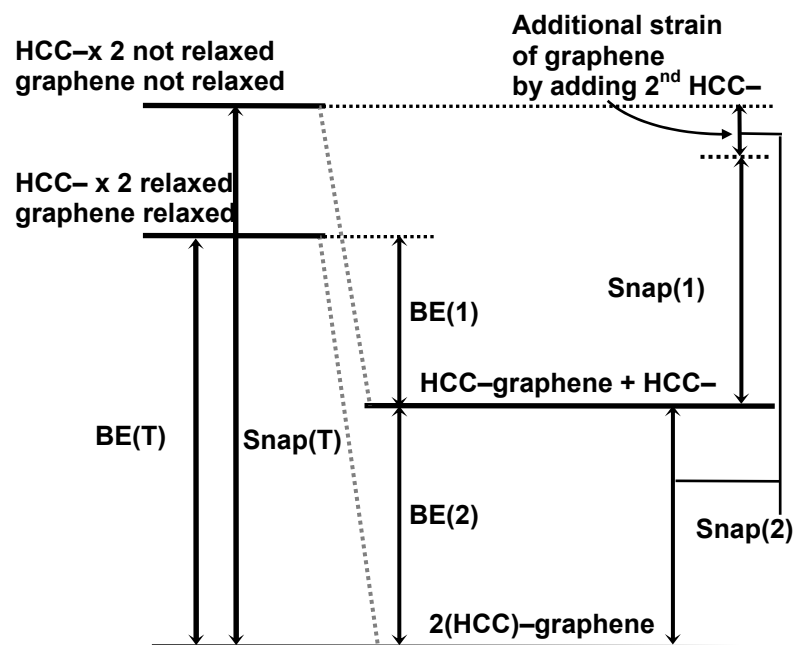


**Chart 1.** Adiabatic and Snap Bond Energetics Measured by Adding Acetylene Anchors (HCC-) on the Graphene Unit Cell ( $0.98 \times 0.85 \text{ nm}^2$ )

BE is adiabatic bond energy.

Snap is bond energy, not allowing the fragments to relax.

(T), energy by adding two HCC-; (1), energy by adding the first HCC-; (2), energy by adding the second HCC-.

**Table 1.** Energetics and Geometry between  $-C_6H_5$  Anchor and Cu(111) Surface

position	atop	fcc	hcp	bridge
snap bond energy (kcal/mol)	45.2	45.3	46.5	46.9
relative energy (kcal/mol) <sup>a</sup>	1.7	1.6	0.4	0
perpendicular separation (Å) <sup>b</sup>	2.00	1.81	1.84	1.81
Cu–C distance (Å) <sup>c</sup>	1.98	2.13, 2.40, 2.71	2.11, 2.51, 2.66	2.16, 2.19

<sup>a</sup> Lowest energy is defined as 0.

<sup>b</sup> Z-coordinates of the atoms on the Cu(111) surface are averaged.

<sup>c</sup> Nearest neighbor atoms.

**Table 2.** Energetics and Geometry between –CCH Anchor and Cu(111) Surface

position	atop	fcc	hcp	bridge
snap bond energy (kcal/mol)	88.8	103.5	102.7	99.3
relative energy (kcal/mol) <sup>a</sup>	14.7	0	0.7	4.2
perpendicular separation (Å) <sup>b</sup>	1.83	1.37	1.40	1.56
Cu-C bond distance (Å) <sup>c</sup>	2.11	2.00, 2.08, 2.13	2.06, 2.10, 2.19	2.03, 2.07

<sup>a</sup> Lowest energy is defined as 0.

<sup>b</sup> Z-coordinates of the atoms on the Cu(111) surface are averaged.

<sup>c</sup> Nearest neighbor atoms.

**Table 3.** Energetics and Geometry between  $-\text{CONH}_2$ ,  $-\text{CONH}$ , and  $-\text{CON}$  Anchors and Cu(111) Surface

initial structure <sup>a</sup>	(CH <sub>3</sub> )CONH <sub>2</sub>	(CH <sub>3</sub> )CONH, H	(CH <sub>3</sub> )CON, 2H
final atom position	O, on	O, on; N, bridge	N, fcc
snap bond energy (kcal/mol)	113.0	122.2	95.9
relative energy (kcal/mol) <sup>b</sup>	9.5	0	26.4
perpendicular separation (Å) <sup>c</sup>	1.81	1.58	0.96
Cu-O bond distance (Å) <sup>d</sup>	2.17	2.10	–
Cu-N bond distance (Å) <sup>d</sup>	–	2.09, 2.17	2.00, 2.01, 2.09

<sup>a</sup> To compare the energies per unit cell, hydrogen atoms are bonded on the Cu(111) surface for (CH<sub>3</sub>)CONH and (CH<sub>3</sub>)CON.

<sup>b</sup> Lowest energy is defined as 0.

<sup>c</sup> Z-coordinates of the atoms on the Cu(111) surface are averaged.

<sup>d</sup> Nearest neighbor atoms.

**Table 4.** Energetics and Geometry between  $-\text{COOH}_2$  and  $-\text{COOH}$  Anchors and Cu(111)

Surface

initial structure <sup>a</sup>	(CH <sub>3</sub> )COOH	(CH <sub>3</sub> )COO, H
final atom position	–	O(1), on; O(2), bridge
snap bond energy (kcal/mol)	13.0	70.3
relative energy (kcal/mol) <sup>b</sup>	5.4	0
perpendicular separation (Å) <sup>c</sup>	2.26	1.75
Cu-O bond distance (Å) <sup>d</sup>	–	Cu–O(1), 2.08; Cu–O(2), 2.19, 2.39

<sup>a</sup> One hydrogen atom is added for (CH<sub>3</sub>)COO to compare the energetics per unit cell.

<sup>b</sup> Lowest energy is defined as 0.

<sup>c</sup> Z-coordinates of the atoms on the Cu(111) surface are averaged.

<sup>d</sup> Nearest neighbor atoms.

**Table 5.** Difference in Snap and Adiabatic Bond Energetic of Two Acetylene (HCC–) Anchors at Resonance (a, b, c) and Nonresonance (d, e, f) Positions<sup>a</sup>

	site	dist.(Å) <sup>b</sup>	total energy (kcal/mol)			energy by adding second HCC– (kcal/mol)		
			snap <sup>c</sup>	BE <sup>d</sup>	strain <sup>e</sup>	snap <sup>c</sup>	BE <sup>d</sup>	strain <sup>e</sup>
first HCC–	–	–	79.7	33.7	46.0	–	–	–
second HCC–	a2	5.1	142.6	80.4	61.4	62.9	46.7	15.5
	a3	5.1	147.3	83.9	62.7	67.6	50.2	16.7
	b4	3.7	143.5	81.3	61.4	63.8	47.6	15.4
	c	5.6	138.2	75.9	61.7	58.5	42.2	15.7
	d4	4.2	126.4	63.0	62.7	46.7	29.3	16.8
	d5	4.2	128.3	62.9	64.8	48.6	29.2	18.8
	e2	4.9	128.2	63.5	64.2	48.5	29.6	18.3
	f	6.5	128.3	63.0	64.8	48.6	29.2	18.8

<sup>a</sup> a3 site provides the most stable structure for the second anchor.

<sup>b</sup> Distance between two anchors.

<sup>c</sup> Snap is bond energy, not allowing the fragments to relax.

<sup>d</sup> BE is adiabatic bond energy.

<sup>e</sup> Strain is the strain energy in graphene caused by bonding HCC–.

**Table 6.** Energetics and Geometry between Anchors and Graphene

anchor	C <sub>6</sub> H <sub>5</sub> -	CCH-	CONH <sub>2</sub> -	COOH-
snap bond energy (kcal/mol) <sup>a</sup>	58.9	82.6	42.0	50.5
graphene strain energy (kcal/mol) <sup>b</sup>	13.9	14.1	11.1	13.9
perpendicular separation (Å) <sup>c</sup>	1.58	1.48	1.63	1.59

<sup>a</sup> Snap bond energy was calculated for each anchor (H atom is excluded).

<sup>b</sup> Deformation energy in graphene caused by bonding an anchor (H atom is excluded).

<sup>c</sup> Perpendicular separation between the carbon atom of an anchor and the bonded carbon atom on graphene. Z-coordinates of the atoms on the Cu(111) surface are averaged.

**Table 7.** Energetics and Geometry of Cu(111) Surface–Anchor–Graphene

anchor	–C <sub>6</sub> H <sub>4</sub> –	–CC–	–CONH–	–COO–	no anchor <sup>a</sup>
snap bond energy (kcal/mol)	106.1	168.9	117.8	123.9	4.8
anchor–Cu(111) surface separation (Å) <sup>b</sup>	1.97	1.33	1.88	2.03	–
anchor–graphene separation (Å) <sup>c</sup>	1.58	1.48	1.62	1.64	–
Cu(111)–graphene separation (Å) <sup>d</sup>	7.03	4.62	4.65	4.73	3.30

<sup>a</sup> Reference 10.

<sup>b</sup> The shortest perpendicular separation between the C or N or O atom of an anchor and the Cu(111) surface. Z-coordinates of the atoms on the Cu(111) surface are averaged.

<sup>c</sup> Perpendicular separation between the carbon atom of an anchor and the bonded carbon atom on graphene.

<sup>d</sup> Z-coordinates of atoms on each surface are averaged.

**Table 8.** Contact Resistance of Cu(111)–Anchor–Graphene Interface

anchor	–C <sub>6</sub> H <sub>4</sub> –	–CC–	–CONH–	–COO–	no anchor <sup>a</sup>
contact resistance (kΩ) <sup>b</sup>	10080	127.5	63.7	42.6	11716
inverse ratio	1.1	92	184	275	1.0

<sup>a</sup> Ref 10.

<sup>b</sup> Per unit area of 0.735 nm<sup>2</sup> (0.98 × 0.85 nm<sup>2</sup>).

## References

- (1) Javey, A.; Guo, J.; Wang, Q.; Lundstrom, M.; Dai, H. *Nature* **2003**, *424*, 654.
- (2) Mann, D.; Javey, A.; Kong, J.; Wang, Q.; Dai, H. *Nano Lett.* **2003**, *3*, 1541.
- (3) Frank, S.; Poncharal, P.; Wang, Z. L.; de Heer, W. A. *Science* **1998**, *280*, 1744.
- (4) Oostinga, J. B.; Heersche, H. B.; Liu, X.; Morpurgo, A. F.; Vandersypen, L. M. K. *Nature Mater.* **2008**, *7*, 151.
- (5) Geim, A. K.; Novoselov, K. S. *Nature Mater.* **2007**, *6*, 183.
- (6) Ryan, J. G.; Geffen, R. M.; Poulin, N. R.; Paraszczak, J. R. *IBM J. Res. Dev.* **1995**, *39*, 371.
- (7) Licata, T. J.; Colgan, E. G.; Harper, J. M. E.; Luce, S. E. *IBM J. Res. Dev.* **1995**, *39*, 419.
- (8) McNally, P. J.; Kanatharana, J.; Toh, B. H. W.; McNeill, D. W.; Danilewsky, A. N.; Tuomi, T.; Knuuttila, L.; Riikonen, J.; Toivonen, J.; Simon, R. *J. Appl. Phys.* **2004**, *96*, 7596.
- (9) Talanov, V. V.; Scherz, A.; Schwartz, A. R. *Appl. Phys. Lett.* **2006**, *88*, 262901.
- (10) Matsuda, Y.; Deng, W.-Q.; Goddard, W. A., III. *J. Phys. Chem. C.* **2007**, *111*, 11113.
- (11) Wang, Y.; Iqbal, Z.; Mitra, S. *J. Am. Chem. Soc.* **2006**, *128*, 95.

- (12) Narain, R.; Housni, A.; Lane, L. *J. Polym. Sci., Part A: Polym. Chem.* **2006**, *44*, 6558.
- (13) Mickelson, E. T.; Chiang, I. W.; Zimmerman, J. L.; Boul, P. J.; Lozano, J.; Liu, J.; Smalley, R. E.; Hauge, R. H.; Margrave, J. L. *J. Phys. Chem. B.* **1999**, *102*, 4318.
- (14) Choi, K. H.; Bourgoïn, J. P.; Auvray, S.; Esteve, D.; Duesberg, G. S.; Roth, S.; Burghard, M. *Surf. Sci.* **2000**, *462*, 195.
- (15) Klinke, C.; Hannon, J. B.; Afzali, A.; Avouris, P. *Nano Lett.* **2006**, *6*, 906.
- (16) Li, S.; Yan, Y.; Liu, N.; Chan-Park, M. B.; Zhang, Q. *Small* **2007**, *4*, 616.
- (17) Song, C.; Xia, Y.; Zhao, M.; Liu, X.; Li, F.; Huang, B. *Chem. Phys. Lett.* **2005**, *415*, 183.
- (18) Zhang, Y.; Suc, C.; Liu, Z.; Li, J. *J. Phys. Chem. B.* **2006**, *110*, 22462.
- (19) Veloso, M. V.; Filho, A. G. S.; Filho, J. M.; Fagan, S. B.; Mota, R. *Chem. Phys. Lett.* **2006**, *430*, 71.
- (20) Deng, W.-Q.; Matsuda, Y.; Goddard, W. A., III. *J. Am. Chem. Soc.* **2007**, *129*, 9834.
- (21) McEuen, P. L.; Fuhrer, M. S.; Park, H. *IEEE Trans. on Nanotechnol.* **2002**, *1*, 78.
- (22) Bahr, J. L.; Yang, J.; Kosynkn, D. V.; Bronikowski, M. J.; Smalley, R. E.; Tour, J. M. *J. Am. Chem. Soc.* **2001**, *123*, 6536.
- (23) Dyke C. A.; Tour, J. M. *Nano Lett.* **2003**, *3*, 1215.

- (24) Liang, F.; Sadama, A. K.; Peera, A.; Chattopadnyay, J.; Gu, Z.; Hauge, R. H.; Billups, W. E. *Nano Lett.* **2004**, *4*, 1257.
- (25) Ramanathan, T.; Fisher, F. T.; Ruoff, R. S.; Brinson, L. C. *Chem. Mater.* **2005**, *17*, 1290.
- (26) Schultz, P. A. *SEQQUEST code*; Sandia National Labs: Albuquerque, NM, **2005**.  
<http://dft.sandia.gov/Quest/>.
- (27) Mattsson, A. E.; Schultz, P. A.; Desjarlais, M. P.; Mattsson, T. R.; Leung, K. *Model. Simul. Mater. Sci. Eng.* **2005**, *13*, R1-R31.
- (28) Perdew, J. P.; Burke, K.; Ernzerhof, M. *Phys. Rev. Lett.* **1996**, *77*, 3865.
- (29) Kim, Y. -H.; Tahir-Kheli, J.; Schultz, P. A.; Goddard, W. A., III. *Phys. Rev. B* **2006**, *73*, 235419.
- (30) *CRC Handbook of Chemistry and Physics*, 87th ed.; Lide, D. R., Ed.; CRC Press: Boca Raton, FL, **2006**.
- (31) Liu, J.; Casavant, M. J.; Cox, M.; Walters, D. A.; Boul, P.; Lu, W.; Rimberg, A. J.; Smith, K. A.; Colbert, D. T.; Smalley, R. E. *Chem. Phys. Lett.* **1999**, *303*, 125.

## Chapter 3

# Contact Resistance of “End-contacted” Metal–Graphene and Metal–Nanotube Interfaces<sup>\*</sup>

### Abstract.

In this paper, we predict the current-voltage ( $I$ – $V$ ) characteristics and contact resistance of “end-contacted” metal electrode–graphene or metal electrode–carbon nanotube (CNT) interfaces for five metals, Ti, Pd, Pt, Cu and Au, based on first-principles quantum mechanical density functional and matrix Green’s function methods. We find the contact resistance of “end-contacted” (or end-on) is 107 k $\Omega$  for Ti, 142 k $\Omega$  for Pd, 149 k $\Omega$  for Pt, 253 k $\Omega$  for Cu, and 187 k $\Omega$  for Au per surface carbon atom at the interface, corresponding to the improvement best in Au (1/6751) followed by Cu (1/2488) > Pt (1/233) > Pd (1/60) > Ti (1/8.8) compared to the “side-contacted” configurations. This can be compared with contact resistance for “side-contacted” metal–graphene or metal–CNT interfaces of 8.6 M $\Omega$  for Pd and 630 M $\Omega$  for Cu, for example. (There is now and experimental validation for the predicted Pt–CNT contact resistance, indicating an accuracy of ~10 %.) This suggests premium for developing technology to achieve “end-contacted” configurations.

---

\* Matsuda, Y.; Deng, W.-Q.; Goddard, W. A. III. “Quantum Mechanics Predictions for Contact Resistance of “End-contacted” Metal–Graphene and Metal–Nanotube Interfaces”. Submitted.

## 1. Introduction

Carbon nanotubes (CNTs)<sup>1</sup> and graphenes (monolayer<sup>2,3</sup>, bilayer<sup>4,5</sup>, and nanoribbons<sup>6,7</sup>) are most promising materials for applications in nanoelectronics due to their small size and superior electrical properties. In particular, metallic CNTs and graphenes are potential candidate for the on-chip interconnect materials in future integrated circuits<sup>8-10</sup> because they have potential advantages for achieving highest possible density integration in combination with high current density<sup>11</sup>, ballistic conductance<sup>12-14</sup>, and high thermal conductivity<sup>15</sup>. Indeed, significant progress has been made in fabrication techniques for CNT interconnects on Si wafers. For example, CNTs for via (vertical) interconnects were successfully grown directly on Si wafers using Co<sup>16</sup>, Fe<sup>17</sup>, or Ni<sup>18</sup> catalysts. In addition, CNT horizontal interconnects have been integrated with silicon complementary metal–oxide–semiconductor (CMOS) transistors on the same chip by applying an electric field to the CNTs dispersed in ethanol, enabling above 1 GHz operation.<sup>19</sup> Furthermore, single layer graphene has been demonstrated to exhibit high electron mobility ( $\sim 15,000 \text{ cm}^2 / \text{Vs}$ ) and thermal conductivity ( $3100 - 5300 \text{ } \Omega / \text{mK}$ ).<sup>2,20,21</sup> They may have advantages over CNTs for developing strategies of selective growth on metals or semiconductors, for example, epitaxial growth on SiC(0001)<sup>4,6,22</sup> and Ru(0001)<sup>23</sup>.

A critical property for such nanoelectronic devices is the contact resistance at the metal–CNT or metal–graphene interfaces. We previously reported contact resistances for “side-contacted” metal electrode (Figure 1b) to CNT or graphene.<sup>24</sup> Here we used ab-initio quantum mechanical (QM) studies to show that Ti leads to the lowest contact resistance of  $24.2 \text{ k}\Omega/\text{nm}^2$  followed by Pd ( $221 \text{ k}\Omega/\text{nm}^2$ ), Pt ( $881 \text{ k}\Omega/\text{nm}^2$ ), Cu ( $16.3 \text{ M}\Omega/\text{nm}^2$ ), and Au ( $32.6 \text{ M}\Omega/\text{nm}^2$ ) for “side-contacted” metal electrode (Figure 1b) to CNT or

graphene.<sup>25</sup> Although Cu–graphene interface has a contact resistance 672 times higher for Ti, we found that incorporation of bifunctional groups (anchors) can reduce the Cu–graphene contact resistance by a factor of 275, making Cu better than Pd by 3.7 times.<sup>25</sup>

In this paper, we use QM to determine the electrical properties (e.g., contact resistance) for “end-contacted” (or vertical) metal–graphene and metal–CNT electrodes (Figure 1a). We find that this “end-contacted” metal electrode improves the contact resistance by up to a factor of 6751, while simultaneously increasing mechanical stabilities dramatically.

## 2. Methods

### 2.1. Modeling Details.

To model the “end-contacted” metal–graphene or metal–CNT configurations as shown in Figure 1a, we have chosen  $2 \times 4$  graphene unit cell (16 carbon atoms) of the graphene sheet (fixed in  $x$  direction at 0.846 nm) as shown in Figure 2. We placed the metal atoms at the arm-chair edge of graphene (4 carbon atoms at the interface) one by one, followed by relaxing the geometry each time to represent the ideal metal–graphene interface. The six metal atoms, which are vertical to the graphene surface, at the interface (shown with red atoms in Figure 2) show the periodicity similar to the deposited metals on the graphene sheet in our previous work<sup>24</sup> and determines the  $y$  periodicity (0.489 nm). For each system the metal layers were added one by one and optimized for the contact to graphene. The additional three layers of metal (six atoms per layer per cell) are constructed as ABC stacking (face-centered cubic (fcc)) for Pd, Pt, Cu and Au and

ABAB stacking (hexagonal close-packed (hcp)) for Ti for the bulk structures. For Ti, the hcp packing was found to be more stable than the fcc by 2.4 kcal / mol per unit cell.<sup>24</sup>

The models are to focus on the local interfacial structures and contact resistance ( $R_{\text{cont}}$ ) properties in this paper. The total resistance ( $R_{\text{T}}$ ), is expressed as  $R_{\text{T}} = R_{\text{cont}} + R_{\text{C}} +$  scattering, where  $R_{\text{C}}$  represents the resistance of CNT or graphene.<sup>26</sup> The scattering term can be ignored since the distance is much smaller than the mean free path of an electron. In addition, we found that effect of the larger attractive interaction due to the hybridization (incursion of the s hybrid character in the  $p\pi$  orbital) caused by the CNT curvature is small, leading slight decrease in the separation at metal–CNT interface by 0.04 – 0.08 Å (1.9 – 2.8 %) for the CNTs of diameters 0.95 and 1.0 nm. Considering all of these issues, we believe that the metal–graphene models represent for metal–CNT configurations with a diameter larger than 1.0 nm for all geometric considerations.

## 2.2. Computational Details.

We used SEQUEST<sup>27</sup>, a fully self-consistent Gaussian-based linear combination of atomic orbitals (LCAO) density functional theory (DFT) method with double- $\zeta$  plus polarization (DZP) basis sets.<sup>28</sup> All calculations were based on the Perdew–Burke–Ernzerhof (PBE) flavor of generalized gradient approximation (GGA) with PBE pseudo atomic potentials and within 2D periodic boundary conditions.<sup>29</sup> The  $k$ -point sampling of  $4 \times 4$  in the Brillouin Zone and the real space grid interval of  $46 \times 26$  in the  $x$ – $y$  plane, for a grid spacing of 0.35 bohr, were carefully determined by energetic convergence.

To obtain  $I$ – $V$  characteristics of each model, the density of states (DOS) was obtained from DFT quantum mechanics, while the transmission coefficient was obtained using matrix Green’s function theory with DFT (which we have used successfully to compute transport properties of molecular electronic devices).<sup>30</sup> The transmission function was then used in the Landauer–Buttiker formula to calculate the  $I$ – $V$  characteristics. The zero-bias transmission  $T(E, V = 0)$  approximation was applied to the computation of the current  $I$  at a finite bias voltage ( $V$ ) which was defined as the difference between the source and the drain voltage. The finite- $V$  transmission  $T(E, V)$  should be close to  $T(E)$  at a low bias voltage of  $-0.1$  to  $0.1$  V, which would be the operating voltage range for devices studied in this paper. The large- $V$  region ( $V > 0.5$  V)  $I$ – $V$  curves should be taken as qualitative. We then calculated the current as a function of bias voltage and the contact resistance for the five deposited metals.

### 3. Results

#### 3.1. Geometrical Properties.

Figure 2 shows the top and side views of the “end-contacted” metal–graphene interface of the optimum geometries. We see that metal–metal interlayer distances are generally within 2 % of the bulk values<sup>31</sup> except for the Ti and Pt top layers which are contracted by 5 % and 3 %, respectively, and the Au system all layers are increased  $\sim 11$  % (Table 1).

The interaction energy of each metal–graphene structure was calculated by comparing the equilibrium states with the each component by separating the electrode (all metal

atoms) infinitely far from graphene surface (snap bond energy) (Figure 3a). These quantities were normalized by the surface carbon atoms at the interface (there are four carbon atoms). We see that the bond energies range from 77.4 kcal/mol (Ti) to 29.6 kcal/mol (Au) and decreases as  $Ti > Pd \approx Pt > Cu > Au$ . As expected, “end-contacted” electrodes lead to greatly increasing interaction energy over that of “side-contacted” electrodes (Figure 3b). The best improvement is for Cu with 323 times followed by Pt (259 times), Au (247 times), Pd (199 times), and the smallest improvement is for Ti with 12.9 times.

### 3.2. $I$ – $V$ characteristics.

The structures for the  $I$ – $V$  calculations (Figure 4a) were constructed from the optimized geometries (Figure 2) by reversing the electrodes and two surface carbon layers of the graphene to calculate directly the contact resistance ( $R_{\text{cont}}$ ). These  $I$ – $V$  structures contain the two contacts (source and drain) bridged by the channel (graphene). Since the surface layer of metal electrodes is strongly bonded to the graphene edge, this layer is included as part of the channel while other three periodic layers of each electrode is considered to be the contact (used iteratively to form the surface Green’s function).

Notably, only the d-orbitals of surface metals and the p-orbitals of surface carbon atoms contribute significantly to the DOS (Figure S1). The projected density of states (PDOS) per unit cell of the p-orbitals (PDOS( $C_p$ )) of surface carbon atoms of graphene at the interface are shown in Figure 4b. These PDOS( $C_p$ ) differ from each other with little systematic similarities in various peaks although reflecting individual characteristics of

the metal electrodes. Even so, the PDOS( $C_p$ ) are large and similar at the Fermi energy ranging from  $1.8 \text{ eV}^{-1}$  (Ti) to  $2.2 \text{ eV}^{-1}$  (Au), indicating a good conduction channel. For the Ti, Pd, and Pt structures, the PDOS( $C_p$ ) of surface carbon atoms near the Fermi energy are mostly carbon  $p\pi$ -orbitals ( $py$ -orbitals in Figure S1), but for the Cu and Au structures, both  $p\pi$ - and  $p\sigma$ -orbitals ( $py$ - and  $pz$ -orbitals, respectively, in Figure S1) contribute equally.

The PDOS for the d-orbitals of the surface (first-layer) metal atoms (PDOS( $M_d$ )) are shown in Figure 4c. Here we see that the PDOS( $M_d$ ) at the Fermi energy ranging from  $15 \text{ eV}^{-1}$  (Ti) down to  $1.5 \text{ eV}^{-1}$  (Au) with a sequence of  $\text{Ti} > \text{Pt} > \text{Pd} > \text{Cu} > \text{Au}$ . For Au, the PDOS( $C_p$ ) is larger than the PDOS( $M_d$ ).

The transmission function,  $T(E)$ , (Figure 4d) near the Fermi energy mirrors the PDOS behaviors except for the Cu system, which shows lower  $T(E)$  than the Au system at the Fermi energy ( $-0.5$  to  $+0.25 \text{ eV}$ ). The calculated  $I$ - $V$  curve (Figure 5a) and total resistance (Figure 5b) correlate directly with the  $T(E)$ , which correlates with the cohesive coupling between the metal d-orbitals and graphene p-orbitals, as discussed above.

We find that Ti has a linear  $I$ - $V$  curve from  $-1$  to  $+1 \text{ V}$  indicating an Ohmic contact, while Pd and Pt are linear from  $-0.5$  to  $+0.5 \text{ V}$ . Using the slope at  $0 \text{ V}$  (at the Fermi energy), we calculate conductance ranging from  $0.97 G_0$  for Ti down to  $0.40 G_0$  for Cu.  $2 G_0$  ( $G_0 \equiv 2q^2/h = 77.5 \text{ } \mu\text{S} = (12.9 \text{ k}\Omega)^{-1}$ ) is the expected conductance quantum for a single-walled carbon nanotube (SWNT) when assuming perfect contacts. From the conductance we obtain contact resistance ( $R_{\text{cont}}$ ) per unit cell of the “end-contact” structures of  $53 \text{ k}\Omega$  for Ti,  $71 \text{ k}\Omega$  for Pd,  $74 \text{ k}\Omega$  for Pt,  $127 \text{ k}\Omega$  for Cu, and  $93 \text{ k}\Omega$  for Au

after averaging the bias voltage from  $-0.1$  to  $+0.1$  V (Table 2). All the contact resistances are also shown per surface carbon atom at the interface allowing us to estimate to the contact resistance for “end-contacted” metal–CNT interfaces as it will be discussed later. As expected, the  $R_{\text{cont}}$  of “end-contacted” is enormously improved over that of “side-contacted” electrodes with improvements ranging from best for Au (1/6751) followed by Cu (1/2488) > Pt (1/233) > Pd (1/60) > Ti (1/8.8).

## 4. Discussion

### 4.1. Nature of the Metal–Carbon Contact.

With “side-contacted” metal–graphene interfaces, only the carbon  $p\pi$  orbitals of carbon atoms contribute to the cohesion to the surface metals (d orbitals). However for “end-contacted” metal–graphene interfaces, carbon  $p\pi$  orbitals as well as  $p\sigma$  orbitals play important roles in cohesion because the surface carbon has  $p\sigma$  electrons that are either unpaired (zigzag) or involved in a weak in-plane  $\pi$  bond (armchair). Thus, these  $p\sigma$  electrons could play substantial roles in cohesion and hence transmission. In fact, Figure S1 shows that only  $p\pi$  orbital is important for Ti, Pd, and Pt while both  $p\pi$  and  $p\sigma$  orbitals are significant for Au and Cu electrodes. Additionally, the PDOS( $C_p$ ) of Au is larger than the PDOS( $M_d$ ) near the Fermi energy, indicating that bond properties of the “end-contacted” Au–graphene is dominated by p orbitals of the surface carbon atoms.

## 4.2. Electrical Properties at the Interface.

Our results indicate that among the five metals considered here, the contact resistance per surface carbon atom is smallest for Ti (107 k $\Omega$ ) and small for Pd (142 k $\Omega$ ) and Pt (149 k $\Omega$ ) and large for Au (187 k $\Omega$ ) and Cu (253 k $\Omega$ ).

Recently, four-terminal experiments on Pt electrode (5 nm depositing on top of CNT and protected with 60 nm Au) “side-contacted” to metallic SWNT (1.0 – 1.5 nm) found a contact resistance of  $R_{\text{side-cont}} \approx 5 \text{ k}\Omega$  with the length of the contacts of  $\sim 1 \mu\text{m}$ .<sup>32</sup> To analyze these experimental results to obtain the specific contact resistance, we assume that the SWNT (10,10) (diameter = 1.37 nm) which is most commonly synthesized CNTs. Given the contact length of 1  $\mu\text{m}$ , there are 16,192 carbon atoms in SWNT (10,10). Assuming that 50 % of the carbon atoms around the circumference of the SWNT are in contact with electrodes, we estimate the contact resistance per carbon atom is  $R_{C_{\text{side-cont}}} = R_{\text{side-cont}} \times N_{\text{side-cont}} = 5,000 \times 8,096 = 40.5 \text{ M}\Omega$ , where  $N_{\text{side-cont}}$  is the number of carbon atoms in contact with electrodes. This can be compared with our previous calculations for Pt case which has  $R_{C_{\text{side-cont}}} = 34.7 \text{ M}\Omega$  per carbon atom (Table 2).<sup>24</sup> Given all uncertainties, this is the good agreement.

The contact resistance results calculated for “end-contacted” metal–graphene interface can be used straightforwardly to estimate the contact resistance for “end-contacted” metal–CNT interface. For example, the armchair SWNT (10,10) has 40 carbon atoms, which is the number of atoms at the cross section, are at the metal–CNT interfaces. Thus, since the graphene results for Pt electrodes give contact resistance per carbon atom ( $R_{C_{\text{end-cont}}}$ ) of 148.5 k $\Omega$ , we estimate the contact resistance of the “end-contacted”

Pt–SWNT (10,10) interface would be  $R_{\text{end-cont}} = 3.7 \text{ k}\Omega$ , which indicates that “end-contacted” Pt electrodes may achieve the same contact resistance with “side-contacted” Pt electrodes (approximately  $5 \text{ k}\Omega$ ) with no contacts length. Moreover, for a double-walled carbon nanotube (DWNT), for example (10,10) and (6,6), the number of the carbon atoms “end-contacted” with electrodes is 64, leading to  $R_{\text{end-cont}} = 2.3 \text{ k}\Omega$ . Thus the “end-contacted” electrodes are utilized more effectively for multiwalled CNTs and CNT bundles.

Despite the advantages of “end-contacted” configurations, there remain significant experimental difficulties in constructing them. Experiments to suspend and disperse CNTs in various solutions (e.g., water or organic solvents)<sup>33–35</sup> have been reported. For via interconnects, chemical mechanical polishing has been successful in achieving “end-contacted” electrode to some extent.<sup>29</sup> Thus by combining and utilizing such techniques, development of similar approaches for horizontal “end-contacted” configurations may be possible.

For an alternative strategy, we consider the geometry where the ends of the CNT covered with electrode (Figure 6). In this case, the total contact resistance can be written as  $R_{\text{cont}} = (1/R_{\text{end-cont}} + 1/R_{\text{side-cont}})^{-1}$ , where  $R_{\text{end-cont}} = Rc_{\text{end-cont}} / N_{\text{end-cont}}$  is from the “end-contacted” interfaces and  $R_{\text{side-cont}} = Rc_{\text{side-cont}} / N_{\text{side-cont}}$  is from the “side-contacted” interfaces. Thus for the case of a (10,10) SWNT,  $N_{\text{end-cont}} = 40$  while  $N_{\text{side-cont}} = 162$  for 10 nm. Since  $Rc_{\text{end-cont}} = 142.4 \text{ k}\Omega$ ,  $Rc_{\text{side-cont}} = 8,566 \text{ k}\Omega$  for Pd electrodes, we obtain the total contact resistance  $R_{\text{cont}} = 3.3 \text{ k}\Omega$ . This illustrates the advantage of such “end-contacted” configurations. We assumed the “side-contacted” length to be 10 nm since

probably by the time it is necessary to use CNTs for via and horizontal interconnects components it would be necessary to reduce the contact area to 20 nm or less.

## 5. Conclusion

It is very difficult to extract reproducible results for the contact resistance data of metal–graphene or metal–CNT interfaces due to the small size and variations in device geometries. For this reason, it is valuable to carry out first principles QM calculations since they provide consistent accuracy for various combinations of metals and carbon structures. This paper illustrates how to use first-principle QM to predict such complex phenomena as contact resistance in metal–graphene and metal–CNT assemblies enabling *in silico* analysis and design prior to experiments.

We analyzed the recently reported experimental contact resistance of Pt–CNT in comparison to our previous “side-contacted” calculations<sup>24</sup>. We find that they agree within ~ 10 %, which helps validate the accuracy of both the theory and these very difficult experiments.

Based on QM studies of the metal–graphene interface, we conclude that there are substantial advantages in reduced contact resistances for configurations that include “end-contacted” metal electrodes. Because of the difficulty in making “end-contacted” electrodes as in Figure 1a, we suggest Figure 6 as practical configurations which also dramatically reduce the total contact resistance.

Although the application here is towards high-performance on-chip interconnect applications, the results should be applicable to other CNT or graphene based

nanoelectronic and optoelectronic devices such as the field-effect transistors and light emitting diodes.

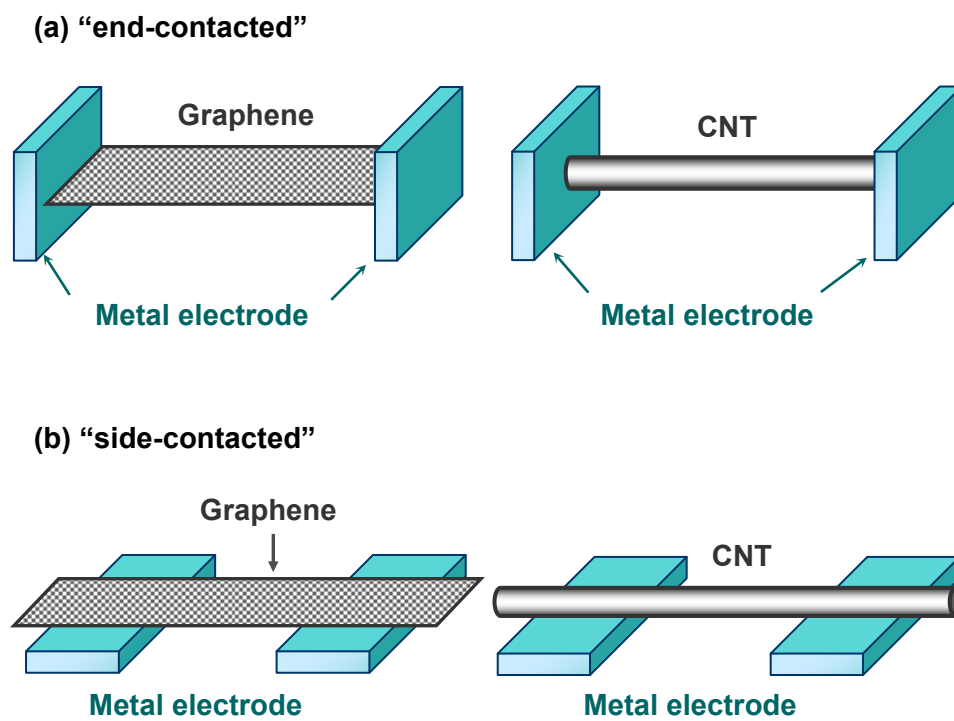


**Figure 1.** (a) Interaction energy of the metal–graphene “end-contacted” interface shown in Figure 1a. (b) “side-contacted” interface shown in Figure 1b (Ref. 24).

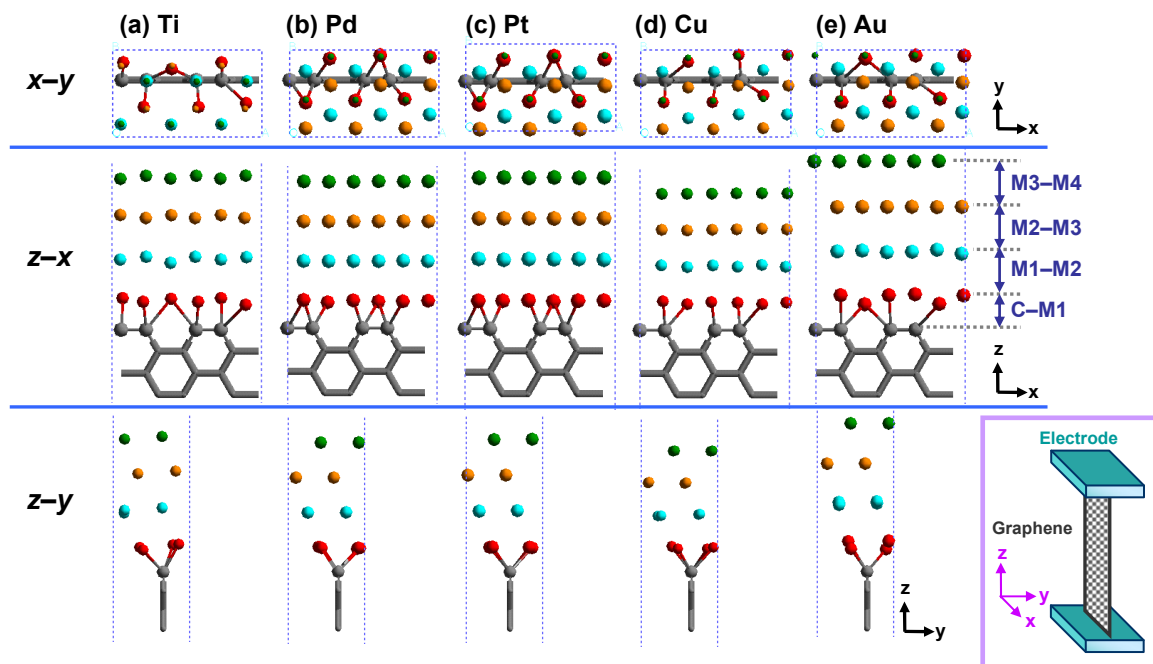


**Figure 2.** Optimized geometries for graphene-metal interface. Top section shows the top view ( $x$ - $y$  plane). Middle section shows the side view ( $z$ - $x$  plane). Bottom section shows the side view ( $z$ - $y$  plane). (a) Ti, (b) Pd, (c) Pt, (d) Cu, and (e) Au. The unit cell is  $0.846 \text{ nm} \times 0.489 \text{ nm}$  (periodic in  $x$ - $y$  directions) with 24 metal atoms (6 atoms  $\times$  4 layers) and 16 carbon atoms (4 atoms  $\times$  4 layers). The Ti is found to have the hcp packing while the others are the fcc. The layer-layer distances are given in Table 1 (C, graphene layer at the interface; M1, metal layer at the interface (first layer); M2, second metal layer; M3, third metal layer; M4, fourth metal layer).

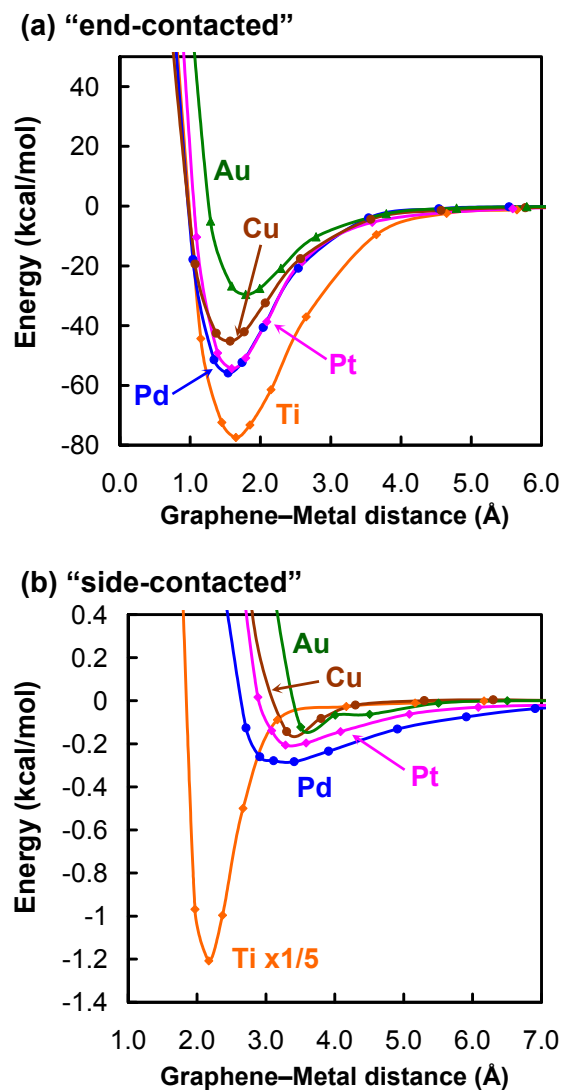


**Figure 3.** (a) Interaction energy (per surface C atom) of the metal–graphene for “end-contacted” interface shown in Figure 1a, and (b) for “side-contacted” interface shown in Figure 1b (Ref. 24). The Ti is scaled by 1:5 (orange, Ti; blue, Pd; pink, Pt; brown, Cu; green, Au). The energies are given in Table 1.

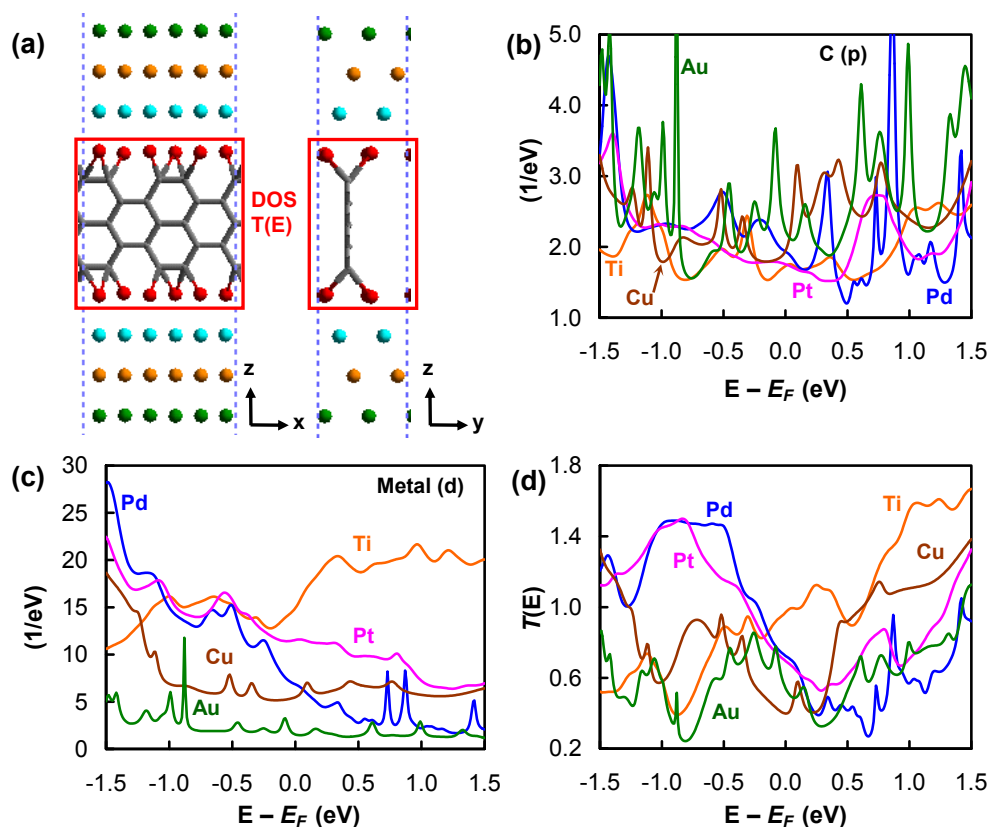


**Figure 4.** Current–Voltage ( $I$ – $V$ ) calculations. (a) Metal–graphene–metal structures used in  $I$ – $V$  calculations (Pd case shown). (b) Partial density of states (PDOS) for p orbital for carbon at the metal–graphene interface per unit cell. (c) PDOS summing over all five d-orbitals for metal at the metal-graphene interface per unit cell. (d) Transmission Coefficient ( $T(E)$ ) (orange, Ti; blue, Pd; pink, Pt; brown, Cu; green, Au). Separate lines of each metal for (b), (c), and (d) are shown in Supporting Information (Figure S2, S3, and S4).

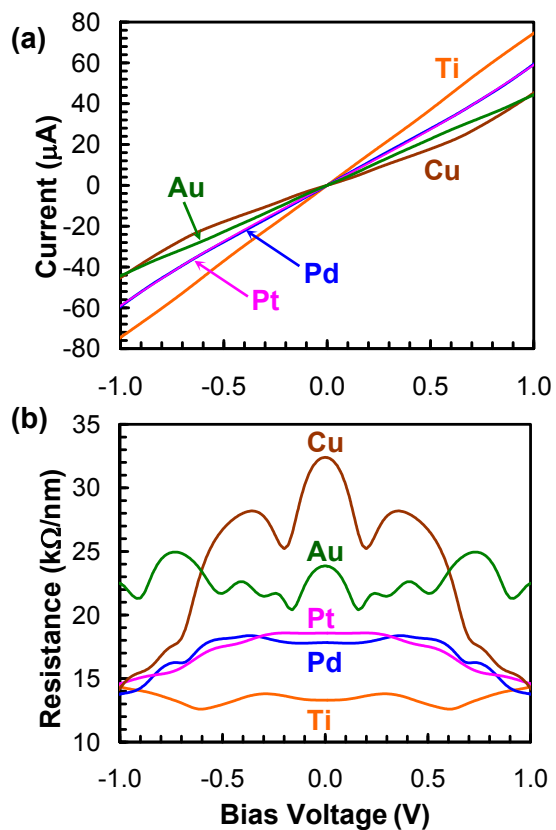


**Figure 5.** Current–Voltage ( $I$ – $V$ ) characteristics near the Fermi energy per unit cell. (a)  $I$ – $V$  curve and (b) contact resistance (orange, Ti; blue, Pd; pink, Pt; brown, Cu; green, Au).

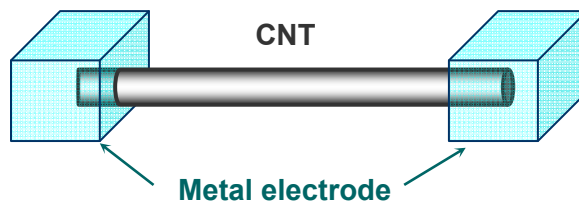


**Figure 6.** Proposed metal–CNT interface configuration.

**Table 1.** Layer–Layer perpendicular separations (Å) of the Metal–Graphene Structures after Optimization and Cohesive Energy (kcal/mol) of the Interface between Metal–Graphene

	Ti	Pd	Pt	Cu	Au
C–M1 perpendicular separation <sup>a</sup> (Å)	1.65	1.54	1.59	1.55	1.79
M1–M2 perpendicular separation <sup>a</sup> (Å)	2.36	2.27	2.34	2.08	2.63
M2–M3 perpendicular separation <sup>a</sup> (Å)	2.39	2.24	2.30	2.06	2.53
M3–M4 perpendicular separation <sup>a</sup> (Å)	2.22	2.26	2.30	2.04	2.59
bulk value (experimental) 300K <sup>b</sup> (Å)	2.34	2.25	2.26	2.08	2.36
metal–graphene cohesive energy <sup>c</sup> (kcal/mol)	77.4	55.9	54.4	45.2	29.6
metal–graphene cohesive energy of “side-contacted” structures <sup>d</sup> (kcal/mol)	6.0	0.28	0.21	0.14	0.12

<sup>a</sup> Z-coordinates of the atoms are averaged. C, graphene layer at the interface; M1, metal layer at the interface (first layer); M2, second metal layer; M3, third metal layer; M4, fourth metal layer. C and M1–M4 are shown in Figure 2.

<sup>b</sup> Ref. 38.

<sup>c</sup> For comparison, the contact resistance is averaged over the surface C atoms (4 atoms) at the interface.

<sup>d</sup> Ref. 24. For comparison, the contact resistance is averaged over the surface C atoms (8 atoms).

**Table 2.** Comparisons of Calculated Contact Resistance of “End-contacted” Metal–Graphene Interface with Those of “Side-contacted”

	Ti	Pd	Pt	Cu	Au
“end-contacted” per unit cell (k $\Omega$ )	13.3	17.8	18.6	31.7	23.3
“end-contacted” per C atom <sup>a</sup> (k $\Omega$ )	106.5	142.4	148.5	253.5	186.8
“side-contacted” per C atom <sup>b</sup> (k $\Omega$ )	938	8,566	34,689	630,352	1,261,002

<sup>a</sup> For comparison, the contact resistance is averaged over the surface C atoms (4 atoms  $\times$  2) at the interface.

<sup>b</sup> Ref. 24. For comparison, the contact resistance is averaged over the surface C atoms (8 atoms  $\times$  2).

## References

- (1) Saito, R.; Dresselhaus, G.; Dresselhaus, M. S. *Physical Properties of Carbon Nanotubes*, Imperial College Press, London, **1998**.
- (2) Novoselov, K. S.; Geim, A. K.; Morozov, S. V.; Jiang, D.; Zhang, Y.; Dubonos, S. V.; Grigorieva, I. V.; Firsov, A. A. *Science*, **2004**, *306*, 666.
- (3) Novoselov, K. S.; Geim, A. K.; Morozov, S. V.; Jiang, D.; Katsnelson, M. I.; Grigorieva, I. V.; Dubonos, S. V.; Firsov, A. *Nature*, **2005**, *438*, 197.
- (4) Ohta, T.; Bostwick, A.; Seyller, T.; Horn, K.; Rotenberg, E. *Science*, **2006**, *313*, 951.
- (5) Oostinga, J. B.; Heersche, H. B.; Liu, X.; Morpurgo, A. F.; Vandersypen, L. M. K. *Nature Mater.* **2008**, *7*, 151.
- (6) Berger, C.; Song, Z.; Li, X.; Wu, X.; Brown, N.; Naud, C.; Mayou, D.; Li, T.; Hass, J.; Marchenkov, A. N.; Conrad, E. H.; First, P. N.; de Heer, W. A. *Science*, **2006**, *312*, 1191.
- (7) Chen, Z.; Lin, Y.-M.; Rooks, M. J.; Avouris, P. *Physica E* **2007**, *40*, 228
- (8) Naeemi, A.; Sarvati, R.; Meindl, J. D. *IEDM Digest* **2004**, 699–702.
- (9) Avouris, P. *Acc. Chem. Res.* **2002**, *35*, 1026.
- (10) Avouris, P.; Chen, J. *Mater. Today* **2006**, *9*, 46.
- (11) Yao, Z.; Kane, C. L.; Dekker, C., *Phys. Rev. Lett.* **2000**, *84*, 2941.

- (12) Javey, A.; Guo, J.; Wang, Q.; Lundstrom, M.; Dai H. *Nature* **2003**, *424*, 654.
- (13) Mann, D.; Javey, A.; Kong, J.; Wang, Q.; Dai, H. *Nano Lett.* **2003**, *3*, 1541.
- (14) Frank, S.; Poncharal, P.; Wang, Z. L.; de Heer, W. A. *Science* **1998**, *280*, 1744.
- (15) Hone, J.; Yenilemez, E.; Tinbker, T. W.; Kim, W.; Dai, H. *Phys. Rev. Lett.* **2001**, *87*, 106801.
- (16) Awano. Y.; Sato, S.; Kondo, D.; Ohfuti, M.; Kawabata, A.; Nihei, M.; Yokoyama, N. *Phys. Stat. Sol. A.* **2006**, *203*, 3611.
- (17) Xu, T.; Wang, Z.; Miao, J.; Chen, X.; Tan, C. M. *Appl. Phys. Lett.* **2007**, *91*, 042108.
- (18) Coiffic, J. C.; Fayolle, M.; Maitrejean, S.; Foa Torres, L. E. F.; Le Poche, H. *Appl. Phys. Lett.* **2007**, *91*, 252107.
- (19) Close, G. F.; Yasuda, S.; Paul, B.; Fujita, S.; Phillip Wong, H.-S. *NanoLett.* **2008**, *8*, 706.
- (20) Balandin, A. A.; Ghosh, S.; Bao, W.; Calizo, I.; Teweldebrhan, D.; Miao, F.; Lau, C. N. *Nano Lett.* **2008**, *8*, 902.
- (21) Ghosh, S.; Calizo, I.; Teweldebrhan, D.; Pokatilov., E. P.; Nika, D. L.; Balandin, A. A.; Bao, W.; Miao, F.; Lau, C. N. *Appl. Phys. Lett.* **2008**, *92*, 151911.
- (22) Brar, V. W.; Zhang, Y.; Yayon, Y.; Ohta, T.; McChesney, J. L.; Bostwick, A.; Rotenberg., E.; Horn, K.; Crommie, M. F. *Appl. Phys. Lett.* **2007**, *91*, 122102.

- (23) Vazquez de Parga, A. L.; Calleja, F.; Borca, B.; Passeggi, M. C. G., Jr.; Hinarejos, J. J.; Guinea, F.; Miranda, R. *Phys. Rev. Lett.* **2008**, *100*, 056807.
- (24) Matsuda, Y.; Deng, W.-Q.; Goddard, W. A., III. *J. Phys. Chem. C.* **2007**, *111*, 11113.
- (25) Matsuda, Y.; Deng, W.-Q.; Goddard, W. A., III. *J. Phys. Chem. C.* **2008**, *112*, 11042.
- (26) McEuen, P. L.; Fuhrer, M. S.; Park, H. *IEEE Transaction on Nanotechnology.* **2002**, *1*, 78.
- (27) Schultz, P. A. *SEQQUEST code*; Sandia National Labs: Albuquerque, NM, 2005. <http://dft.sandia.gov/Quest/>.
- (28) Mattsson, A. E.; Schultz, P. A.; Desjarlais, M. P.; Mattsson, T. R.; Leung, K. *Modelling Simul. Mater. Sci. Eng.* **2005**, *13*, R1-R31.
- (29) Perdew, J. P.; Burke, K.; Ernzerhof, M. *Phys. Rev. Lett.* **1996**, *77*, 3865.
- (30) Kim, Y. -H.; Tahir-Kheli, J.; Schultz, P. A.; Goddard, W. A., III. *Phys. Rev. B* **2006**, *73*, 235419.
- (31) *CRC Handbook of Chemistry and Physics, 87th ed.*; Lide, D. R., Ed.; CRC Press: Boca Raton, FL, 2006.
- (32) Kanbara, T.; Takenobu, T.; Takahashi, T.; Iwasa, Y.; Tsukagori, K.; Aoyagi, Y.; Kataura, H. *Appl. Phys. Lett.* **2006**, *88*, 053118.

- (33) Chen, J.; Hamon, M. A.; Hu, H.; Chen, Y.; Rao, A. M.; Eklund, P. C.; Haddon, R. C. *Science*, **1998**, *282*, 95.
- (34) Niyogi, S.; Hu, H.; Hamon, M. A.; Bhowmik, P.; Zhao, B.; Rozenzhak, S. M.; Chen, J.; Itkis, M. E.; Meier, M. S.; Haddon, R. C. *J. Am. Chem. Soc.* **2001**, *123*, 733.  
Zhao, B.; Hu, H.; Niyogi, S.; Itkis, M. E.; Hamon, M. A.; Bhowmik, P.; Meier, M. S.; Haddon, R. C. *J. Am. Chem. Soc.* **2001**, *123*, 11673.
- (35) Strano, M. S.; Dyke, C. A.; Usrey, M. L.; Barone, P. W.; Allen, M. J.; Shan, H.; Kittrell, C.; Hauge, R. H.; Tour, J. M.; Smalley, R. E. *Science* **2003**, *301*, 1519.

**Acknowledgements.**

This work was supported partially by Intel Components Research (Kevin O'Brien, Florian Gstrein and James Blackwell) and by National Science Foundation (CCF-0524490 and CTS-0608889). The computer systems used in this research were provided by ARO-DURIP and ONR-DURIP). Additional support for the MSC was provided by ONR, ARO, DOE, NIH, Chevron, Boehringer-Ingelheim, Pfizer, Allozyne, Nissan, Dow-Corning, DuPont, and MARCO-FENA.

**Supporting Information Available.**

The detailed orbital contributions of the partial density of states (PDOS) of d-orbitals of the surface metal atoms and p-orbitals of the surface carbon atoms at the contact interface are shown in Figure S1. Also the PDOS (Figures 3b and c), and transmission coefficients,  $T(E)$ , (Figure 3d) are shown for each metal independently in Figure S2, S3, and S4, respectively. This material is available free of charge via the Internet at <http://pubs.acs.org>.

## Supporting Information

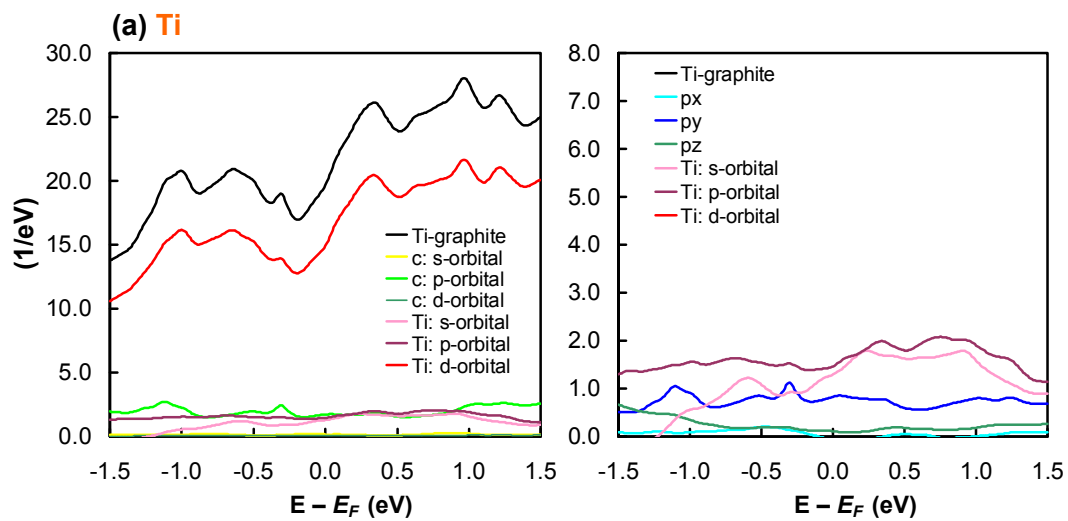
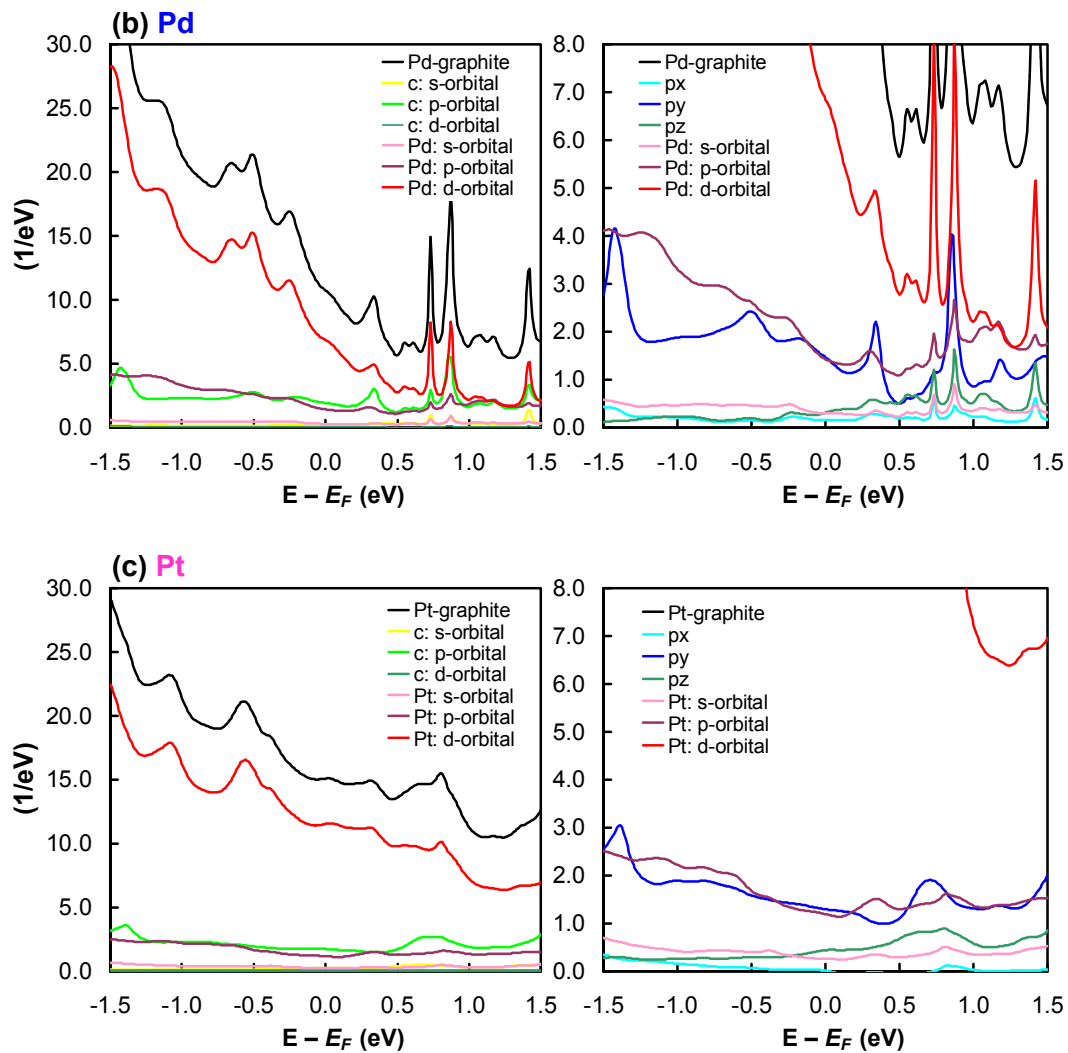
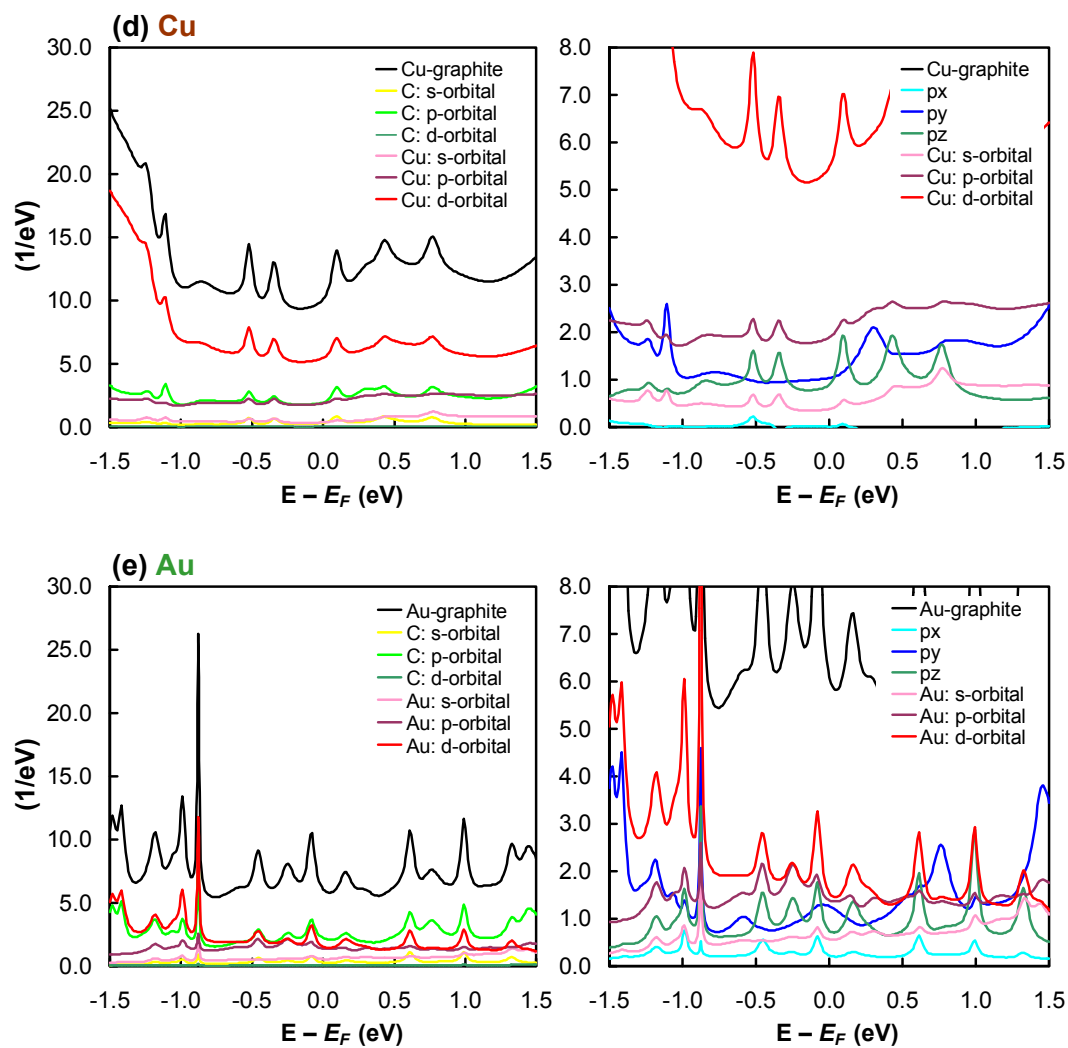


Figure S1-1. (a) Partial Density of States (PDOS) of Ti-graphene  $I-V$  model.



**Figure S1-2.** Partial Density of States (PDOS) of (b) Pd-graphene and (c) Pt-graphene  $I$ - $V$  models.



**Figure S1-3.** Partial Density of States (PDOS) of (d) Cu-graphene and (e) Au-graphene  $I$ - $V$  models.

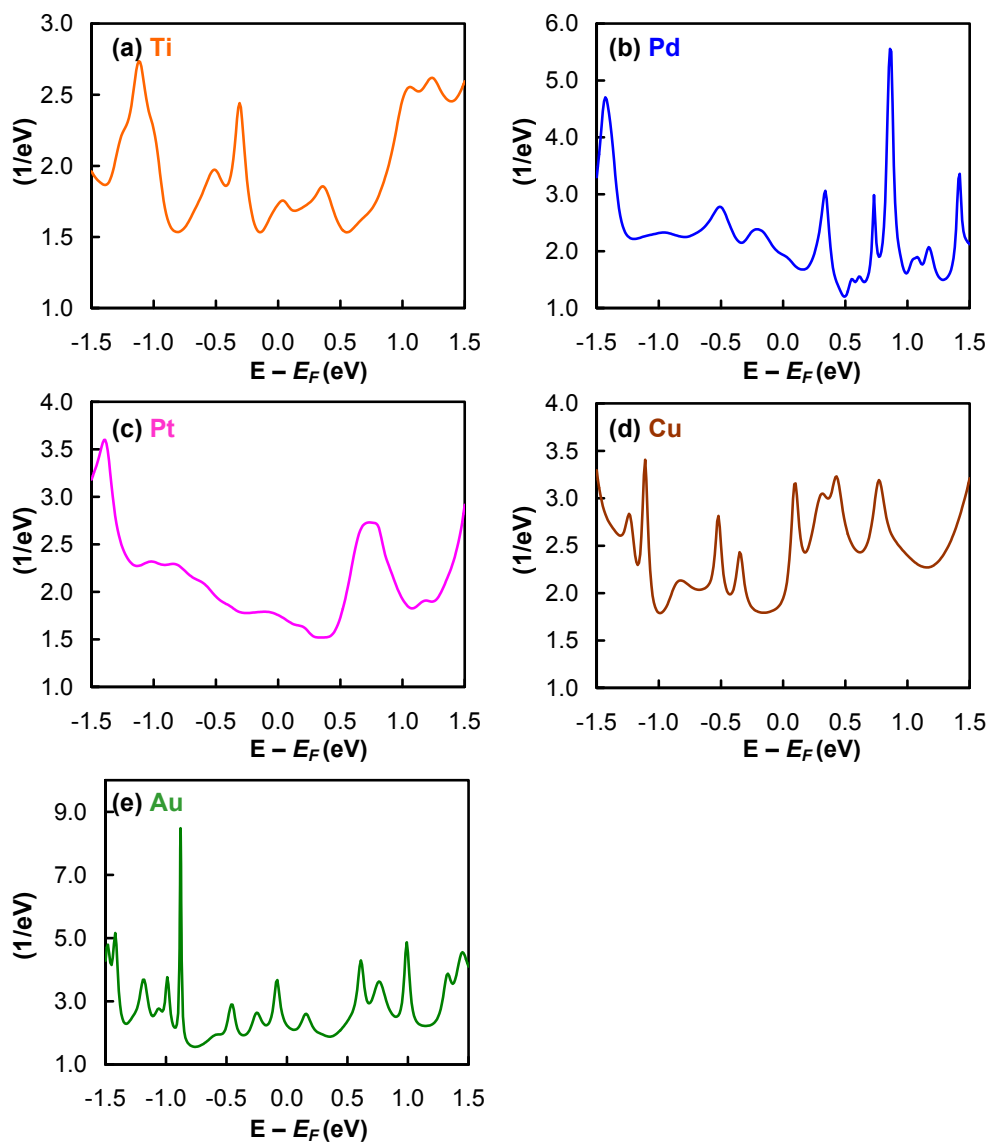


**Figure S2.** Partial Density of States (PDOS) of p orbital of surface C atoms on graphene.

(a) Ti, (b) Pd, (c) Pt, (d) Cu, and (e) Au  $I$ - $V$  models.

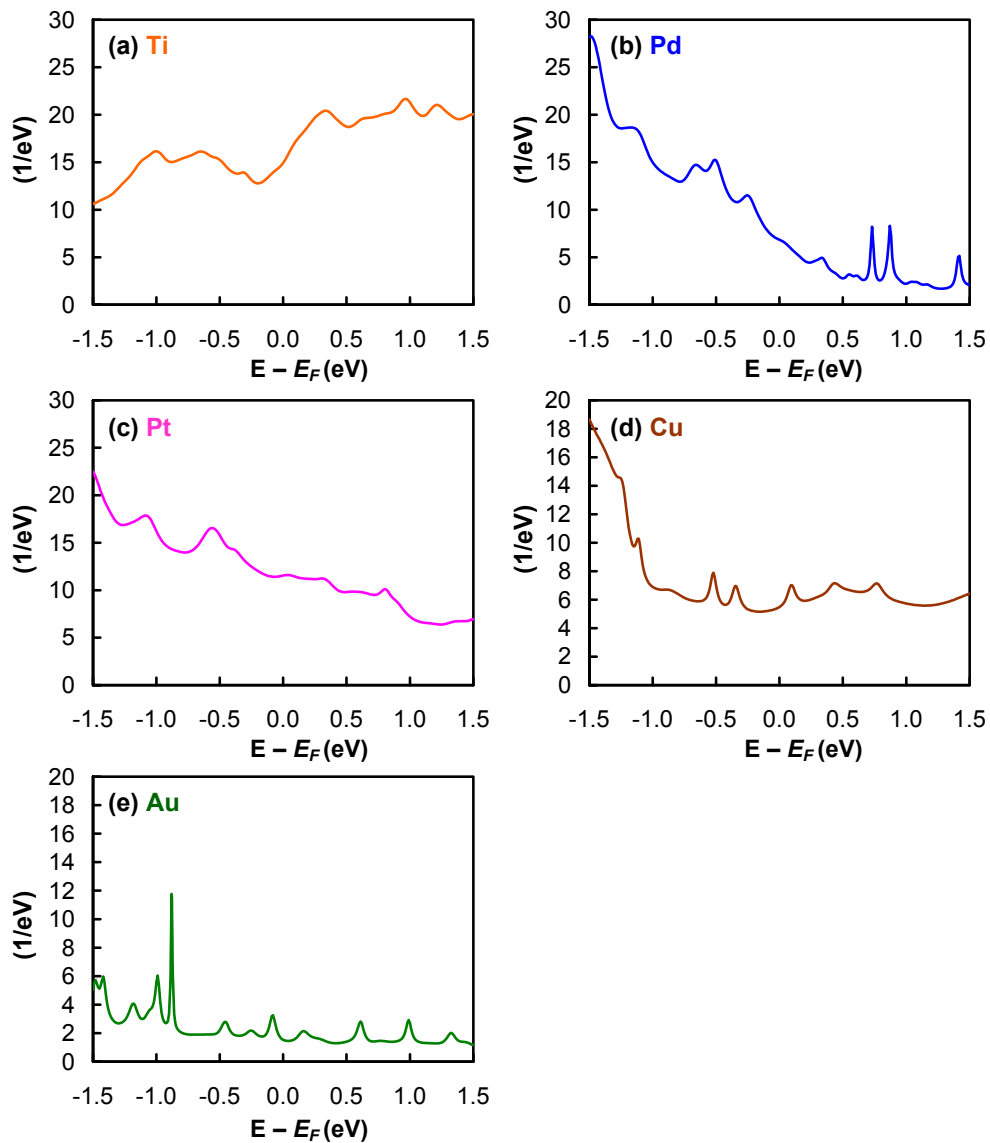


**Figure S3.** Partial Density of States (PDOS) of d orbital of surface metal atoms. (a) Ti, (b) Pd, (c) Pt, (d) Cu, and (e) Au  $I$ - $V$  models.

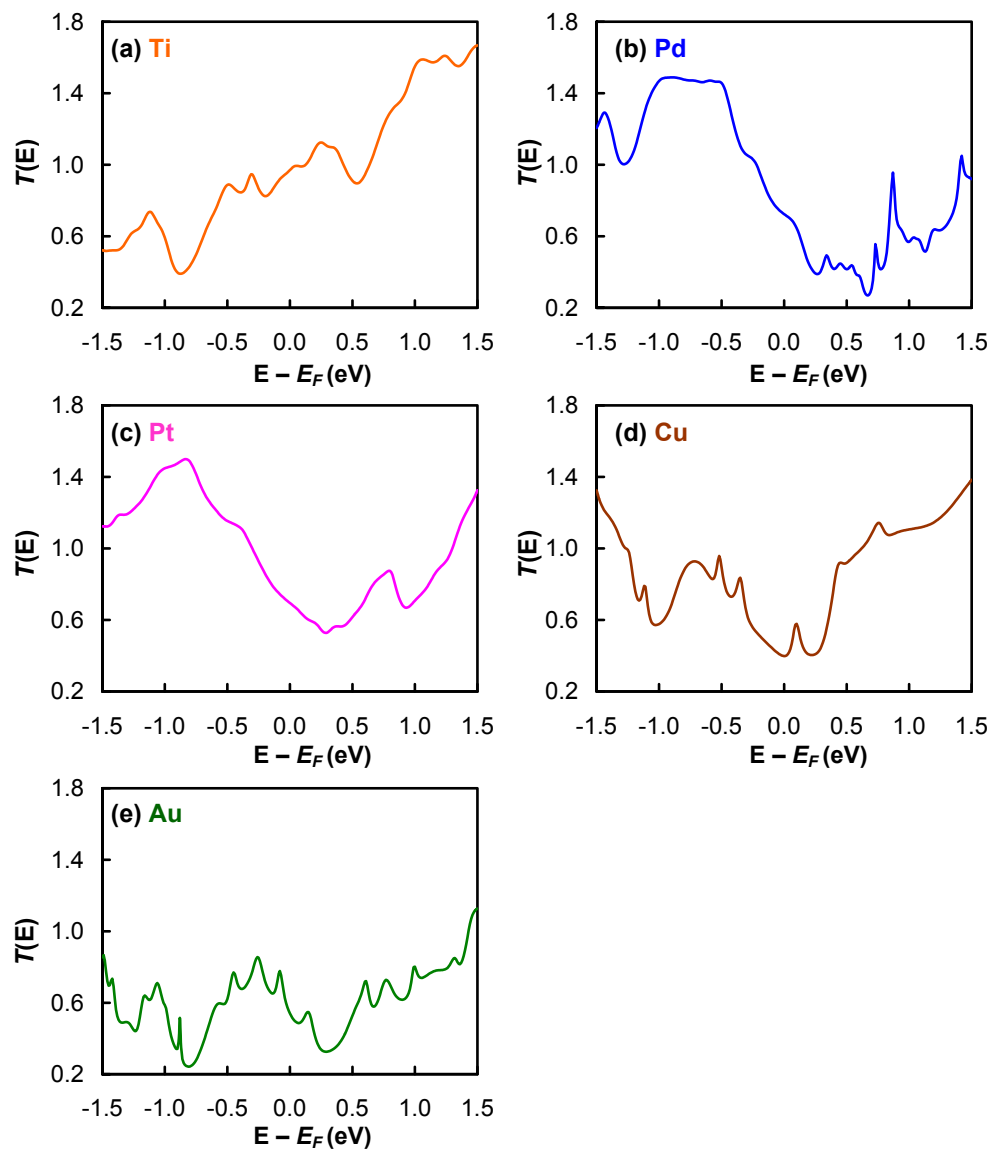


**Figure S4.** Transmission coefficient ( $T(E)$ ) of (a) Ti, (b) Pd, (c) Pt, (d) Cu, and (e) Au  $I-V$  models.

## Chapter 4

### Definitive Band Gaps in Single-Walled Carbon Nanotubes\*

#### Abstract

We report ab-initio quantum mechanical calculations of band structures of single-walled carbon nanotubes (SWNTs) using the B3LYP density functional. We show that the small band gaps in “metallic” zigzag SWNTs, as well as other detailed properties extracted from the band structures, show excellent agreement with previous experimental studies. The calculated band gaps and effective masses are inversely proportional to the square of the diameter, which is the most significant property in designing CNTs.

---

\* Yuki Matsuda, Jamil Tahir-Kheli, and William A. Goddard III. Manuscript is in preparation.

## 1. Introduction

Carbon nanotubes (CNTs) provide a number of unique and special properties that suggest great promise for nanoelectronic applications. In particular, the high electrical conductivity of quantum wires can be most important for on-chip interconnect metals and transistors of future integrated circuits.

One crucial obstacle to overcome such applications is the controlling of whether the CNT is metallic or semiconducting. The critical parameter in determining the electronic properties of CNTs are the chiral vectors,  $C_h = (na_1 + ma_2) \equiv (n, m)$ , where  $a_1$  and  $a_2$  are integers and the real space unit vectors of the graphene sheet, specifying the way in which the graphene sheet is wrapped. When  $n - m$  is a multiple of three, the CNT is metallic, otherwise it is a semiconductor. Thus armchair  $(n, n)$  CNTs are always metallic but zigzag  $(n, 0)$  CNTs are expected to be metallic when  $n$  is a multiple of 3.

However, Lieber et al.<sup>1</sup> showed that some  $(n, 0)$  zigzag single-walled carbon nanotubes (SWNTs) have finite band gaps [ $0.080 \pm 0.005$  eV band gap for  $(9,0)$ ,  $0.042 \pm 0.004$  eV for  $(12,0)$ , and  $0.029 \pm 0.004$  eV for  $(15,0)$ ] when measured under ultrahigh vacuum conditions at 5 K on Au(111) substrate.

Previous quantum mechanical (QM) calculations were not able to account for the detailed trend in band gaps observed experimentally. Thus local density approximation (LDA) functional calculations led to 0.024 eV for  $(9,0)$ , 0.002 eV for  $(12,0)$ , and 0 eV for  $(15,0)$  which are 70%, 95%, and 100% too small. It is well known that LDA will lead to band gaps which are too small. A common approach to correcting these too-small band gaps from LDA is the GW approximation which is used to include many-body corrections, but

for (9,0) this leads to a band gap which is too large by 213%.<sup>2</sup> The Perdew–Burke–Ernzerhof (PBE) generalized gradient approximation (GGA) functional leads to band gaps of 0.030 eV for (9,0), 0.010 eV for (12,0), and 0 eV for (15,0) which are 63%, 86%, and 100% too small, which is very similar to the results from LDA. Moreover, Perdew–Wang 91 (PW91) generalized gradient approximation (GGA) functional with uniform scale factor (1.20) corrections<sup>3</sup> provides a 0.20 eV band gap for (9,0), 0.08 eV for (12,0), and 0.14 eV for (15,0), which are 250%, 190% and 483% of the experimental values respectively and do not follow a consistent trend.

Since the band gap is the most significant property in designing CNTs for electronics applications, it is necessary to find a way of predicting accurate band gaps. In this paper, we show that the Becke–Lee–Yang–Parr (B3LYP) flavor of density functional<sup>4</sup> theory leads to accurate band gaps of these zigzag SWNTs, gaps of 0.079 eV for (9,0), 0.041 eV for (12,0) and 0.036 eV for (15,0) which are 99%, 99% and 123% (100%, 100% and 108% including the measurement deviation) of the experimental values respectively. Since B3LYP does well for energy gaps we expect that it should be accurate for other properties such as effective masses and the Fermi velocity which are also needed for designing nanoelectronic devices. We also report properties of other (n,0) zigzag CNTs, where we find that both (6,0) and (24,0) are metallic.

This B3LYP flavor DFT combines the Becke exchange potential with Hartree-Fock (HF) exact exchange plus the Lee–Yang–Parr correlational functional.<sup>4</sup> B3LYP has been validated by providing the most accurate cohesive energies, ionization potentials and electron affinities for a range of finite molecules.<sup>5,6</sup> In addition, B3LYP has been shown to provide accurate band gaps for undoped cuprate  $\text{La}_2\text{CuO}_4$  (an insulating spin-1/2

antiferromagnet)<sup>7</sup> and many other semiconductors and insulators<sup>8</sup>. Apparently, the inclusion of exact HF exchange helps to correct for self energy problem with standard DFT formulations. Based on these successes, we decided to test using the B3LYP functional to solve the problem of CNT band gaps.

We show here that B3LYP flavor of density functional theory quantum mechanics successfully determines the accurate band gaps of these zigzag SWNTs. Our results provide useful guidelines and proposals for SWNT applications in nanoelectronics.

## 2. Computational Methodology

To determine the structural parameters, we used the Graphite Force Field<sup>9</sup>, which leads to accurate properties of fullerene and CNT molecules and crystals.<sup>10,11</sup> The CNT geometries were fully optimized with no symmetry constraints. Detailed structural parameters are given in Table S1 (S denotes Supporting Information).

For the band calculations, we used CRYSTAL<sup>12</sup> software based on Gaussian basis sets with periodic boundary conditions. All electronic band structure calculations used the DURAND\_21G\* basis sets.<sup>13</sup>

## 3. Results and Discussion

Table 1 and Figure S1 compare experimental data<sup>14,15,16</sup> to the critical energies for band structures of diamond and graphite predicted by LDA, PBE, and B3LYP functionals. For diamond, we see that B3LYP leads to an indirect band gap of 5.5 eV compared to 5.5 eV

from experiment<sup>14</sup>, 3.9 eV from PBE and 3.3 eV from LDA. Similarly, the direct band gap at  $\Gamma$  point from B3LYP is 7.2 eV compared to 7.3 eV from experiment<sup>15</sup>, 5.5 eV from PBE and 5.3 eV from LDA. In graphite band structures all calculated bands cross at K point. The direct band gap at  $\Gamma$  point from B3LYP is 13.6 eV compared to  $\sim$ 13.1 eV from experiment<sup>16</sup>, 11.0 eV from PBE and 11.4 eV from LDA. The reason for the accurate band gaps predictions by B3LYP is the inclusion of exact Hartree–Fock (HF) exchange which better accounts for the self-exchange hole.

Figure 1a summarizes the band gaps of various SWNTs as a function of diameter. When  $d > 0.6$  nm, the band gaps of zigzag SWNTs which are semiconductors according to the chiral vector rule ( $n \bmod 3 \neq 0$ ) decrease as the diameter increases. The band gaps of two chiral SWNTs, (15,5) with  $d = 1.42$  nm and (14,7) with  $d = 1.46$  nm consisted of semiconductor zigzag SWNTs of same diameters. In particular, our B3LYP calculated  $E_g = 0.66$  eV for (15,5) with  $d = 1.42$  nm and 0.65 eV for (14,7) with  $d = 1.46$  nm are consistent with the experimentally observed  $E_g = 0.50 - 0.60 \pm 0.1$  eV for chiral SWNTs with  $d = 1.4 \pm 0.1$  nm by Dekker et al.<sup>17</sup> Thus the diameter is the dominant factor for band gaps.

For zigzag SWNTs with  $d < 0.6$  nm, we find that the band gap decreases for (7,0) and is zero (metallic) for (6,0) (5,0). The singly degenerate bands of the conduction band minimum (CBM), which cross ((5,0) and (6,0) SWNTs) and approach ((7,0) SWNT) the Fermi energy near  $\Gamma$  points (Figure S-1 a, b, and c), are due to the  $\sigma^* - \pi^*$  hybridization effects caused by the curvature of small diameter CNTs.<sup>18</sup> In these states, the  $\pi^*$  and  $\sigma^*$  states mix and repel each other, leading to lower pure  $\pi^*$  states. As common tight-binding approaches fail to describe asymmetrical charge transfer of the atoms, the  $\sigma^* - \pi^*$

hybridizations cannot be calculated, leading to the gaps in (5,0)<sup>19</sup> and (6,0) (e.g.  $E_g = 0.18$  eV for  $sp^3s^*$  tight-binding model<sup>20</sup>).

Figure 1b shows that the small band gaps in “metallic” zigzag SWNTs, which possess chiral vectors where  $n$  is a multiple of 3. There is excellent agreement between the experimental<sup>1</sup> and B3LYP band gaps for (9,0), (12,0), and (15,0) as described above (Table 2). These band gaps scale as  $\sim 1/d^2$ , a trend which continues for (18,0) and (21,0). However, for (6,0) and beyond (24,0), we find no band gap ( $E_g = 0$ ). These trends can be understood in Figure 2, which shows the  $\pi - \pi^*$  coupling near the expected crossing points (K points on the Brillouin zone) of  $3n$  in these zigzag SWNTs.

The reasons that support the presence of small band gaps are due to the intrinsic properties of the SWNTs and not due to other effects such as distortions at the measurement conditions of very low temperature ( $\sim 5$  K), ultra vacuum, and a Au(111) substrate. The low temperature leads to close conditions with our calculations and allows direct comparisons between the results. Next, the ultra vacuum allows little adsorbates on the surface of the SWNTs. Moreover, we had previously studied SWNTs or graphene sheets in contact with various metal surfaces, and show that Au(111) surface has little interaction.<sup>21</sup> The cohesive energy of Au(111)–C at equilibrium position (0.35 nm) is 0.13 kcal/mol/atom, which is the worst of five metals (Ti with 6.0 kcal/mol/atom  $\gg$  Pd  $>$  Pt  $>$  Cu  $>$  Au). Even when the nanotube strain is as small as 0.01 kcal/mol / C atom for the Pd surface, a smaller strain is expected for the Au surface. Thus, we believe that the observed band gaps are intrinsic properties and did not result from the adsorbates or deformations by the interactions between Au surface and SWNTs.

Figure 3a shows the calculated effective electron ( $m_e^*$ ) and hole ( $m_h^*$ ) masses of semiconductor SWNTs from the band structures calculated by B3LYP. All effective masses are shown as  $m^*/m_e$ , where  $m_e$  is the electron mass and  $m_e^*$ . There are different trends for the effective masses of zigzag SWNTs for  $n = 3i + 1$  ( $i$  is integer) and  $n = 3i + 2$ . For (7,0) and (8,0) zigzag SWNTs, the asymmetry feature of conduction and valance bands lead to the different effective masses of electrons and holes, which also supports  $\sigma^* - \pi^*$  hybridizations. For larger diameter SWNTs, the symmetry of conduction and valance bands ( $\pi - \pi^*$ ) provides the same effective electron and hole masses. The trend of the effective masses of zigzag SWNTs, which are based on the subgroups when  $n = 3i + 1$  and  $n = 3i + 2$ , can be explained by how the allowed  $k$  points cross the corner of Brillouin zone. The allowed  $k$  points cross closer to the K points for  $n = 3i + 2$ , leading to the effective masses from the larger slope in the conduction and valance bands which corresponds to the cross sections of  $\pi$  orbitals in three dimensions. They scale as diameter squared when  $d > 1.0$  nm ( $i > 16$  for  $n = 3i + 1$ , and  $i > 11$  for  $n = 3i + 2$ ) (Figure 3b). Since the allowed  $k$  points cross closer to the K points with larger diameters, the effective masses and band gaps decrease.

#### 4. Conclusion

In summary, we find that the B3LYP hybrid functional is a powerful tool for studying accurate band gaps of SWNTs, which shows excellent agreement with previous experimental studies. Notably, the presence of the small band gaps in the “metallic” zigzag (9,0), (12,0), and (15,0) are significant for applications of SWNTs in

nanoelectronics, where metallic or semiconductor property is most important. Thus B3LYP can describe accurately both the  $\pi - \pi^*$  couplings and the  $\sigma^* - \pi^*$  hybridizations, which previous calculations using LDA, PBE, GGA and tight-binding failed to do. In addition, we also show the band gaps and effective masses are inversely proportional to the diameter squared at  $d > 1.3$  nm. We believe that this study provides useful and important guidelines for experimentalists to characterize or design CNT based nanodevices.

**Acknowledgements.**

This work was supported partially by Intel Components Research (Kevin O'Brien, Florian Gstrein, and James Blackwell) and by the National Science Foundation (CCF-0524490 and CTS-0608889). The computer systems used in this research were provided by ARO-DURIP and ONR-DURIP. Additional support for the MSC was provided by ONR, ARO, DOE, NIH, Chevron, Boehringer-Ingelheim, Pfizer, Allozyne, Nissan, Dow-Corning, DuPont, and MARCO-FENA.

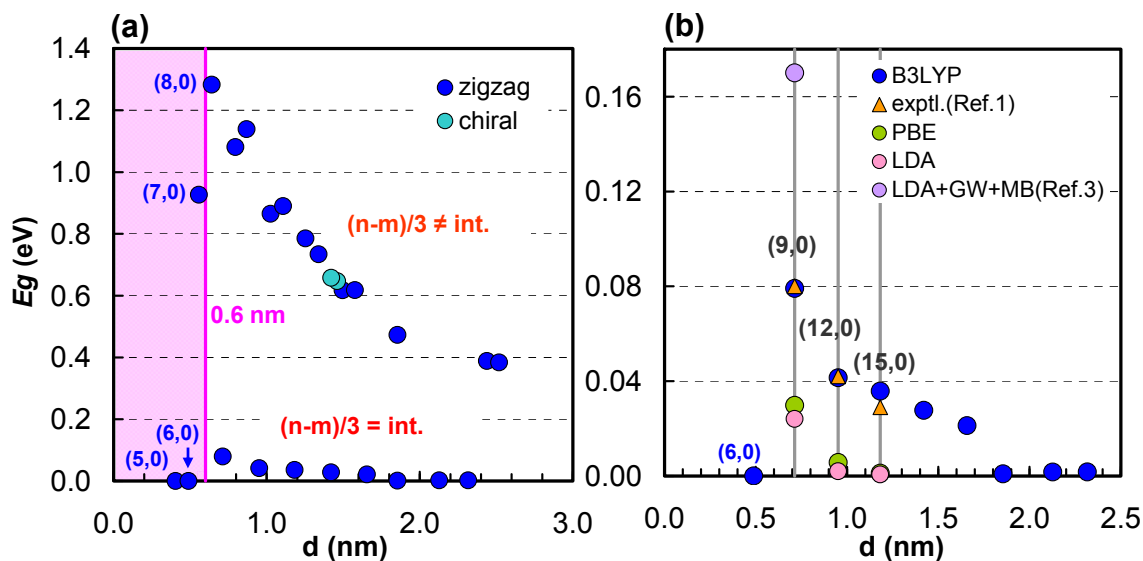


**Figure 1.** (a) Band gaps of zigzag SWNTs (dark blue circle) calculated by B3LYP as a function of diameter. Chiral SWNTs (light blue circle), (15,5) of  $d = 1.42$  nm and (14,7) of  $d = 1.46$  nm, are plotted. (b) B3LYP band gaps of zigzag SWNTs with  $(n - m)/3 = \text{integer}$  as a function of diameter (blue circle). For comparison, experimental data<sup>1</sup> (orange triangle), PBE (yellow green circle), LDA (pink circle), LDA + GW approximation + Many-body effect<sup>3</sup> (violet circle) are shown.

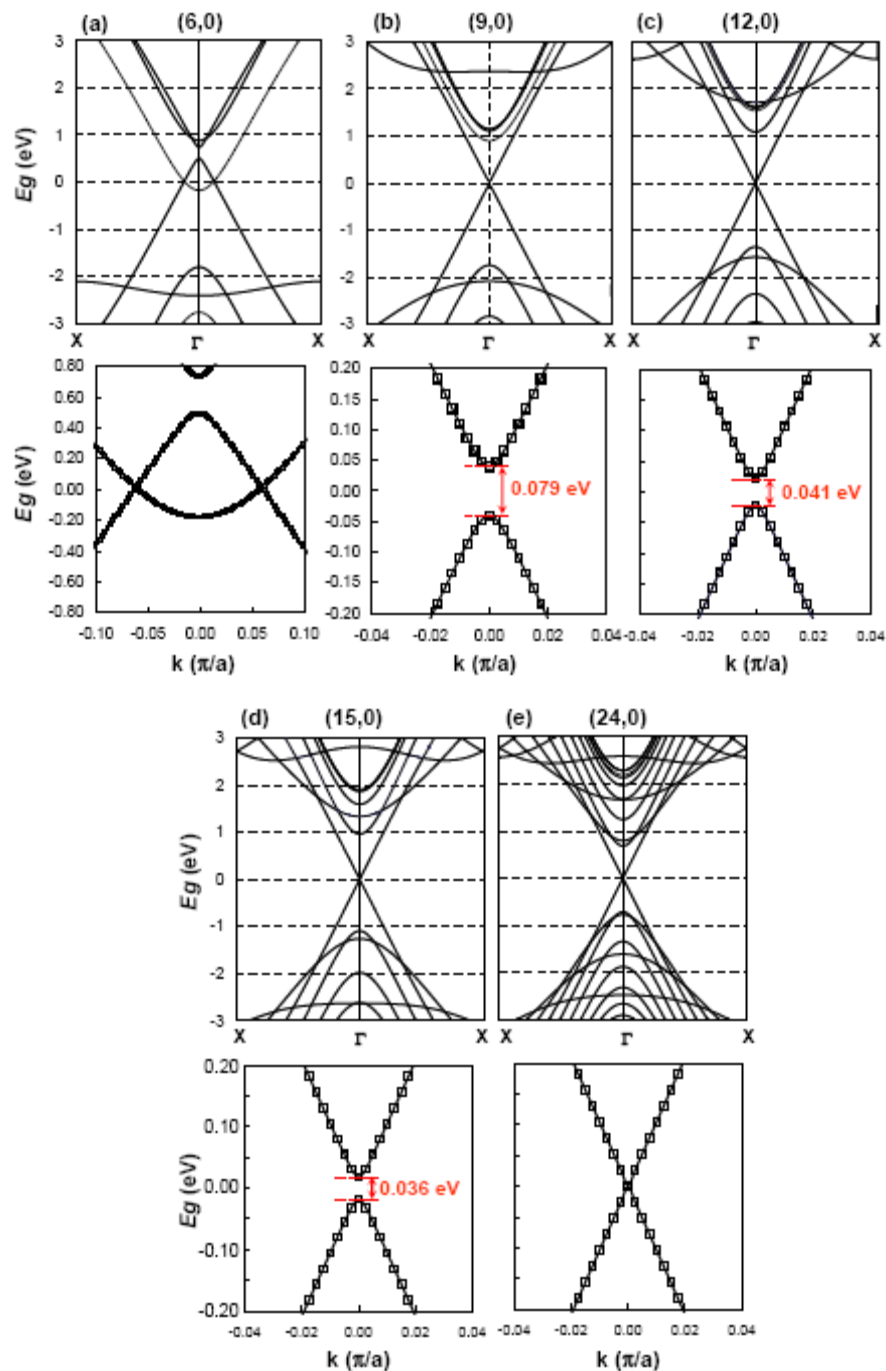


**Figure 2.** Band structures of (a) (9,0), (b) (12,0), (c) (15,0), (d) (18,0), and (e) (24,0) zigzag SWNTs (top) with enlarged scale near the Fermi energy (bottom). The small gaps are in good agreement with the experimental data by Lieber et al. (Table 1).<sup>1</sup>

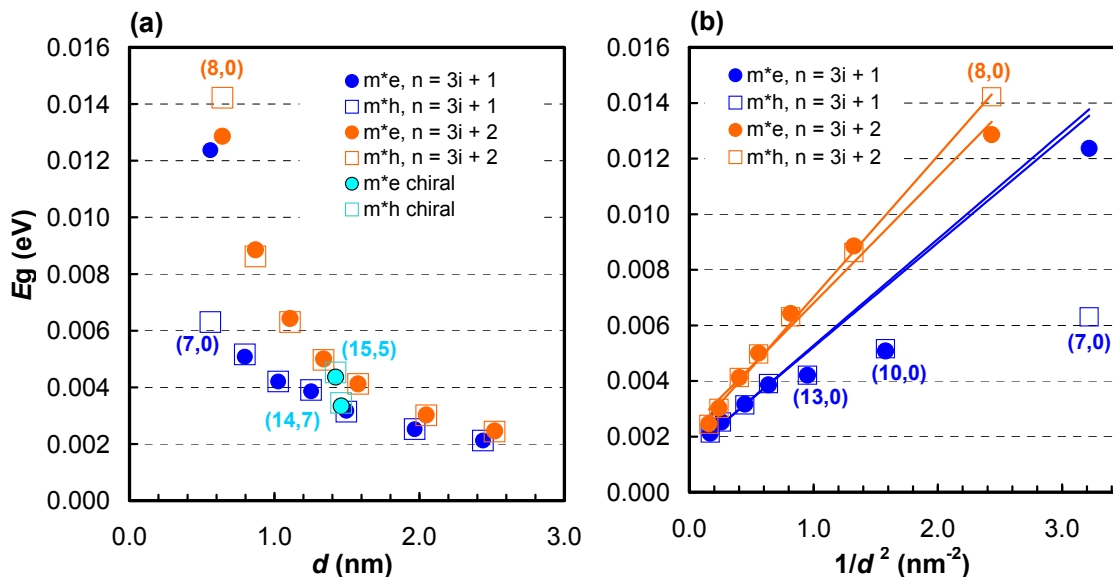


**Figure 3.** (a) Calculated effective electron ( $m^*_e$ ) and hole ( $m^*_h$ ) masses of semiconductor SWNTs from the B3LYP band structures as a function of diameter. (b) Effective masses of zigzag SWNTs scales as diameter squared.

All effective masses are shown as  $m^*/m_e$ , where  $m_e$  is the electron mass and  $m^*_e$  are shown in solid circles and  $m^*_h$  are in blank squares (blue,  $n = 3i + 1$  ( $i$  is integer); orange,  $n = 3i + 2$ ; light blue, chiral).

**Table 1.** Band Gap of Diamond and Graphite using Different Functional (LDA, PBE and B3LYP) Compared with Observed Gaps (eV).

		LDA	PBE	B3LYP	observed
diamond	indirect	3.3	3.9	5.5	5.5 <sup>a</sup>
	$\Gamma$	5.3	5.5	7.2	7.3 <sup>b</sup>
graphite	$\Gamma^c$	11.0	11.4	13.6	$\sim 13.1^d$

<sup>a</sup> Ref. 14.

<sup>b</sup> Ref. 15.

<sup>c</sup>  $\sigma - \sigma^*$  transition

<sup>d</sup> Ref. 16.

**Table 2.** Band Gaps ( $E_g$ ) of “Metallic” ( $(n - m)/3 = \text{integer}$ ) Zigzag and Chiral SWNTs Using the B3LYP Functional Compared with Experimental, PBE, and LDA Gaps.

$n^a$	$m^a$	diameter (nm) <sup>b</sup>	B3LYP $E_g$ (eV)	experimental $E_g$ (eV)	PBE $E_g$ (eV)	LDA $E_g$ (eV)
6	0	0.489	0.00			
9	0	0.713	0.079	$0.080 \pm 0.005^c$	0.003	0.024
12	0	0.951	0.041	$0.042 \pm 0.004^c$	0.006	0.002
15	0	1.182	0.036	$0.029 \pm 0.004^c$	0.00	0.00
18	0	1.420	0.028			
21	0	1.655	0.021			
24	0	1.855	0.00			
27	0	2.217	0.00			
30	0	2.317	0.00			
5	5	0.557	0.00			
10	10	1.366	0.00	$0.00^c$		
8	2	0.725	0.00			

---

11	5	1.121	0.00
16	4	1.446	0.00
15	6	1.478	0.00

---

<sup>a</sup> Chiral vectors,  $C_h = (n, m)$

<sup>b</sup> After optimizations.

<sup>c</sup> Ref. 1.

**References**

- (1) Ouyang, M.; Huang, J.-H.; Cheung, C. L.; Lieber, C. M. *Science* **2001**, *292*, 702.
- (2) Miyake, T.; Saito, S. *Phys. Rev. B.* **2005**, *72*, 073404.
- (3) Sun, G.; Kürti, J.; Kertesz, M.; Baughman, R. H. *J. Phys. Chem. B.* **2003**, *107*, 6924.
- (4) Becke, A. D. *J. Chem. Phys.* **1993**, *98*, 5648. Stephens, P. J.; Devlin, F. J.; Chabalowski, C.F.; Frisch, M. J. *J. Phys. Chem.* **1994**, *98*, 11623.
- (5) Xu, X.; Goddard, W. A., III. *PNAS* **2002**, *99*, 15308.
- (6) Xu, X.; Kua, J.; Periana, R. A.; Goddard, W. A., III. *Organometallic* **2003**, *22*, 2057.
- (7) Tahir-Kheli, J.; Goddard, W. A. III *Phys. Rev. B.* **2007**, *46*, 014514.
- (8) Muscat, J.; Wander, A.; Harrison, N. M. *Chem. Phys. Lett.* **2003**, *342*, 397.
- (9) Guo, Y.; Karasawa, N.; Goddard, W. A. III. *Nature (London)* **1991**, *351*, 464.
- (10) Gao, G.; Çağın, T.; Goddard, W. A., III. *Phys. Rev. Lett.* **1998**, *80*, 5556.
- (11) Chen, G.; Guo, Y.; Karsawa, N.; Goddard, W. A., III. *Phys. Rev. B.* **1993**, *48*, 13959.
- (12) Dovesi, R.; aunders, V. R.; Roetti, C.; Orlando, R.; Zicovich-Wilson, C. M.; Pascale, F.; Civalieri, B.; Doll, K.; Harrison, N. M.; Bush, I. J.; D'Arco, Ph.; Llunell, M.,

*CRYSTAL 06 User's Manual*; University of Torino: Torino, **2006**.

<http://www.crystal.unito.it>

- (13) Causa, M.; Dovesi, R.; Roetti, C. *Phys. Rev. B* **1991**, *43*, 11937.
- (14) *Solid State Physics*; Ashcroft, N. W.; Mermin, N. D., W. B. Saunders Company: Florida, **1997**.
- (15) Roberts, R. A.; Walker, W. C. *Phys. Rev.* **1967**, *161*, 730.
- (16) Marchand, D.; Frétigny, C.; Laguës, M.; Batallan, F.; Simon, C.; Rosenman, I.; Pinchaux, R. *Phys. Rev. B* **1984**, *30*, 4788.
- (17) Wildöer, J. W. G.; Venema, L. C.; Rinzler, A. G.; Smalley, R. E.; Dekker, C. *Nature*, **1998**, *391*, 59.
- (18) Blase, X.; Benedict, L. X.; Shirley, E. L.; Louie, S. G. *Phys. Rev. Lett.* **1994**, *72*, 1878.
- (19) Saito, R.; Fujita, M.; Dresselhaus, G.; Dresselhaus, M. S. *Appl. Phys. Lett.* **1992**, *60*, 2004.
- (20) Cao, J. X.; Yan, X. H.; Ding, J. W.; Wang, D. L. *J. Phys.: Condens. Matter* **2001**, *13*, L271–L275.
- (21) Matsuda, Y.; Deng, W.-Q.; Goddard, W. A., III. *J. Phys. Chem. C* **2007**, *111*, 11113.

## Supporting Information

**Table S1.** Structural Parameters after the Force Field Optimization and the Band Gaps of Zigzag, Armchair, and Chiral SWNTs Calculated Using the B3LYP Functional

$n^a$	$m^a$	atoms / unit cell	diameter (nm)	periodicity <sup>b</sup> (nm)	B3LYP $E_g$ (eV)	experimental $E_g$ (eV)
5	0	20	0.404	0.423	0.00	
6	0	24	0.489	0.425	0.00	
7	0	28	0.577	0.426	0.927	
8	0	32	0.641	0.426	1.283	
9	0	36	0.713	0.427	0.079	$0.080 \pm 0.005^c$
10	0	40	0.796	0.427	1.081	
11	0	44	0.869	0.427	1.139	
12	0	48	0.951	0.427	0.041	$0.042 \pm 0.004^c$
13	0	52	1.026	0.427	0.865	
14	0	56	1.107	0.428	0.890	
15	0	60	1.182	0.428	0.036	$0.029 \pm 0.004^c$

16	0	64	1.253	0.428	0.785	
17	0	68	1.339	0.428	0.734	
18	0	72	1.420	0.428	0.028	
19	0	76	1.496	0.428	0.617	
20	0	80	1.577	0.428	0.618	
21	0	84	1.655	0.428	0.021	
24	0	96	1.855	0.428	0.00	
25	0	100	1.967	0.428	0.477	
26	0	104	2.048	0.428	0.473	
27	0	108	2.217	0.428	0.00	
30	0	120	2.317	0.428	0.00	
31	0	124	2.439	0.428	0.388	
32	0	128	2.519	0.428	0.384	
5	5	20	0.557	0.247	0.00	
6	6	24	0.686	0.247	0.00	
10	10	40	1.366	0.247	0.00	0.00 <sup>c</sup>
8	2	57	0.725	6.523	0.00	

---

11	5	268	1.121	2.022	0.00	
15	5	260	1.422	1.542	0.66	$0.50 - 0.60 \pm 0.1^d$
14	7	196	1.460	1.132	0.65	$0.50 - 0.60 \pm 0.1^d$
16	4	112	1.446	0.653	0.00	
15	6	156	1.478	0.891	0.00	

---

<sup>a</sup> Chiral vectors,  $C_h = (n, m)$ .

<sup>b</sup> Periodicity of unit cell in SWNT along direction.

<sup>c</sup> Ref. 1.

<sup>d</sup> Ref. 17.

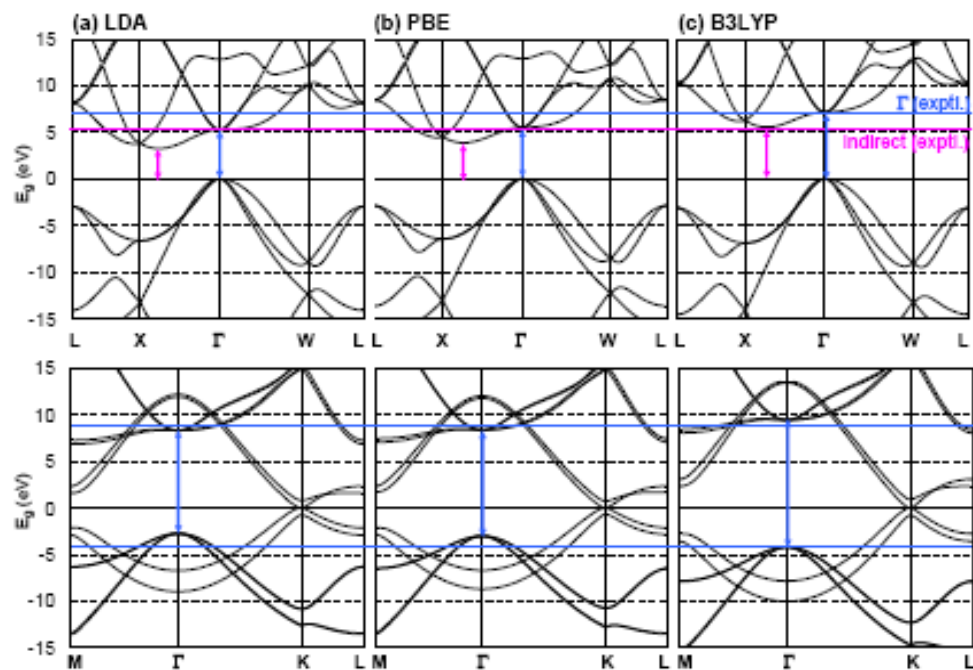


**Figure S1.** Band structures of diamond (top) and graphite (bottom) calculated by (a) LDA, (b) PBE, and (c) B3LYP. Experimental direct band gaps at  $\Gamma$  point (blue) and indirect band gaps (pink) are shown. The calculated and experimental band gaps are given in Table 1.

The STM measurements referred to in this paper were carried out in ultrahigh vacuum at  $\sim 5$  K on SWNT samples supported on Au(111) substrates. For purpose of comparison, we extracted the figures and figure captions from the original paper by Lieber et al.<sup>1</sup>

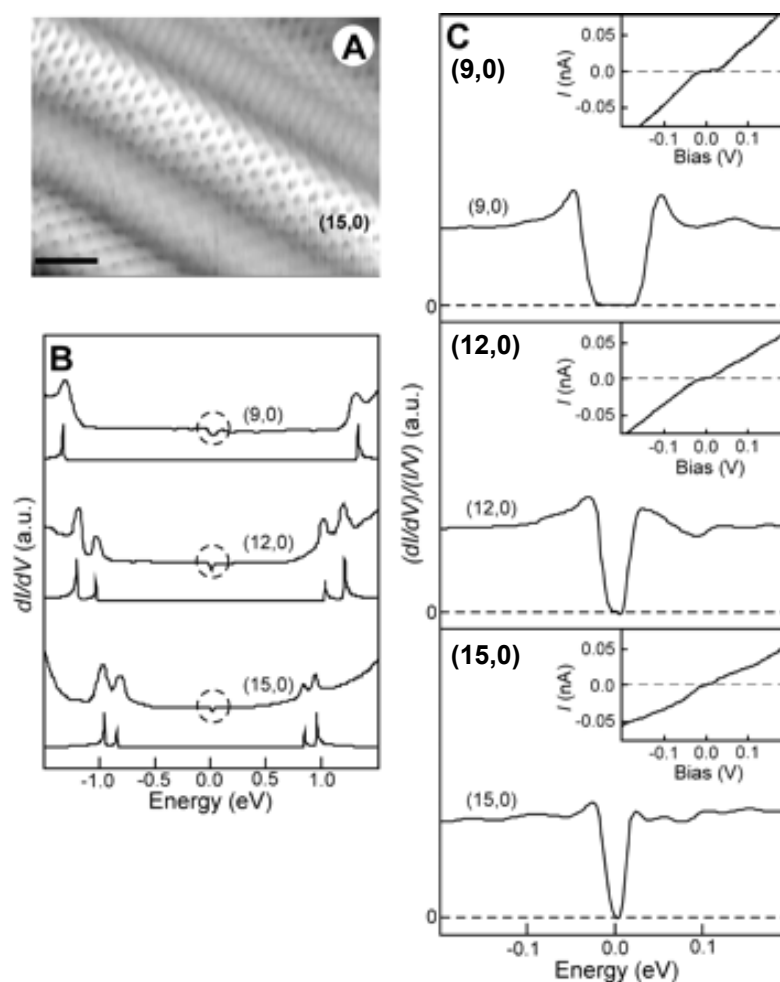


**Figure S2.** (Ref.1) Atomic structure and spectroscopy of "metallic" zigzag SWNTs. (A) Typical atomically resolved STM image of a (15,0) SWNT. The image was recorded in the constant-current mode with bias voltage of 0.65 V and current  $I$  of 0.15 nA. (Scale

bar: 1 nm). (B) Tunneling conductance data,  $dI/dV$ , for different zigzag SWNTs, with corresponding calculated DOS shown below each experimental curve in arbitrary units (a.u.). The data were recorded as the in-phase component of  $I$  directly by a lock-in amplifier with a 7.37-kHz modulation signal of 2 mV peak-to-peak amplitude to the bias voltage. The new features in the low-energy region of the (9,0), (12,0), and (15,0) tubes are highlighted by dashed circles. (C) Typical high-resolution normalized conductance  $(dI/dV)/(I/V)$  curves and measured  $I-V$  curves (insets) for (9,0), (12,0), and (15,0) tubes, respectively. The  $(dI/dV)/(I/V)$  curves were calculated from  $dI/dV$  and  $I-V$  data.

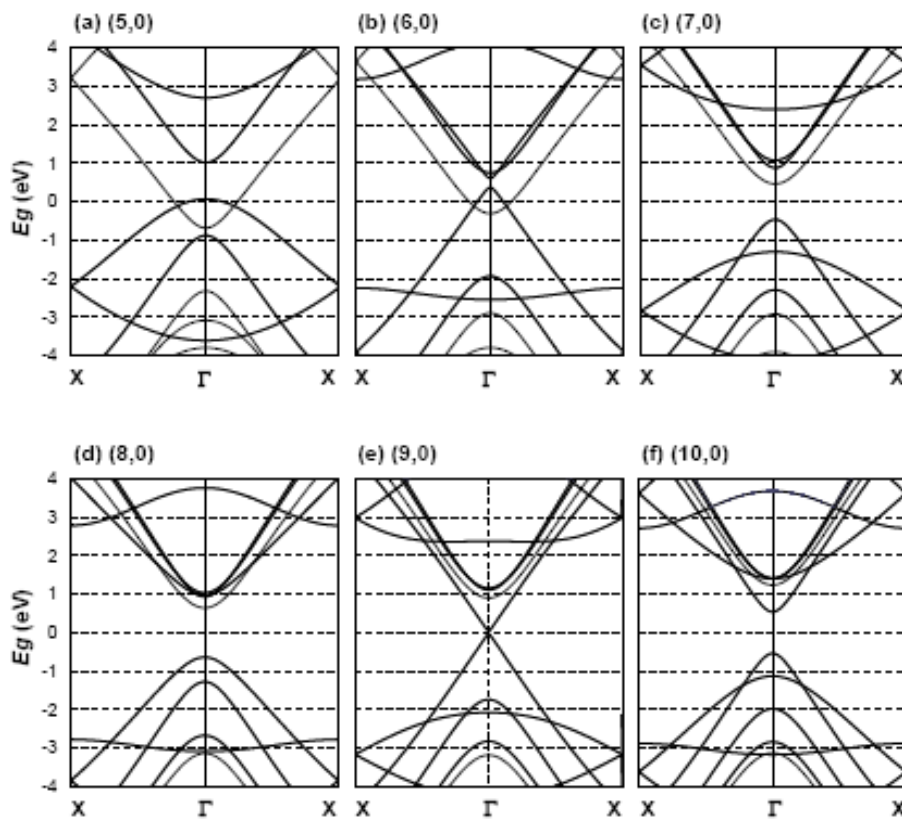


**Figure S3-1.** Band structures of zigzag SWNTs calculated using the B3LYP functional. (a) (5,0), (b) (6,0), (c) (7,0), (d) (8,0), (e) (9,0), and (f) (10,0).

According to the chiral vector rules, (5,0) indicates semiconductor, but due to the strong distortions resulting from a small diameter, it becomes metallic. (9,0) is metallic but there is a small band gap at the Fermi energy as shown in Figure 2.

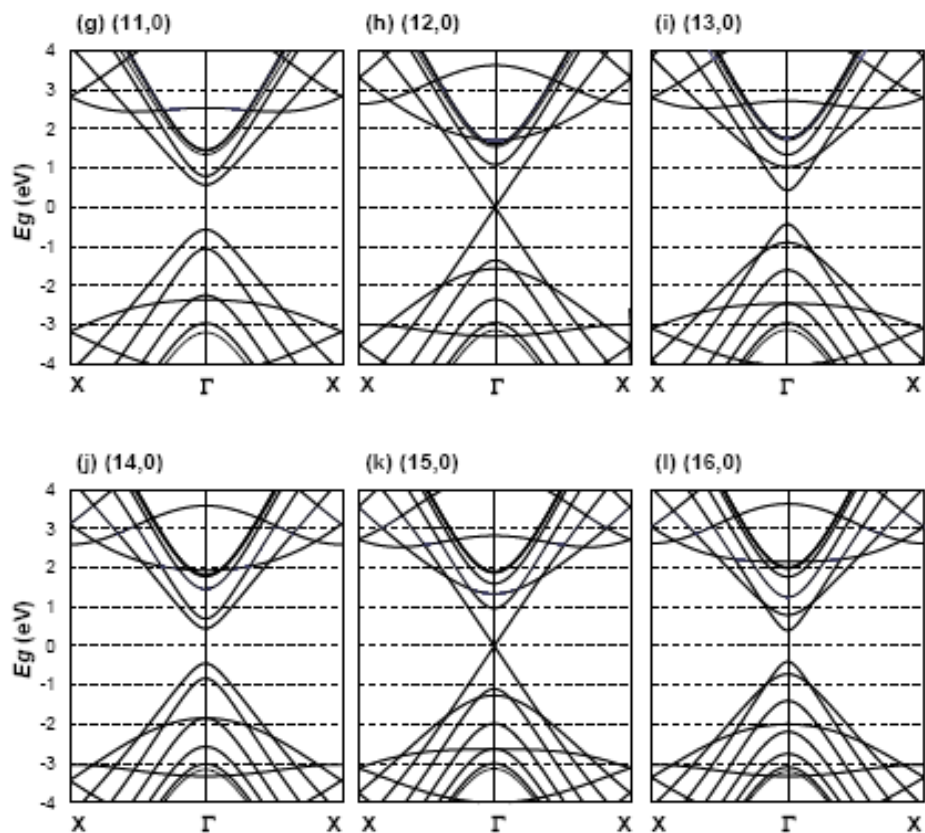


**Figure S3-2.** Band structures of zigzag SWNTs calculated using the B3LYP functional. (g) (11,0), (h) (12,0), (i) (13,0), (j) (14,0), (k) (15,0), and (l) (16,0).

According to the chiral vector rules, (12,0) and (15,0) are metallic but there are small band gaps at the Fermi energy as shown in Figure 2.

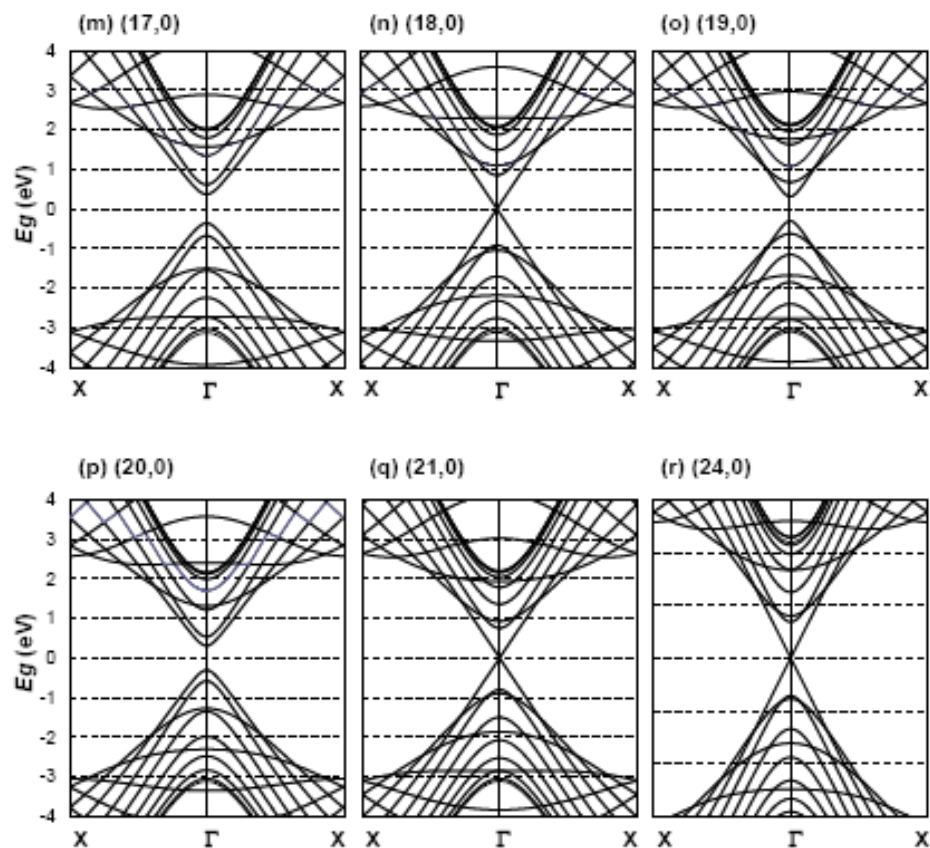


**Figure S3-3.** Band structures of zigzag SWNTs calculated using the B3LYP functional. (m) (17,0), (n) (18,0), (o) (19,0), (p) (20,0), (q) (21,0), and (r) (24,0).

According to the chiral vector rules, (18,0) and (21,0) are metallic but there are small band gaps at the Fermi energy as shown in Table 2. However, (24,0) shows metallic properties again (Figure 2).

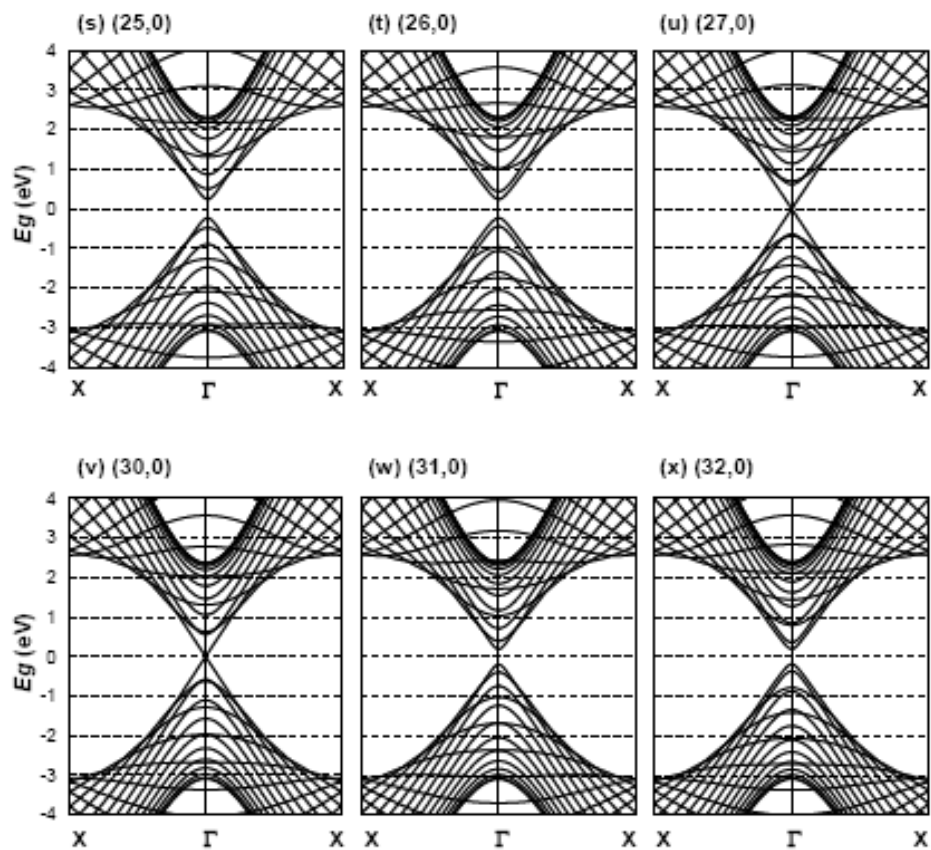


**Figure S3-4.** Band structures of zigzag SWNTs calculated using the B3LYP functional.

(s) (25,0), (t) (26,0), (u) (27,0), (v) (30,0), (w) (31,0), and (x) (32,0).

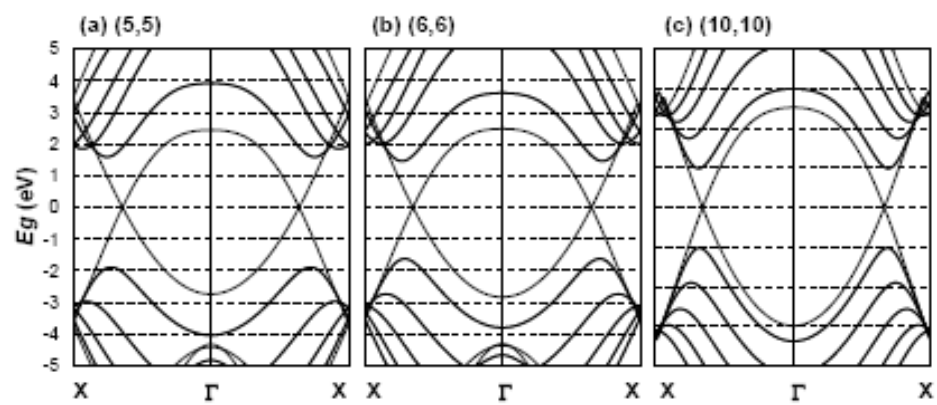


**Figure S4.** Band structures of armchair SWNTs calculated using the B3LYP functional.

(a) (5,5), (b) (6,6), and (c) (10,10).

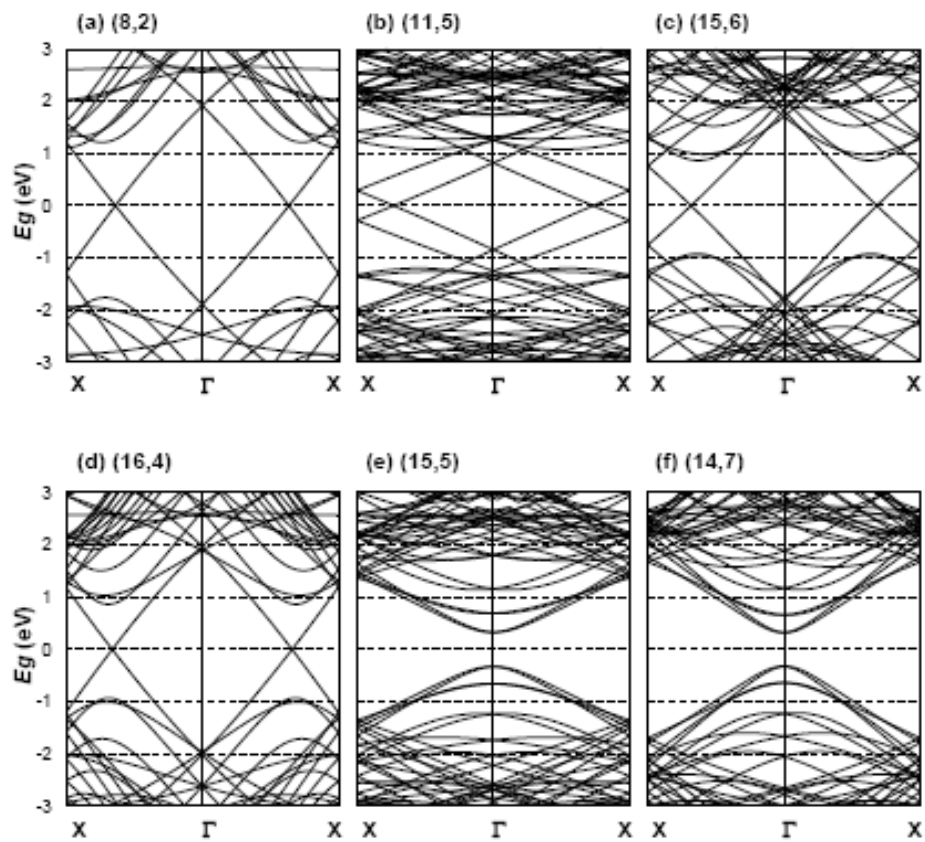


**Figure S5.** Band structures of chiral SWNTs of (a) (8,2), (b) (11,5), (c) (15,6), (d) (16,4), (e) (15,5), and (f) (14,7).

## Chapter 5

# Surface and Electronic Properties of Hydrogen Terminated Si [001] Nanowires\*

### Abstract

We report ab-initio quantum mechanical calculations of hydrogen terminated Si [001] nanowires (H-SiNWs) as a function of diameter ( $d$ ) and hydrogen coverage using the B3LYP density functional. For  $d \leq 1.9$  nm, fully saturated hydrogen coverage is more stable than unsaturated H-SiNWs. This explains the discrepancy between observed band gaps and prior theoretical calculations. For larger diameters, surface LUMO and HOMO states are formed. The direct band gap scales as  $1/d^2$  for saturated H-SiNWs and is well described by transverse quantization in the effective mass approximation. We conclude that controlling the diameter and surface hydrogen coverage of SiNWs is an effective method for optimizing the electronic properties for applications.

---

\* Yuki Matsuda, Jamil Tahir-Kheli, and William A. Goddard III. Submitted.

## 1. Introduction

Recent silicon nanowire (SiNW) fabrication techniques provide precise control of the crystallographic direction of the NW axis and its diameter and shape.<sup>1–18</sup> Exploiting these advances to tune SiNW electronic properties is important for the next generation of electronic devices or post CMOS materials. In fact, in the field of thermoelectrics, it has recently been shown that p-type SiNWs with diameters  $\leq 20$  nm have a thermoelectric figure of merit of  $ZT \approx 1$ , whereas the bulk value is  $ZT = 0.014$ .<sup>1,2</sup>

In practice, the superlattice nanowire pattern transfer (SNAP) method<sup>3</sup> provides a very general top-down approach to synthesizing large arrays of SiNWs of arbitrary diameter and orientation from either silicon wafers or films that can be patterned to form logic circuits (multiplexer)<sup>4</sup> and chemical sensors<sup>5</sup>. The alternative, bottom-up approach, grows SiNWs on metal catalysts (e.g., Au clusters) with diameters as small as 1.3 nm.<sup>6</sup> A variety of applications in electronics<sup>7</sup>, biological<sup>8</sup> and chemical<sup>9</sup> sensors, photonics<sup>10</sup>, and solar cells<sup>11</sup> using doped, coated or functionalized NWs<sup>12</sup> have been reported. The Langmuir–Blodgett approach<sup>13</sup> and layer-by-layer assembly processes<sup>14</sup> have also been successful, whereas catalyzed growth seems to exhibit orientation dependence.<sup>15–18</sup>

Despite these advances, fundamental questions of how the properties of SiNWs depend upon size, number and location of defects, and surface modifications is lacking. In addition, there are uncertainties about the relationship between the structural stability and surface properties that become important at nanoscale dimensions due to the large surface to bulk ratio in SiNWs.

For example, Si wafers are usually coated with a thermal oxide that tends to be passivating, leading to stable reproducible systems. However, for small NWs, the thickness of the oxide film becomes comparable to the diameter leading to undesirable surface electronic effects. Thus alternative ways to passivate the silicon surface may be necessary. One such method is chemical etching of silicon in a HF treatment that terminates the surface with H.<sup>6,19</sup>

In this paper, we have performed first principles quantum mechanical (QM) calculations on hydrogen terminated silicon nanowires (H-SiNWs) along the [001] direction with {100} and {110} surfaces to determine the electronic properties as a function of NW diameter and surface composition. Our results were obtained by first determining both the best shape of the SiNW cross section and the optimum coverage of hydrogen for each diameter. Second, we computed the band structure and relevant surface states and their scaling with diameter and surface hydrogen saturation.

We show that there is a crossover from fully saturated hydrogen surfaces for  $d < 1.9$  nm with valence and conduction band states delocalized over the NW to unsaturated hydrogen surfaces with valence and conduction wavefunctions localized on the surface. This leads to the evolution of the band gap with diameter consistent with experiment. Finally, we show that the evolution of the band gap as a function of diameter can be understood as arising from quantization of the momentum transverse to the NW axis.

These results are relevant for characterizing and designing SiNWs for wide-ranging applications.

## 2. Computational Methodology

Some Si atoms in the NWs may have 3 bonds plus a dangling bond. Correctly describing these states requires unrestricted or spin polarized wave functions where localized orbitals can be singly occupied. Closed shell (every band orbital doubly occupied) leads to large errors for these systems. For example, calculations of an unsaturated H-SiNW with diameter 2.5 nm ( $\text{Si}_{129}\text{H}_{12}$ ), described in detail below, finds the restricted-spin Becke-3-Lee-Yang-Parr<sup>20</sup> (RB3LYP) energy 1.58 eV higher than (unrestricted) UB3LYP. In addition, the RB3LYP band gap is 0.39 eV compared to the UB3LYP value of 1.60 eV (Figures S4 and S5). Therefore, all of our calculations allowed spin polarization (UB3LYP).

The most fundamental property used to design SiNWs for electronics applications is the band gap. It has recently been observed that the B3LYP<sup>20</sup> flavor of density functional theory quantum mechanics leads to reliable band gaps, whereas the local-density approximation (LDA) and generalized gradient approximation (GGA) methods do not.<sup>21-</sup>  
<sup>23</sup> B3LYP is a hybrid functional including 20% exact Hartree-Fock (HF) exchange in contrast to LDA and all GGA functionals that have no exact HF exchange. All previously reported QM calculations of the band gaps of SiNWs used LDA<sup>24-26</sup> or Perdew-Burke-Ernzerhof (PBE)<sup>27-31</sup> with plane wave basis sets<sup>24, 25, 27-31, 32</sup>. LDA and GGA DFT calculations generally lead to artificially low band gaps. The most dramatic example of the superiority of B3LYP for obtaining accurate band gaps is the undoped cuprate  $\text{La}_2\text{CuO}_4$  (an insulating spin-1/2 antiferromagnet). The experimental band gap of 2.0 eV is obtained by UB3LYP, whereas LDA and GGA functionals find a metal with no gap,  $E_g = 0$ .<sup>23</sup>

Including exact exchange is very difficult for periodic boundary condition (PBC) codes that are based on plane wave basis sets, such as VASP<sup>33</sup>, SIESTA<sup>34</sup>, ABINIT<sup>35</sup>, and ESPRESSO<sup>36</sup>. For PBC codes based on Gaussian basis sets (such as CRYSTAL), it is practical to include exact exchange. Thus, our calculations used CRYSTAL<sup>37</sup> for open/closed shell B3LYP band calculations. All of these calculations were performed with 66-21G\* basis sets for Si<sup>38</sup> and 3-1p1G for H<sup>39</sup>.

Structural geometry optimizations using PBE are known to be reliable and are computationally less expensive than B3LYP. Thus we used SEQUEST<sup>40</sup>, a fully self-consistent Gaussian-based linear combination of atomic orbitals (LCAO) density functional theory (DFT) method with double- $\zeta$  plus polarization (DZP) basis sets<sup>41</sup> to obtain the best geometries. These calculations used the PBE flavor of GGA<sup>42</sup> with PBE pseudo atomic potentials and spin polarization with no symmetry constraints. Six irreducible  $k$ -points in the Brillouin Zone were used. A real space grid spacing of 0.5 bohr was used based on by energetic convergence and prior calculations of Si surfaces.<sup>43</sup>

### **3. Results and Discussion**

#### **3.1. Surface Properties of H-SiNWs**

We optimized the structures of H-SiNW with diameters of 1.0, 1.3, 1.6, 1.9, 2.5, and 3.1 nm, using one dimensional (1D) periodic boundary conditions with a unit cell of 5.4 Å in the wire direction of [001]. We determined the optimum distribution of Si atoms and H termination. Generally, the NWs have an octagonal shape with four {100} plateaus that

dimerize with no H and four  $\{110\}$  plateaus that have one H per Si (Figure S2). At the corners of these 8 plateaus, we find the Si atoms bond to one or two H atoms.

We calculated the heats of formation with respect to the energies of bulk Si and hydrogen molecules for each optimized H–SiNW structure. The results are shown in Figure 1a as a function of the rescaled H/Si ratio where H and Si are the total number of the atoms in the unit cell. For each diameter, H/Si varies for the fully saturated case. We rescale this ratio for each diameter so that the fully saturated case has H/Si = 1. For each diameter  $d$ , the most stable SiNW is shown with red circles. For  $d \leq 1.9$  nm, the hydrogen saturated surface is more stable indicating that it is thermodynamically favorable for gas phase hydrogen molecules to react with the surface of SiNWs.

For  $d = 1.0$  nm in Figure 1b, the most stable structure is  $\text{Si}_{21}\text{H}_{20}$  with H/Si = 1.00. This has twelve surface Si atoms per unit cell where the middle Si atom has one H atom and the corner Si atoms have two H atoms. This leads to a heat of formation energy of  $E_h = 2.4$  kcal/mol per Si. Hereafter, the units for the energy are per Si atom unless stated otherwise. Removing four H atoms per cell from the saturated SiNW leads to an optimized H–SiNW (H/Si = 0.80,  $\text{Si}_{21}\text{H}_{16}$ ) has two H terminated Si–Si dimers at two corners and  $E_h = 5.5$  kcal/mol. Removing four more H atoms leads to an optimized H–Si [100] NW (H/Si = 0.60,  $\text{Si}_{21}\text{H}_{12}$ ) with four dangling bond Si atoms in addition to the two Si–Si dimers with  $E_h = 11.0$  kcal/mol. The detailed geometrical parameters of the H–SiNWs ( $d = 1.0$  nm) are also shown in Figure S1.

For  $d = 2.5$  nm, the unsaturated H–SiNWs (H/Si = 0.62,  $\text{Si}_{129}\text{H}_{32}$ ) is more stable structure than the saturated structure. It has eight H terminated Si dimers from the  $(2 \times 2)$

reconstruction of the  $\{100\}$  surface and four dangling Si bonds at the corner per unit cell (Figure S3a).

For  $d = 3.1$  nm, we find that the optimum NW has H/Si = 0.66 or  $\text{Si}_{196}\text{H}_{42}$  with  $E_h = 0.07$  kcal/mol. This H–SiNW is almost as stable as bulk Si plus hydrogen gas. It has ten Si dimers paired along the  $\{100\}$  side walls with two dangling bonds at the corners and saturated termination on the  $\{110\}$  surfaces. This leads to two dangling bond Si atoms per unit cell (Figure 1c). Binding an H to these two dangling bond states increases the energy by 0.95 kcal/mol and is due to the Si strains and H–H interactions.

The structural parameters for all the H–SiNWs are in Table S1. Saturated or equilibrium unsaturated models are shown in Figures S2 and S3. H–SiNWs for  $d = 2.5$  nm with various H/Si ratio are also shown in Figure S4.

### 3.2. Electronic Properties of H–SiNWs

Table 1 and Figure S5 compare the experimental band gap of bulk Si crystal to the results of different functionals (B3LYP, PBE, and LDA). B3LYP leads to a direct  $\Gamma$  point band gap of 3.8 eV compared to 3.5 eV from experiment<sup>44</sup> while PBE and LDA are smaller with values of 2.6 eV and 2.4 eV respectively. Similarly, the indirect band gap from B3LYP is 1.7 eV compared to 1.17 eV from experiment<sup>45</sup>. PBE is 0.4 eV and LDA is 0.2 eV. The reason for the improved band gaps for B3LYP is the inclusion of exact Hartree–Fock (HF) exchange that better accounts for the self-exchange hole.<sup>22, 23</sup>

The band structures of the saturated H–SiNWs ( $d = 1.0$  to 3.1 nm) all lead to a closed shell electronic structure (Figure 2). The band gap ranges from 4.1 eV ( $d = 1.0$  nm) to

2.2 eV ( $d = 3.1$  nm). The valance band maximum (VBM) is always located at  $\Gamma$  just as in bulk Si. There are two classes of conduction band minimum (CBM), one at the  $\Gamma$  point that leads to a direct band gap for  $d \leq 1.6$  nm and one  $\approx 1/3$  along  $\Gamma$  to X (the [100] direction) that leads to an indirect gap for  $d > 1.6$  nm. However, even at  $d = 3.1$  nm, the difference between the direct and indirect band gap is only 0.06 eV, whereas in bulk Si the difference is 3.5 (CBM) – 1.2 (VBM) = 2.3 eV. A direct band gap for  $d \leq 1.6$  nm opens the possibility of direct optical excitation without phonon emission. This is ideal for creating optical devices with SiNWs.

Table 2 shows the effective electron masses ( $m_e^*$ ) and hole masses ( $m_h^*$ ) of saturated H–SiNWs calculated from the band structures in Figure 2. We find that the effective masses approach the bulk values with increasing diameters.

For  $d = 3.1$  nm, the band structure and partial density of states (PDOS) of the most stable structure (H/Si = 0.21) calculated with unrestricted spin B3LYP (since they have two dangling bond Si atoms per unit cell) are shown in Figures 3a and 3b. The PDOS of the  $\alpha$  and  $\beta$  spin electrons show that the four dangling bond Si atoms lead to localized surface states for the HOMO and LUMO inside the band gap. The HOMO has spin  $\alpha$  and the LUMO is spin  $\beta$ . The direct band gap is 1.8 eV. This is close to the calculated indirect band gap of bulk Si of 1.7 eV. These dangling bond Si sites are likely to attract group III or V dopants<sup>30</sup> to promote surface conductivity. We expect this increased surface conductivity would further increase the ZT in p-type SiNWs.<sup>1,2</sup>

Finally, the direct band gaps calculated by B3LYP as a function of squared diameter ( $d^2$ ) in saturated H–SiNWs (red circle) are shown in Figure 4a. For  $d \geq 1.6$  nm, the band gaps

are indirect (blue circles) as described above. Since the equilibrium H–SiNWs structures at  $d = 2.5$  and  $3.1$  nm have unsaturated hydrogen coverage, the band gaps of those NWs are also shown. Without the HOMO and LUMO in these NWs created by the surface dangling bonds, the band gap is  $2.3$  eV. This is  $0.1$  eV smaller than the saturated H–SiNW of the same diameter ( $2.2$  eV) because the quantum confinement is slightly larger due to the reduced size of the reconstructed surface.<sup>27</sup> We expect the direct band gap to scale as  $1/d^2$  due to quantization of the  $k$ -vectors transverse to the NWs length. This leads to two different expressions in the effective mass approximation (EMA)<sup>46</sup> (assuming a square  $d \times d$  well or purely cylindrical wire with diameter  $d$ ). The gap is

$$E_g(\text{square}) = E_0 + \frac{\hbar^2 \pi^2}{m^* d^2} = E_0 + \frac{3.38}{d^2}, \quad (1)$$

$$E_g(\text{cylinder}) = E_0 + \frac{\hbar^2 (2 \times 2.405)^2}{m^* d^2} = E_0 + \frac{3.96}{d^2}, \quad (2)$$

where  $E_g$  is band gap (eV),  $E_0$  is bulk value (eV),  $d$  is diameter (nm), and  $m^*$  is the harmonic mean of the effective electron and hole masses (kg) of Si bulk,  $1/m^* = 1/m_e + 1/m_h$ . The  $2.405$  factor in equation (2) arises from the first root of the Bessel function,  $J_0$ .  $E_0 = 1.79$  for equation (1) with a square well model and  $1.61$  for equation (2) with a cylindrical model are obtained after least-square fits. The Si bulk value is  $1.7$  eV. Equations (1) and (2) show good agreement with the calculated band gaps at  $d > 1.3$  nm. Equation (1) is the better fit because the H–SiNW structure are approximately square (Figure 4b). The overestimation of the band gaps in small diameter H–SiNWs is expected using the EMA.<sup>46</sup>

Figure 4c shows the comparison of our results using B3LYP with previous theoretical studies on saturated H-SiNWs in the [001] growth direction.<sup>24,27,32</sup> along with the known experimental values<sup>6</sup>. The experimental values are for the [112] growth direction except for  $d = 3.0$  nm that was [110]. Prior calculations indicate that the band gaps of [001] NWs may be  $\sim 0.2$  eV smaller than those of [112] and [110].<sup>24,27,32</sup>

Clearly, the dependence of the band gap on diameter from experiment disagrees dramatically with all QM calculations. The experimental band gap of 3.5 eV for  $d = 1.3$  nm is in good agreement with our B3LYP calculated value of 3.4 eV for  $d = 1.3$  nm. The BPW91 density functional results of Wu<sup>32</sup> agrees with experiment at  $d = 2.5$  nm. We believe this agreement is purely fortuitous since the correct equilibrium structure at this diameter is unsaturated as we have shown above. Figure 4d shows the fit of the calculated band gap using the equilibrium structure to experiment. We believe this shows the narrower wires are unsaturated.

#### 4. Conclusion

We have shown that the band gaps of SiNWs are dramatically affected by the diameter and the level of coverage by adsorbates (e.g. hydrogen) on the surface. We show that all previous QM calculations on H-SiNWs lead to both magnitude and trend of the energy gaps with diameter that are in disagreement with experiment. In contrast, we find that the using thermodynamically stable level of hydrogen coverage in conjunction with B3LYP QM calculations leads to band gaps in good agreement with the experiment.

We find that the most stable level of hydrogen coverage is full saturation of surface Si bonds for diameters up to  $d \approx 2$  nm. For saturated H–SiNWs, we find that the QM band gaps from B3LYP scale inversely proportional to diameter squared and are fitted by the transverse quantization in the effective mass approximation. We also show that there is a direct band gap for  $d \leq 1.6$  nm and only a very small difference between the direct band and indirect band gaps for diameters up to 3.1 nm.

Moreover, for  $d \geq 2.5$  nm, we show that the equilibrium surface has a surface hydrogen coverage of  $\sim 66$  % leading to dimer pair Si atoms (similar to the Si {100} surface) plus dangling bond trivalent Si atoms. These dangling bond atoms lead to donor and acceptor surface states that decrease the band gap by 0.2 – 0.8 eV with respect to the saturated surface. It is this crossover from fully saturated and unsaturated H–SiNWs that is responsible for the dependence of the experimental band gap on diameters.

These results suggest that controlling the surface hydrogen coverage and diameter of SiNWs can be advantageous for tuning and enhancing optical performance, electrical conductivity, thermopower, and thermal conductivity. Similarly, the surface hydrogen atoms might be replaced by Cl, CH<sub>3</sub>, or CCH to further tune other properties.<sup>47</sup> In particular, the low direct band gap nature of these small diameter SiNWs may provide useful photovoltaic properties for solar energy as well as optical and optoelectronic applications.

**Acknowledgements.**

We thank Professor Seung Soon Jang and Dr. Youyong Li for helpful discussions. This research was supported partially by DARPA-ONR PROM (00014-06-0938) and NSF (CCF-0524490). The computer systems used in this research were provided by ARO-DURIP and ONR-DURIP. Additional support for the MSC was provided by ONR, ARO, DOE, NIH, Chevron, Boehringer-Ingelheim, Pfizer, Allozyne, Nissan, Dow-Corning, DuPont, and MARCO-FENA.

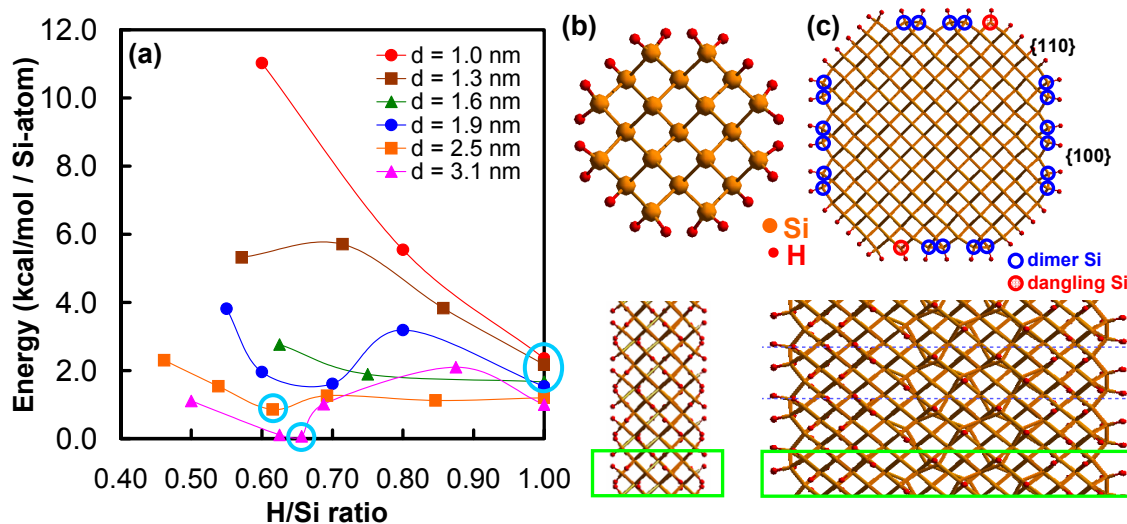


**Figure 1.** Optimized structures of H-SiNWs as a function of diameter. (a) Heats of formation vs. H/Si ratio for 1.0 nm (red); 1.3 nm (brown); 1.6 nm (green); 1.9 nm (blue); 2.5 nm (orange); 3.1 nm (pink). We rescale the H/Si ratio for each diameter so that the fully saturated case has H/Si = 1. The minimum energy of each case is shown with light blue circles. (b) Cross section (top) and side view (bottom) for  $d = 1.0$  nm, (H/Si = 1.00, Si<sub>20</sub>H<sub>21</sub>). The periodic unit length of 0.54 nm is shown with a green line. The square cross section is bounded by H saturated {110} surfaces on all four sides. (c) Cross section (top) and side view (bottom) for  $d = 3.1$  nm (H/Si = 0.66, Si<sub>196</sub>H<sub>42</sub>) (orange, Si; red, H). Here we find an octagonal cross section with four {100} like surfaces leading to ten dimer Si atoms (shown with blue circles) as in the (2 × 2) reconstruction and two dangling Si atoms (shown with red circles). The four {110} surfaces are saturated as in (b).

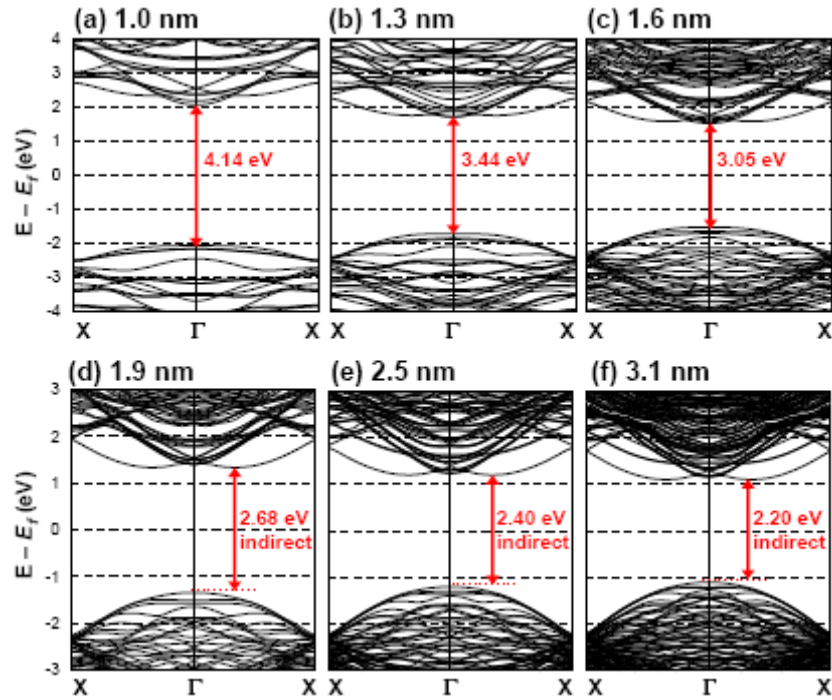


**Figure 2.** Band structures of saturated H-SiNWs using B3LYP. Diameter = (a) 1.0 nm, (b) 1.3 nm, (c) 1.6 nm, (d) 1.9 nm, (e) 2.5 nm, and (f) 3.1 nm. The VBM is at  $\Gamma$  just as in bulk Si. We find two classes of CBM, one at the  $\Gamma$  that leads to the direct band gap and one at  $1/3$  along the  $\Gamma$  to X. The latter leads to the indirect band gap. We find the smallest gap to be for  $d \leq 1.6$  nm.

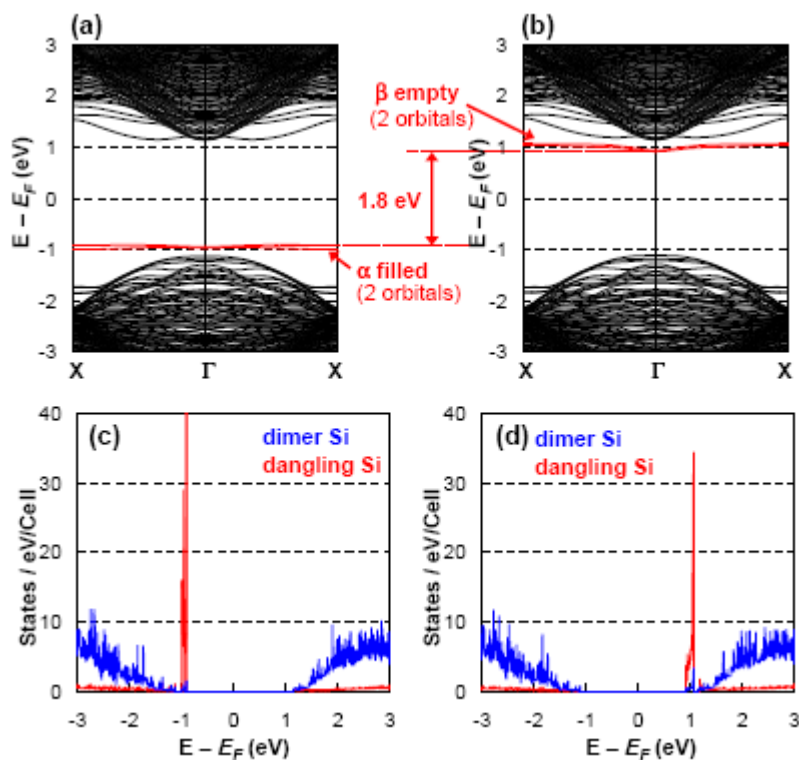


**Figure 3.** Band structures of the unsaturated H-SiNW with  $d = 3.1$  nm ( $\text{Si}_{196}\text{H}_{42}$ ) using UB3LYP. (a)  $\alpha$  electrons and (b)  $\beta$  electrons. Partial density of states of Si atoms (per unit cell) of (c)  $\alpha$  and (d)  $\beta$  electrons (blue; dimer Si atoms, red; dangling Si atoms). We find that the dangling bond Si atoms lead to new LUMO and HOMO states in the band gap.

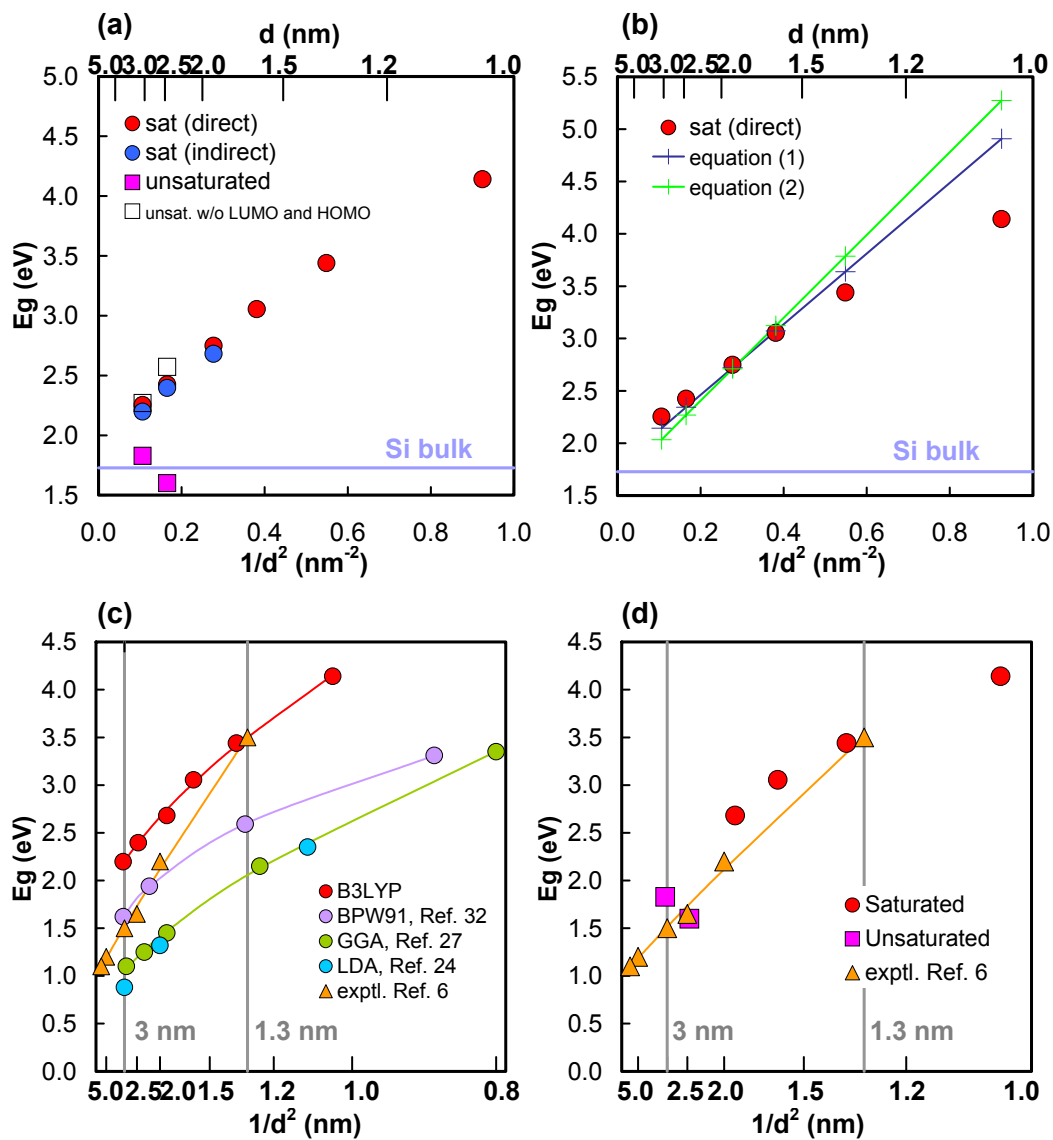


**Figure 4.** Band gap ( $E_g$ ) as a function of  $1/d^2$ .

(a) Calculated H-SiNWs band gaps using B3LYP. The red circles show the band gaps of saturated H-SiNWs. The blue circles show the indirect band gaps of saturated H-SiNWs. The orange squares show the band gaps of unsaturated H-SiNWs for  $d = 2.5$

and 3.1 nm. The blank squares show the band gaps without the LUMO and HOMO created by the surface states of unsaturated H–SiNWs.

(b) The expected direct band gap due to quantization in the effective mass approximation for saturated H–SiNWs from assuming a square  $d \times d$  well (blue, eq. (1)) and cylinder of diameter  $d$  (green, eq. (2)).

(c) Comparison of our saturated B3LYP band gaps to other theoretical studies, LDA (blue circle, Ref. 24), GGA (green circle, Ref. 27), and BPW91 (purple circle, Ref. 32), on saturated SiNWs are shown. The experimental data (orange triangle; Ref. 6) is [011] for  $d = 3\text{nm}$ , otherwise [211]. The fit to experiment is not good because for smaller diameters, the equilibrium H–SiNW structure is unsaturated.

(d) Plot of the lowest energy H–SiNWs structure band gaps (red circle, saturated at  $d < 1.9\text{ nm}$ ; pink square, unsaturated at larger  $d$ ) vs. experimental data (orange triangle, Ref. 6). B3LYP and the correct SiNW structures explain the experimental data well.

**Table 1.** Band Gap of Si Crystal (eV) Using Different Functional (B3LYP, PBE and LDA) Compared to Experimental Data

	B3LYP	PBE	LDA	experimental <sup>a</sup>
direct band gap	3.8	2.6	2.4	3.5
indirect band gap	1.7	0.4	0.2	1.17

<sup>a</sup> Ref. 45, 46

**Table 2.** Effective Electron and Hole Masses ( $m_e^*$  and  $m_h^*$ ) in Units of the Free Electron Mass) of Saturated H-SiNWs as a Function of Diameter from B3LYP Calculations.

diameter (nm)	Electrons $m_e^*$ <sup>a</sup>		Holes $m_h^*$
	min. along $\Gamma$ to X <sup>c</sup>	$\Gamma$ point	$\Gamma$ point
1.0	-	<b>0.77</b>	18.28
1.3	-	<b>0.88</b>	16.94
1.6	-	<b>0.84</b>	5.59
1.9	<b>0.98</b>	0.71	2.64
2.5	<b>1.54</b>	0.69	2.51
3.1	<b>1.54</b>	0.59	2.29
Si bulk	<b>1.63</b>	0.42	0.59 (heavy) 0.34 (light)
Si bulk (exptl.) <sup>b</sup>	<b>1.08</b>	-	0.49 (heavy) 0.16 (light)

<sup>a</sup> Values in boldface are the CBM.

<sup>b</sup> Ref. 46

<sup>c</sup> For H-SiNWs at  $d \geq 1.9$  nm, the CBM is at 33 % from  $\Gamma$  to X.

## References

- (1) Boukai, A. I.; Bunimovich, Y.; Tahir-Kheli, J.; Yu J.-K.; Goddard, W. A. III; Heath J. R. *Nature* **2008**, *451*, 168.
- (2) Hochbaum, A. I.; Chen, R.; Delgado, R. D.; Liang, W.; Garnett, E. C.; Najarian, M.; Majumdar, A.; Yan, P. *Nature* **2008**, *451*, 163.
- (3) Melosh, N. A.; Boukai, A.; Diana, F.; Gerardot, B.; Badolato, A.; Petroff, P. M.; Heath, J. R. *Science* **2003**, *300*, 112.
- (4) Beckman, R.; Johnston-Halperin, E.; Luo, Y.; Green, J. E.; Heath, J. R. *Science* **2005**, *310*, 465.
- (5) Mcalpine, M. C.; Ahmad, H.; Wang, D.; Heath, J. R. *Nature Materials* **2007**, *6*, 379.
- (6) Ma, D. D. D.; Lee, C. S.; Au, F. C. K.; Tong, S. Y.; Lee, S. T. *Science*, **2003**, *299*, 1874.
- (7) Lu, W.; Lieber, C. M. *Nature Mater.* **2007**, *6*, 841.
- (8) Patolsky, F.; Timko, B. P.; Zheng, G.; Lieber, C. M. *MRS Bull.* **2007**, *32*, 142.
- (9) Patolsky, F.; Zheng, G.; Lieber, C. M. *Nature Protocols* **2006**, *1*, 1711.
- (10) Yang, C.; Barrelet, C. J.; Capasso, F.; Lieber, C. M. *Nano Lett.* **2006**, *6*, 2929.
- (11) Tsakalakos, L.; Balch, J.; Fronoheiser, J.; Korevaar, B. A.; Sulima, O.; Rand, J. *Appl. Phys. Lett.* **2007**, *91*, 233117.
- (12) Lieber, C. M.; Wang, Z. L. et al. *MRS Bull.* **2007**, *32*, 99.

- (13) Whang, D.; Jin, S.; Wu, Y.; Lieber, C. M. *Nano Lett.* **2003**, *3*, 1255.
- (14) Javey, A.; Nam, S.; Friedman, R. S.; Yan, H.; Lieber, C. M. *Nano Lett.* **2007**, *7*, 773.
- (15) Wu, Y.; Cui, Y.; Huynh, Y.; Barrelet, C. J.; Bell, D. C.; Lieber, C. M. *Nano Lett.* **2004**, *4*, 433.
- (16) Li, C.-P.; Lee, C.-S.; Ma, X.-L.; Wang, N.; Zhang, R.-Q.; Lee, S. T. *Adv. Mater.* **2003**, *15*, 607.
- (17) Holmes, J. D.; Johnson, K. P.; Doty, R. C.; Korgel, B. A. *Science* **2000**, *287*, 1471.
- (18) Wang, C. X.; Hirano, M.; Hosono, H. *Nano Lett.* **2006**, *6*, 1552.
- (19) Hirashita, N.; Kinoshita, M.; Aikawa, I.; Ajioka, T. *Appl. Phys. Lett.* **1990**, *56*, 451.
- (20) Becke, A. D. *J. Chem. Phys.* **1993**, *98*, 5648. Stephens, P. J.; Devlin, F. J.; Chabalowski, C.F.; Frisch, M. J. *J. Phys. Chem.* **1994**, *98*, 11623.
- (21) Tahir-Kheli, J.; Goddard, W. A. III *Phys. Rev. B* **2007**, *46*, 014514.
- (22) Muscat, J.; Wander, A.; Harrison, N. M. *Chem. Phys. Lett.* **2003**, *342*, 397.
- (23) Perry, J. K.; Tahir-Kheli, J.; Goddard, W. A. III *Phys. Rev. B* **2001**, *63*, 144510.
- (24) Vo, T.; Williamson, A. J.; Galli, G. *Phys. Rev. B*, **2006**, *74*, 045116.
- (25) Peelaers, H.; Partoens, B.; Peeters, F. M. *Nano Lett.* **2006**, *6*, 2781.
- (26) Aradi, B.; Ramos, L. E.; Deak, P.; Kohler, Th.; Bechstedt, F.; Zhang, R. Q.; Frauenheim, Th. *Phys. Rev. B*, **2007**, *76*, 035305.
- (27) Leu, P. W.; Shan, B.; Cho, K. *Phys. Rev. B*, **2006**, *73*, 195320.

- (28) Durgun, E.; Akman, N.; Ataca, C.; Ciraci, S. *Phys. Rev. B*, **2007**, *76*, 245323.  
Durgun, E.; Cakir, D.; Akman, N.; Ciraci, S. *Phys. Rev. Lett.* **2007**, *99*, 256806.
- (29) Nolan, M.; O'Callaghan, S.; Fagas, G.; Greer, J. G. *Nano Lett.* **2007**, *7*, 34.
- (30) Fernandez-Serra, M. -V.; Adessi, Ch.; Blase, X. *Nano Lett.* **2006**, *6*, 2674.
- (31) Ponomareva, I.; Menon, M.; Richter, E. ; Andriotis, A. N. *Phys. Rev. B*, **2006**, *74*, 125311.
- (32) Ng, M. -F.; Zhou, L. ; Yang, S. -W. ; Sim, L. Y. ; Tan, V. B. C.; Wu, P. *Phys. Rev. B*, **2007**, *76*, 155435.
- (33) Kresse, D.; Furthmüller, J. *Comput. Mater. Sci.* **1996**, *6*, 15. Kresse, D.; Furthmüller, J. *Phys. Rev. B* **1996**, *54*, 11169.
- (34) M Soler, J. M.; Artacho, E.; Gale, J. D.; García, A.; Junquera, J.; Ordejón, P.; Sánchez-Portal, D. *J. Phys.: Condens. Matter* **2002**, *14*, 2745.
- (35) Gonze, X.; Beuken, J.-M.; Caracas, R.; Detraux, F.; Fuchs, M.; Rignanese, G.-M.; Sindic, L.; Verstraete, M.; Zerah, G.; Jollet, F.; Torrent, M.; Roy, A.; Mikami, M.; Ghosez, P.; Raty, J.-Y.; Allan, D. C. *Comput. Mater. Science* **2002**, *25*, 478.
- (36) Baroni, S.; de Gironcoli, S.; Dal Corso, A.; Giannozzi, P. et al., *The PWSCF Code*; DEMOCRITOS National Simulation Center of INFN: Trieste, Italy, **2008**.  
<http://www.quantum-espresso.org/>
- (37) Dovesi, R.; aunders, V. R.; Roetti, C.; Orlando, R.; Zicovich-Wilson, C. M.; Pascale, F.; Civalleri, B.; Doll, K.; Harrison, N. M.; Bush, I. J.; D'Arco, Ph.; Llunell, M.,

*CRYSTAL 06 User's Manual*; University of Torino: Torino, 2006.

<http://www.crystal.unito.it>

(38) Gordon, M.S.; Binkley, J.S.; Pople, J.A.; Pietro, W.J.; Hehre, W.J. *J. Am. Chem. Soc.* **1982**, *104*, 2797. Binkley, J. S.; Gordon, M. S.; DeFrees, D. J.; Pople, J. P. *J. Chem. Phys.* **1982**, *77*, 3654.

(39) Gatti, C.; Saunders, V.R.; Roetti, C. *J. Chem. Phys.* **1994**, *101*, 10686.

(40) Schultz, P. A. *SEQQUEST code*; Sandia National Labs: Albuquerque, NM, 2005.  
<http://dft.sandia.gov/Quest/>.

(41) Mattsson, A. E.; Schultz, P. A.; Desjarlais, M. P.; Mattsson, T. R.; Leung, K. *Modelling Simul. Mater. Sci. Eng.* **2005**, *13*, R1-R31.

(42) Perdew, J. P.; Burke, K.; Ernzerhof, M. *Phys. Rev. Lett.* **1996**, *77*, 3865.

(43) Solares, S. D.; Michalak, D. J.; Goddard, W. A. III; Lewis, N. S. *J. Phys. Chem. B* **2006**, *110*, 8171.

(44) *Solid State Physics*; Ashcroft, N. W.; Mermin, N. D., W. B. Saunders Company: Florida, **1997**.

(45) *Physics of Semiconductor Devices*, 2nd ed.; Sze, S. M. John Wiley & Sons: New York, NY, **1981**.

(46) *Electronic States in Crystal of Finite Size, Quantum Confinement of Bloch Waves*, Springer Tracts in Modern Physics 212; Ren, S. Y. Springer: Heidelberg Germany, **2006**.

- (47) Haick, H.; Hurley, P. T.; Hochbaum A. I.; Yang, P.; Lewis, N. S. *J. Am. Chem. Soc.* **2005**, *128*, 8990. Bansal, A.; Li, X.; Lauermann, I.; Lewis, N. S. *J. Am. Chem. Soc.* **1996**, *118*, 7225.

## Supporting Information

**Table S1.** Diameter, H/Si ratio, Component, Dimer Si atoms and Dangling-Bonds of Optimized H-SiNW structures

diameter (nm)	Si	H	H/Si ratio <sup>a</sup>	$E_h$ /Si (kcal/mol)	atom <sup>b</sup> dimer Si <sup>c</sup>	dangling bond <sup>d</sup>
1.0	21	20	1.00	<b>2.36</b>	0	0
	21	16	0.80	5.54	4	0
	21	12	0.60	11.02	4	4
1.3	37	28	1.00	<b>2.17</b>	0	0
	37	24	0.86	3.83	4	0
	37	20	0.71	5.70	8	0
	37	16	0.57	5.32	8	4
1.6	52	32	1.00	<b>1.67</b>	0	0
	52	24	0.75	1.89	8	0
	52	20	0.63	2.76	8	4
1.9	76	40	1.00	<b>1.53</b>	0	0

	76	32	0.80	3.19	0	4
	76	28	0.70	1.61	12	0
	76	24	0.60	1.95	12	4
	76	22	0.55	3.81	12	6
2.5	129	52	1.00	1.20	0	0
	129	44	0.85	1.14	8	0
	129	36	0.69	1.26	16	0
	129	32	0.62	<b>0.86</b>	16	4
	129	28	0.54	1.54	16	8
	129	24	0.46	2.30	16	12
3.1	196	64	1.00	1.00	0	0
	196	56	0.88	2.10	0	8
	196	44	0.69	1.01	20	0
	196	42	0.66	<b>0.07</b>	20	2
	196	40	0.63	0.11	22	3
	196	32	0.50	1.11	22	11

<sup>a</sup> We rescale the H/Si ratio for each diameter so that the fully saturated case has H/Si = 1.

<sup>b</sup> Heat of formation energy referred to the Si bulk and hydrogen molecule per Si atom.

<sup>c</sup> Number of reconstructed Si atoms.

<sup>d</sup> Number of dangling-bond defects.

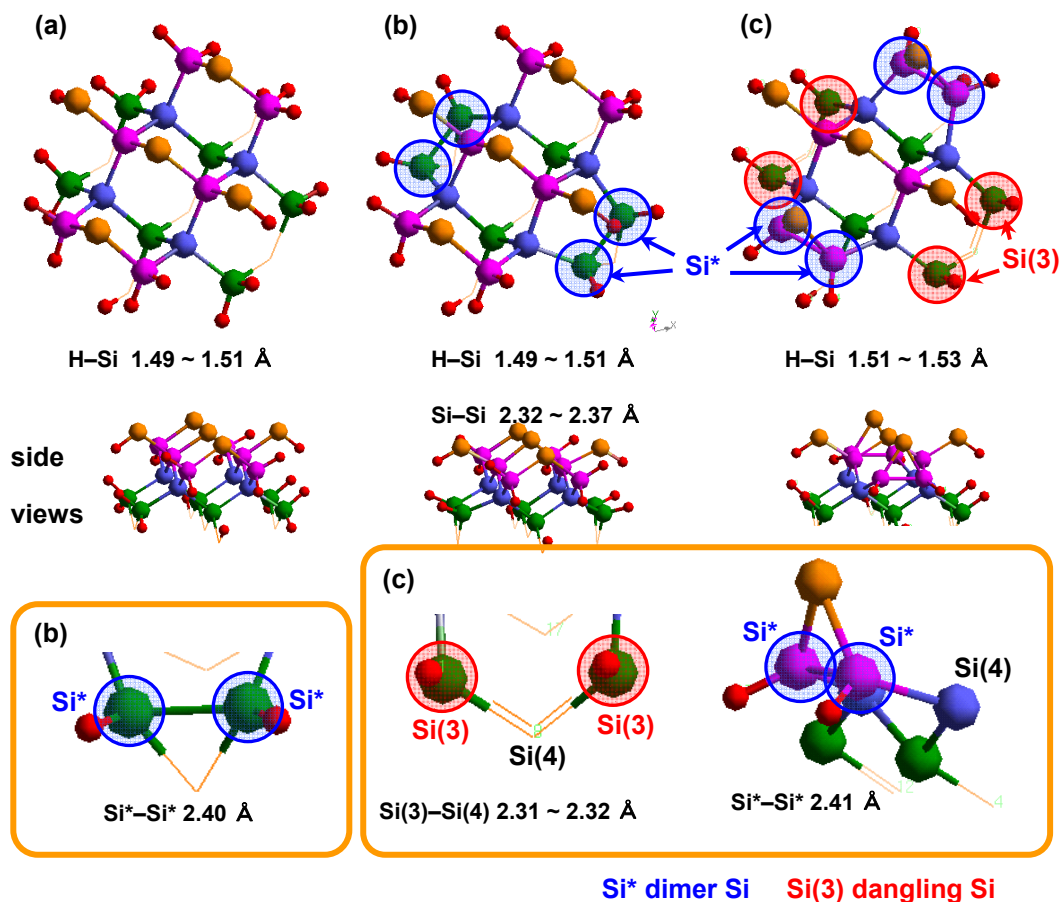


**Figure S1.** Detailed geometries of the optimized H-SiNW structures with  $d = 1.0$  nm.

(a) H/Si = 1.00,  $\text{Si}_{21}\text{H}_{20}$ , fully saturated. No reconstructed Si atoms. All Si atoms are 4-coordinate.

(b) H/Si = 0.80,  $\text{Si}_{21}\text{H}_{16}$ . Four reconstructed Si atoms per unit cell. No dangling bonds.

(c) H/Si = 0.60,  $\text{Si}_{21}\text{H}_{12}$ . Four reconstructed Si atoms and four dangling bonds per unit cell. Geometry is highly distorted (Si-Si distance has large variation).

Heats of formation are (a) 49.5 kcal/mol, (b) 116.4 kcal/mol, and (c) 231.5 kcal/mol as referred to Si crystal and  $\text{H}_2$ .

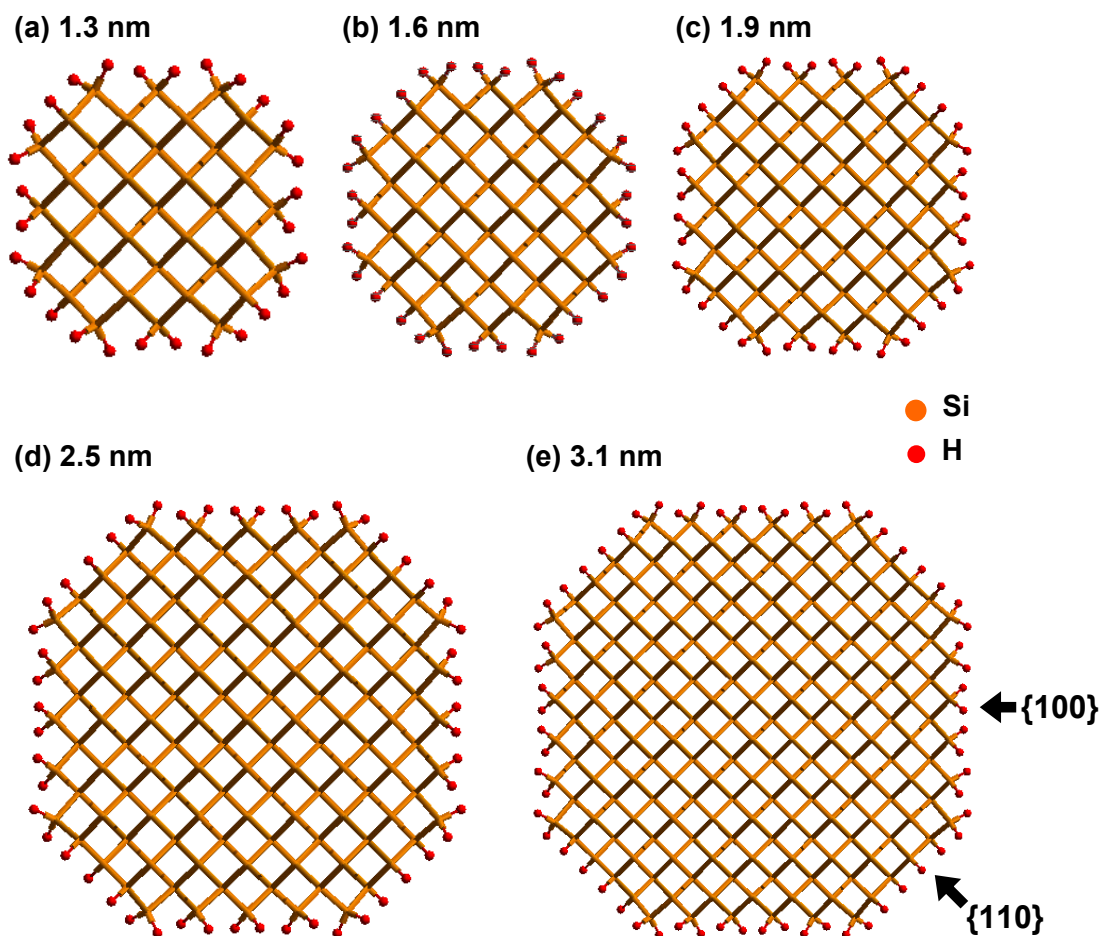


**Figure S2.** Cross section views of the saturated H-SiNWs ( $H/Si = 1$ ) with diameters of (a) 1.3 nm ( $Si_{37}H_{28}$ ), (b) 1.6 nm ( $Si_{52}H_{32}$ ), (c) 1.9 nm ( $Si_{76}H_{40}$ ), (d) 2.5 nm ( $Si_{129}H_{52}$ ), and (e) 3.1 nm ( $Si_{196}H_{64}$ ).

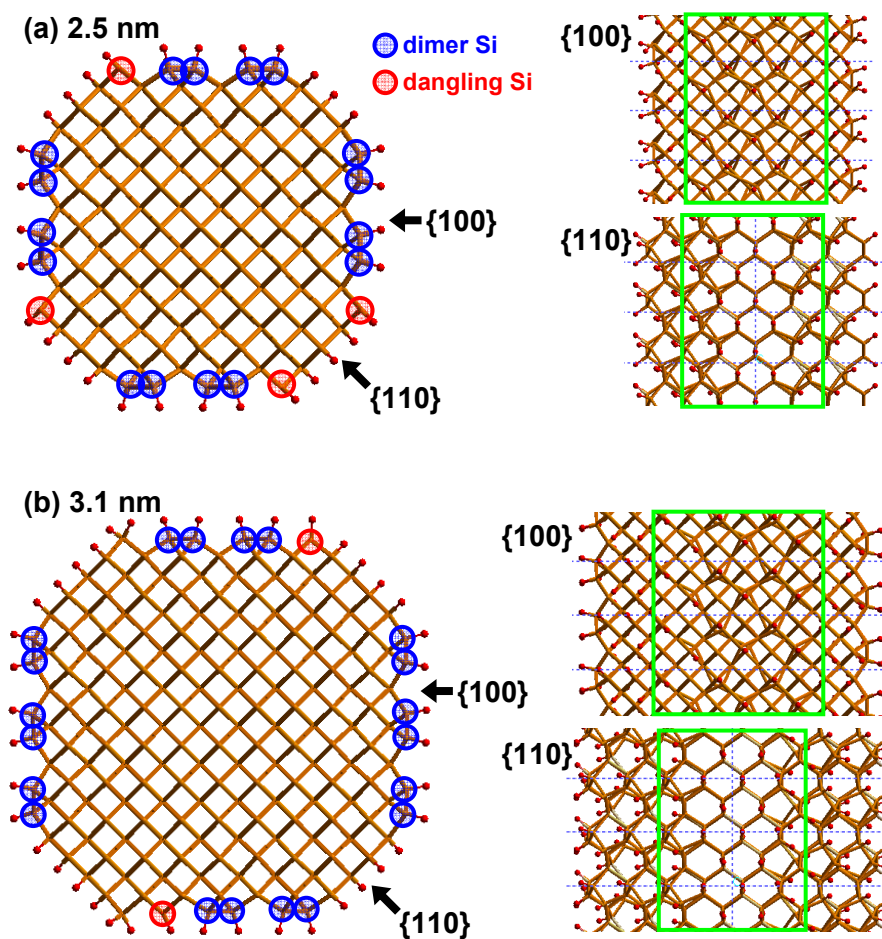


**Figure S3.** Cross section and side views ( $\{100\}$  and  $\{110\}$  surfaces) of the unsaturated H-SiNW models with diameters of (a) 2.5 nm ( $H/Si = 0.62$ ,  $Si_{129}H_{32}$ ), and (b) 3.1 nm ( $H/Si = 0.66$ ,  $Si_{196}H_{42}$ ), which equilibrium structures of the same diameter.

Dimer Si atoms are shown with blue circles and dangling Si atoms are shown with red circles on the  $\{100\}$  surface. The four  $\{110\}$  surfaces show saturated hydrogen coverage.

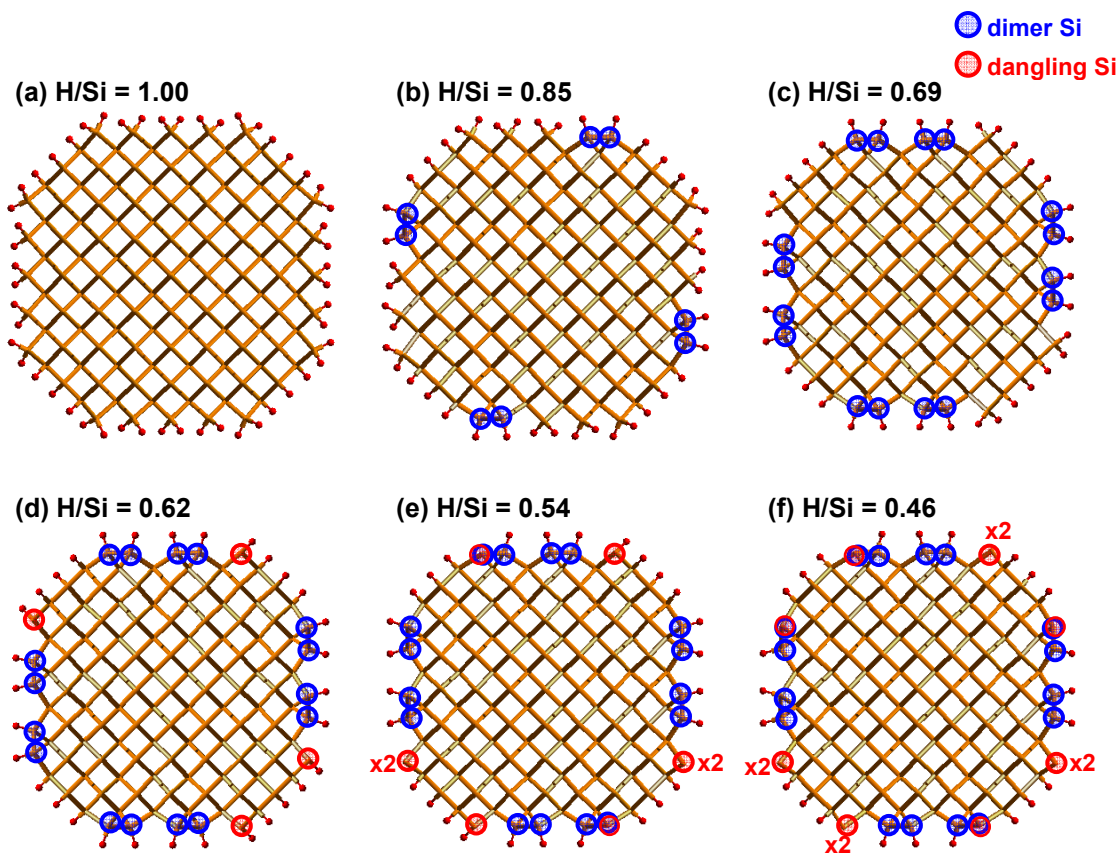


**Figure S4.** Cross section views of the H-SiNW models with  $d = 2.5$  nm. H/Si ratio = (a) 1.00 (saturated),  $\text{Si}_{129}\text{H}_{52}$ , (b) 0.85,  $\text{Si}_{129}\text{H}_{44}$ , (c) 0.69,  $\text{Si}_{129}\text{H}_{43}$ , (d) 0.62,  $\text{Si}_{129}\text{H}_{32}$ , (e) 0.54,  $\text{Si}_{129}\text{H}_{28}$ , and (f) 0.46,  $\text{Si}_{129}\text{H}_{24}$ .

Dimer Si atoms are shown with blue circles and dangling Si atoms are shown with red circles on the {100} surface. 'x2' expresses two dangling bonds per Si atom. The four {110} surfaces show saturated hydrogen coverage.

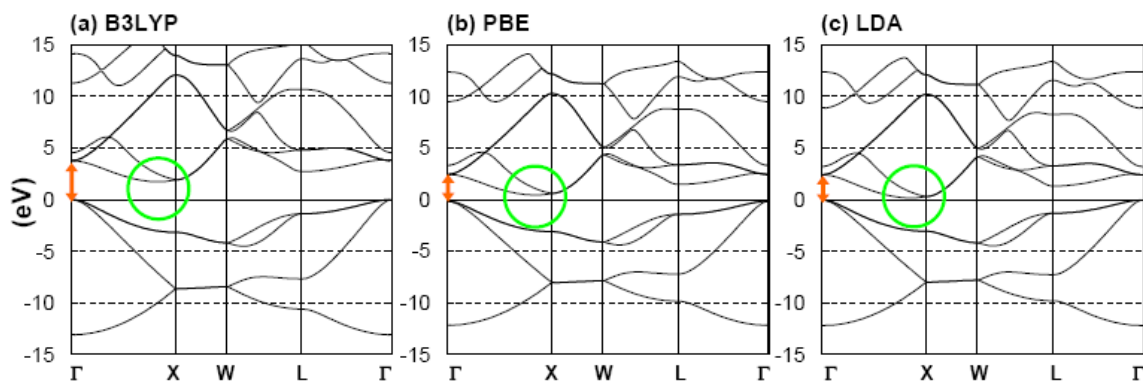


**Figure S5.** Band structures of Si crystal calculated using (a) B3LYP, (b) PBE, and (c) LDA. The VBM is set at 0 eV for comparison. The direct band gaps at  $\Gamma$  are shown with an orange arrow and the CBM is shown with a green circle. The position of the CBM is approximately 82 % for B3LYP and 85 % for PBE and LDA from  $\Gamma$  to X. The calculated band gaps are given in Table 1.

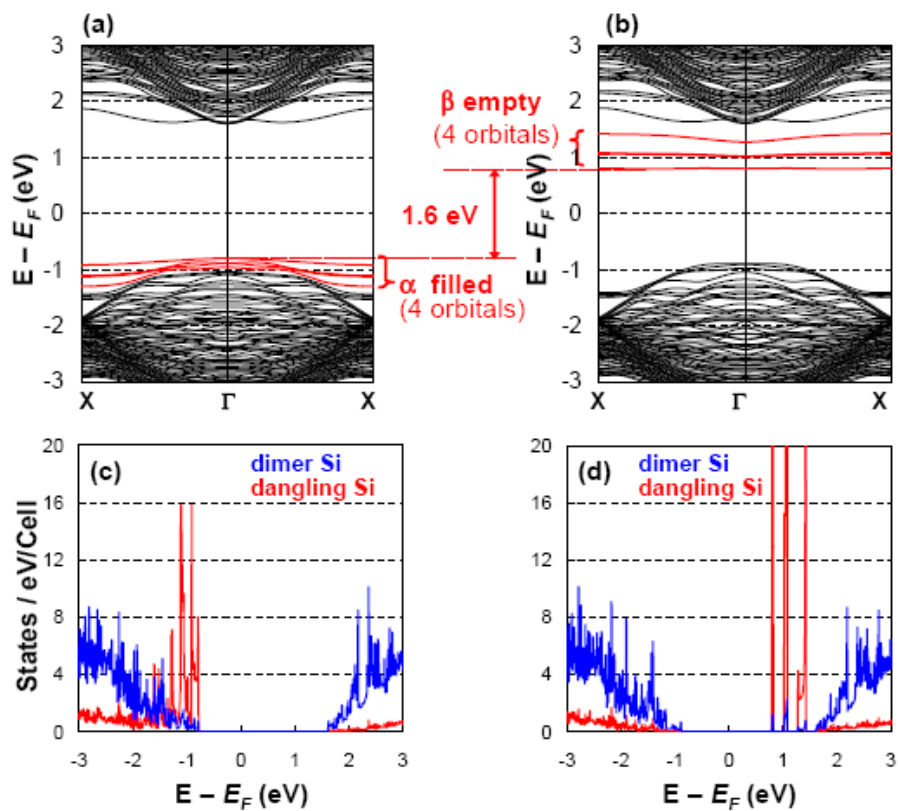


**Figure S6.** Band structures of unsaturated H-SiNW with  $d = 2.5$  nm ( $\text{Si}_{129}\text{H}_{32}$ ) using UB3LYP. (a)  $\alpha$  electrons and (b)  $\beta$  electrons. Partial density of states of Si atoms (per unit cell) of (c)  $\alpha$  and (d)  $\beta$  electrons (blue; dimer Si atoms, red; dangling Si atoms). We find that the four dangling bond Si atoms lead to new LUMO and HOMO states in the band gap.

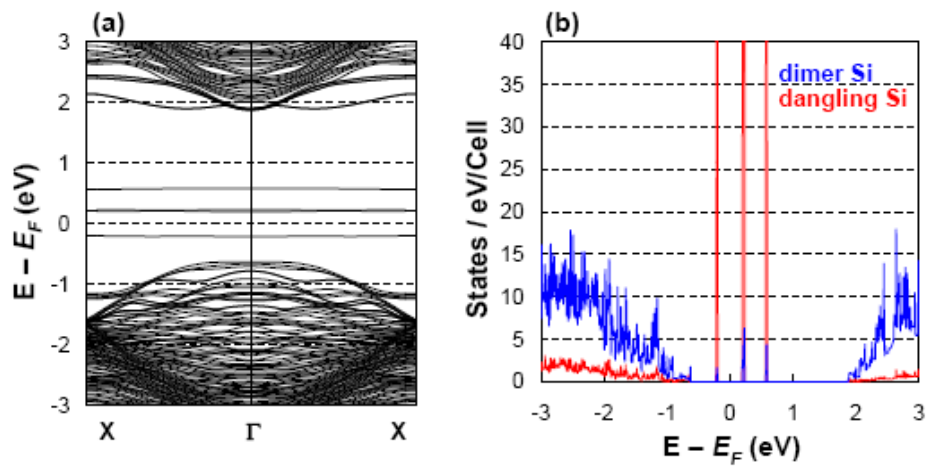


**Figure S7.** (a) Band structures of unsaturated H-SiNW with  $d = 2.5$  nm ( $\text{Si}_{129}\text{H}_{32}$ ) using RB3LYP. (b) Partial density of states of the Si atoms (per unit cell) of (blue; dimer Si atoms, red; dangling Si atoms).

Note that the band gap is 0.39 eV, which is 1.3 eV smaller than the UB3LYP calculation shown in Figure S5. The total energetic from the single point energy calculation by RB3LYP shows 1.5 eV higher than that of UB3LYP (Figure S6).

**Basis Sets in CRYSTAL format<sup>a</sup>**

[http://www.crystal.unito.it/mssc2006\\_cd/tutorials/index.html](http://www.crystal.unito.it/mssc2006_cd/tutorials/index.html)

**Si**

14 5

0 0 6 2.0 1.

16115.9000000000 1.959480215544232E-03

2425.5800000000 1.492880164217892E-02

553.8670000000 7.284780801331127E-02

156.3400000000 0.246130027074480

50.0683000000 0.485914053450895

17.0178000000 0.325002035750458

0 1 6 8.0 1.

292.7180000000 -2.780941414749545E-03 4.438264520798176E-03

69.8731000000 -3.571461816911335E-02 3.266793327542387E-02

22.3363000000 -0.114985058496399 0.134721137226402

8.1503900000 9.356344759857371E-02 0.328678334790414

3.1345800000 0.603017306773259 0.449640458001940

1.2254300000 0.418959213137304 0.261372266232727

0 1 2 4.0 1.

1.0791300000 -0.376107879451492 6.710299112482998E-02

0.3024220000 1.251649598826560 0.956882873440840

0 1 1 0.0 1.

0.0933392000 1.000000000000000 1.000000000000000

0 3 1 0.0 1.

0.4500000000 1.000000000000000

**H**

1 3

0 0 3 1.0 0

33.8650000000000 2.549381454078656E-02

5.094790000000000 0.190373108582211

1.158790000000000 0.852161486043321

0 0 1 0.0 0

0.325840000000000 1.000000000000000

0 2 1 0.0 0

0.750000000000000 1.000000000000000

<sup>a</sup> Ref. 37